



The 1-MW Radiatively Driven Hypersonic Wind Tunnel Experiments Final Report

D. K. Mansfield, P. J. Howard, J. D. Luff, R. B. Miles, G. L. Brown and I. G. Girgis
Department of Mechanical and Aerospace Engineering, Princeton University

R. J. Lipinski, G. E. Pena, and L. X. Schneider
Sandia National Laboratories

J. Grinstead
NASA, Ames

R. Howard
Aerospace Testing Alliance, Arnold Engineering Development Center, Arnold Air Force Base

January 2005

Final Report for Period May 2002 — January 2004

STATEMENT A: Approved for public release;
distribution unlimited.

**ARNOLD ENGINEERING DEVELOPMENT CENTER
ARNOLD AIR FORCE BASE, TENNESSEE
AIR FORCE MATERIEL COMMAND
UNITED STATES AIR FORCE**

NOTICES

When U. S. Government drawings, specifications, or other data are used for any purpose other than a definitely related Government procurement operation, the Government thereby incurs no responsibility nor any obligation whatsoever, and the fact that the Government may have formulated, furnished, or in any way supplied the said drawings, specifications, or other data, is not to be regarded by implication or otherwise, as in any manner licensing the holder or any other person or corporation, or conveying any rights or permission to manufacture, use or sell any patented invention that may in any way be related thereto.

Qualified users may obtain copies of this report from the Defense Technical Information Center.

References to named commercial products in this report are not to be considered in any sense as an endorsement of the product by the United States Air Force or the Government.

DESTRUCTION NOTICE

For unclassified, limited documents, destroy by any method that will prevent disclosure or reconstruction of the document.

APPROVAL STATEMENT

This report has been reviewed and approved.



Capt R. W. Wilson
Applied Technology Division
Test Operations Directorate

Approved for publication:

FOR THE COMMANDER



R.T. Crook
Deputy Chief, Applied Technology Division
Test Operations Directorate

REPORT DOCUMENTATION PAGE					Form Approved OMB No. 0704-0188	
<p>The public reporting burden for this collection of information is estimated to average 1 hour per response, including the time for reviewing instructions, searching existing data sources, gathering and maintaining the data needed, and completing and reviewing the collection of information. Send comments regarding this burden estimate or any other aspect of this collection of information, including suggestions for reducing the burden, to Department of Defense, Washington Headquarters Services, Directorate for Information Operations and Reports (0704-0188), 1215 Jefferson Davis Highway, Suite 1204, Arlington, VA 22202-4302. Respondents should be aware that notwithstanding any other provision of law, no person shall be subject to any penalty for failing to comply with a collection of information if it does not display a currently valid OMB control number.</p> <p>PLEASE DO NOT RETURN YOUR FORM TO THE ABOVE ADDRESS</p>						
1. REPORT DATE (DD-MM-YYYY) January 2005			2. REPORT TYPE TSR		3. DATES COVERED (From – To) May 2002-January 2004	
4. TITLE AND SUBTITLE The Final Report on the 1MW Radiatively-Driven Hypersonic Wind Tunnel Experiments				5a. CONTRACT NUMBER		
				5b. GRANT NUMBER		
				5c. PROGRAM ELEMENT NUMBER		
6. AUTHOR(S) D. K. Mansfield, P. J. Howard, J. D. Luff, R. B. Miles, G. L. Brown, and I. G. Girgis, Princeton University; R. J. Lipinski, G. E. Pena, and L. X. Schneider, Sandia National Laboratories; J. Grimstead, NASA, Ames; and R. Howard, ATA, AEDC				5d. PROJECT NUMBER		
				5e. TASK NUMBER		
				5f. WORK UNIT NUMBER		
7. PERFORMING ORGANIZATION NAME(S) AND ADDRESS(ES) Princeton University, Sandia National Laboratories, and AEDC					8. PERFORMING ORGANIZATION REPORT NO.	
9. SPONSORING/MONITORING AGENCY NAME(S) AND ADDRESS(ES) Arnold Engineering Development Center Directorate of Technology 1099 Avenue C Arnold AFB TN 37389-9013					10. SPONSOR/MONITOR'S ACRONYM(S) AEDC/DOT	
					11. SPONSOR/MONITOR'S REPORT NUMBER(S) AEDC-TR-05-3	
12. DISTRIBUTION/AVAILABILITY STATEMENT Statement A: Approved for public release; distribution unlimited.						
13. SUPPLEMENTARY NOTES Available in the Defense Technical Information Center (DTIC).						
14. ABSTRACT Results and analysis of the RDHWT/MARIAH II 1 MW experiment are reported. The experiment is the addition of approximately 1 MW of energy to a supersonic air flow with an electron beam. The experiment hardware, arrangement and conduct are described. Selected data and analysis are reported. The experiment was subject to transient power fluctuations that were traced to the electron beam source rather than to flow instability. Power stability was established at lower power conditions, and these data were used for selected code validations.						
15. SUBJECT TERMS RDHWT, MARIAH II, hypersonic wind tunnel, supersonic flow, energy addition, e-beam, electron beam, plasma						
16. SECURITY CLASSIFICATION OF:			17. LIMITATION OF ABSTRACT	18. NUMBER OF PAGES	19a. NAME OF RESPONSIBLE PERSON	
a. REPORT	b. ABSTRACT	c. THIS PAGE			Capt Robert A. Wilson	
Unclassified	Unclassified	Unclassified	SAR	135	19b. TELEPHONE NUMBER (Include area code) 931-454-5261	

1. Introduction

This report will describe experiments in support of the Radiatively-Driven Hypersonic Wind Tunnel (RDHWT/ MARIAH II) project that were carried out collaboratively by Princeton University and the Sandia National Laboratory. The purpose of the experiments was to demonstrate the viability of increasing the total enthalpy of a wind tunnel by adding energy downstream of the nozzle in the supersonic flow regime, thus avoiding the need for excessively high temperatures in the plenum for high Mach number operation. Previous experiments have shown that this concept is viable at power levels up to 100kW. In the experiments reported here, the energy addition is at higher levels of radiative power (1MW) than had been attempted heretofore. The objective is to validate existing energy-addition models and to develop a further understanding of physics issues involved with the addition of electron beam energy to supersonic flows [1-4]. The experiments to be described were performed in Albuquerque, New Mexico at the Sandia HAWK Electron Accelerator Facility. Experimental work began in May 2002 and was divided into two series of data collection: series A and B. In September, data collection series A was suspended for nine weeks while modifications to the HAWK were undertaken. The subsequent collection of data, series B, ended in early April 2003. Analysis of the data continued until November 2003.

The work outlined below describes the third in a sequence of energy addition experiments that employed the HAWK e-beam. The first experiments involved the addition of 10 kW for durations of 500 – 700 μ s and were aimed at demonstrating that stable heated airflow could be produced and characterized with a reliable set of diagnostic measurements [1]. The second set of experiments involved the injection of 100 kW using a 700 keV e-beam for times as long as 1 ms. Using external magnetic fields, attempts were made to bend and focus the e-beam so as to minimize energy loss to the nozzle wall. Improvements to both the diagnostics employed and to the quantitative comparison of data to CDF models were also accomplished in the second set of experiments. The latest set of experiments was aimed at injecting 1 MW of power from a 1 MeV e-beam delivering 1 Amp of current for times as long as a few milliseconds. Additional objectives of the 1 MW experiment plan were

- To demonstrate bending of the e-beam sufficient to avoid impingement of the high-temperature airflow on e-beam delivery components (45°)
- To demonstrate the extraction of the e-beam through a gasdynamic window (This was to incorporate a plasma porthole concept proposed by Brookhaven Laboratory)
- To demonstrate efficient electron extraction from an annular cathode immersed in a magnetic field and ensuing focusing into the nozzle to form a quasi top hat profile energy deposition region with suppressed electron reflection back out of the nozzle
- To attain an enthalpy ratio comparable to that envisioned for a Mach 12 Missile Scale Hypersonic Wind Tunnel (MSHWT) (2.79)
- To validate energy deposition and e-beam steering models

- To establish the effect of the e-beam on the chemistry of the heated air
- To gain an understanding of the e-beam current return path
- To observe whether or not arc discharges occur in the nozzle.

To attain the goals and parameters outlined above, several improvements to the beam delivery technology employed during the previous experiments were needed. After the conclusion of the 100 kW experiments, the HAWK accelerator was modified to allow for the injection of more power (1 MW) at a higher energy (1 MeV) and for a longer duration (7 ms). Magnetic coils were also added to the accelerator to capture electrons as they were emitted from the cathode and to sculpture the spatial profile of the electron beam power density into a quasi-rectangular (i.e. top hat) profile.

During the experiments to be described, the e-beam from the upgraded HAWK accelerator was introduced into an expanding supersonic airflow from a high-pressure (2100 - 2750 psi), high temperature (600 - 615 K) plenum. The high-energy e-beam was directed and focused into a carefully designed expansion nozzle from downstream using externally applied magnetic fields. The configuration of external magnets was designed to ensure that the resulting field lines were approximately parallel to the nozzle wall. This was done to minimize the interaction of the e-beam with the inner surface of the nozzle thus avoiding damage to the nozzle wall. Diagnostic measurements were made to determine the flow field in both the e-beam-heated and the unheated cases over a wide range of plenum and e-beam conditions.

Because the purpose of the experiments was to gain an understanding of the energy addition process, particular care was taken to measure the electron beam power and to account for the current delivered to the nozzle assembly from the HAWK accelerator.

Questions of e-beam and airflow stability were also addressed. In particular, because the duration of e-beam heating (up to 7 ms) was longer than the transit time of the air in the nozzle (~ 0.5 ms), beam-driven airflow instabilities had sufficient time to develop. The absence of these instabilities was confirmed using a diagnostic suite that is described below.

The results of diagnostic measurements were compared against time-dependent computer simulations of the airflow as is also described below.

An Overview of the 1 MW Experiments

Most of the objectives of the 1 MW experiments were either partially or completely met. Data taken from approximately 85 blowdowns with e-beam heating was archived and has been analyzed. All useful data were taken during the series B time frame. Series A established that several revisions to the experiment were needed prior to the acquisition of reliable data. Examples of the most important revisions include the following:

- Because of complications arising from excessive heating and sustaining a discharge in the strong magnetic field, the plasma porthole was abandoned in favor of a thin exploding window and a fast acting shutoff valve to permit the beam to exit the HAWK accelerator
- In order to achieve precise and optimal coupling of the e-beam into the nozzle, the nozzle was moved away from HAWK by about 10 cm and an additional beam steering magnet was installed between HAWK and the nozzle.
- The dielectric union that was used to isolate electrically the nozzle / magnet assembly from ground was found to be faulty and was removed and refurbished. This modification allowed for the measurement of the electron beam current delivered to the nozzle.
- After the electron beam current into the nozzle was found to be both lower and much more erratic than the HAWK current measured internally, the experimental effort was briefly re-directed toward gaining an understanding the source of large variations observed in the nozzle current. The source of these fluctuations was eventually determined to be caused by internal mechanisms in the HAWK accelerator and not, for instance, by an air-beam instability (see Appendix A5).
- New Optrand pressure transducers that were designed to be less sensitive to sudden increases in temperature were purchased and installed in the walls of the nozzle (see Appendix A5).
- The internal components of the HAWK accelerator were refurbished and cleaned to suppress internal breakdowns that repeatedly occurred during test series A. In addition, the maximum operating voltage was reduced from 1 MV to 700 kV in order to avoid further breakdowns and improve the reliability of e-beam injection.
- With the lower Hawk operating voltage and with the plenum conditions employed to accommodate the lower HAWK voltage and heater limitations (~2100 psi and ~605 K instead of the design target of 2650 psi and 650K), it was observed that the airflow became subsonic at deposited powers greater than about 450 kW. Subsequently, the majority of the energy-addition experiments were performed slightly below this level to avoid complications in the interpretation of the data that would arise from attempting to model the supersonic to subsonic transition.

A summary of the data is shown in Fig 1.1. In this figure, the average of the electron beam power attained over 1.5 ms is plotted against the air pressure measured in the plenum at the time of injection. The data are displayed for several values of the HAWK beam voltage. This plot shows the wide range of beam power, beam current, beam voltage and plenum conditions that were explored during this work. The highest power deposited was 890 kW.

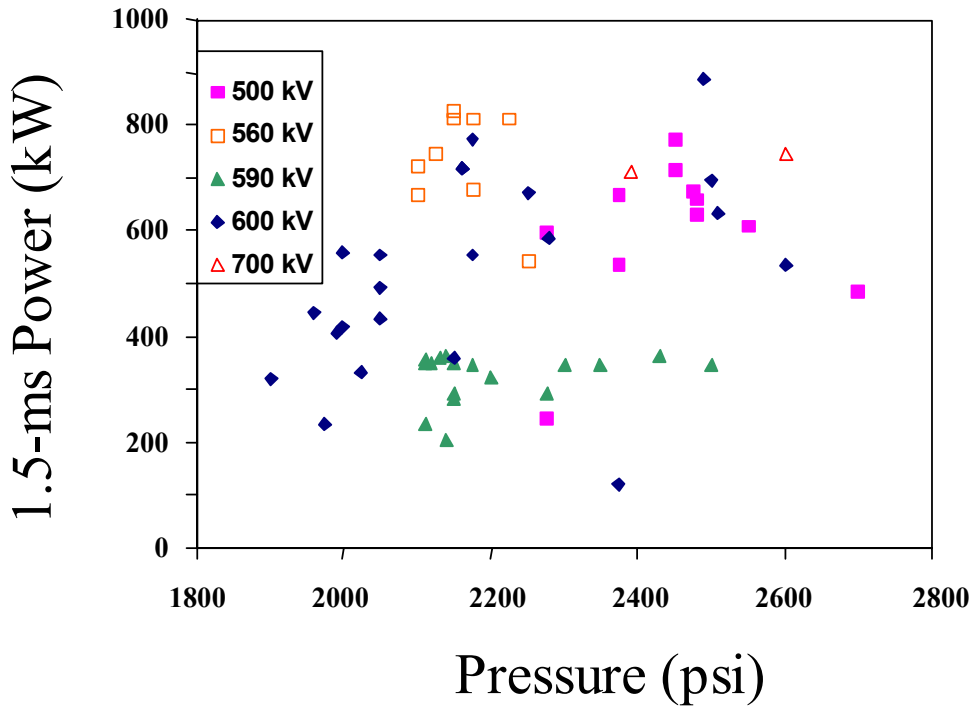


Figure 1.1: The average power attained over 1.5 ms is plotted against the air pressure measured in the plenum at the time of injection. Also shown are the e-beam voltages measured at the time of injection.

The remaining sections of this report are divided as follows: Section 2 presents brief descriptions of the hardware used during the experiment. More complete descriptions of the hardware are given in the associated appendices (A1, A2 and A3) including a description of the nozzle design process. Section 3 presents an overview of the electron beam injection system and the improvements that were made to the HAWK accelerator. More details are again given in an appendix (A4). Descriptions of the diagnostics employed during the experiments are given briefly in Section 4 and more comprehensively in an appendix (A5). The numerical methods employed to simulate the airflow are described briefly in Section 5 and more completely in the associated appendix (A6). A discussion of the development of moderate and high power shots is given in Section 6. In Section 7 the data are compared to numerical simulations. Results and conclusions appear in Section 8. A discussion about future work and possible improvements to the experiments is given in Section 9.

2. Descriptions of the Hardware

High-Pressure Air Delivery System

Regulated high-pressure heated air was routinely delivered to the nozzle / magnetic assembly by computer command. The air-delivery system worked well at the system design pressure (2650 PSI). The pebble bed heater used during the experiments delivered air that was slightly cooler (615 K) than the 650 K design temperature (see Fig 2.1 below). Both the air delivery system and the pebble bed heater underwent some modifications during the course of the experiments. A more complete description of these systems and their performance is given in Appendix A1.

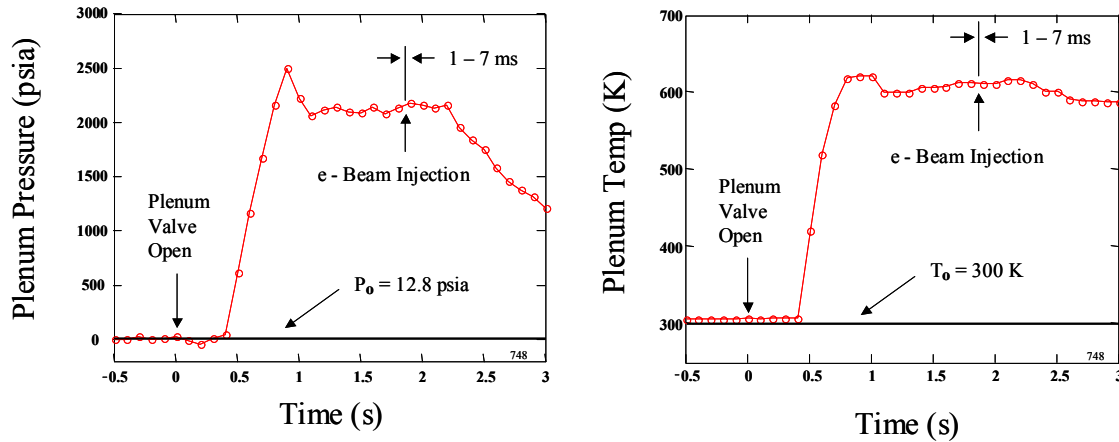


Figure 2.1: The plenum pressure and temperature for a typical blowdown. Also indicated are the timing and duration of e-beam injection.

Nozzle Design and Fabrication

Two important criteria went into the design of the nozzle and heating profile employed for the 1 MW experiments: the throat diameter (1.1 cm) and the enthalpy ratio (total enthalpy to plenum enthalpy = 2.76) were to be comparable to the 200 MW, 1 meter diameter test core flow, Mach 12 MSHWT design. The design for the internal profile of the nozzle was arrived at after completion of an iterative process involving numerical models of increasing complexity. The first level of modeling was used to determine the thermodynamic ideal path; hence a purely thermodynamics analysis was used and no flow solving was required. The next level of modeling involved solving the differential equations of inviscid one-dimensional geodynamics coupled with empirical equations describing e-beam heating. At this stage, the nozzle contour was optimized to achieve the thermodynamic ideal path. The last level of modeling involved solving the axisymmetric two-dimensional inviscid equations fully coupled with a two-dimensional e-beam code.

The nozzle design work was a collaborative process between the Princeton and Sandia teams in the months leading up to the beginning of the laboratory work. Details of the work are given in Appendix A2. Also included in the appendix are predictions of the axisymmetric fluid mechanics pertaining to the 1 MW energy addition experiments.

After arriving at a design, a split, contoured nozzle was machined from two pieces of stainless stock on a Bridgeport CNC milling machine. The two halves were carefully aligned, held together with stainless socket head cap screws and sealed with gold wire where required.

A picture of the unassembled nozzle may be seen in Appendix A1.

The Computer Control System

Virtually all aspects of the 1 MW experiments were controlled in real time with a stand-alone PC computer system operating at the relatively modest speed of 200 MHz. Labmaster, a program designed specifically for the Sandia / HAWK environment, employed LabView software in conjunction with a bank of digital delay /pulse generators (DD/PGS) to accomplish the tasks listed below both simultaneously and autonomously:

- Synchronization of all experimental hardware (lasers, cameras ...etc).
- Collection, processing and storing of slow (10 Hz) data
- Triggering, collection and storing of fast (75 kHz) data
- Control of high-pressure air delivery system to initiate and terminate air flow.
- Triggering the firing sequence of all magnet fields
- Setting threshold and inhibit levels to protect the nozzle.
- Triggering (or inhibiting) the firing of the HAWK accelerator.
- Safety checks with conditional go/no-go decision tree.

Because the computer control system worked effectively in the roles outlined above, blowdowns could typically be accomplished in about two seconds - approximately a factor of five faster than had been anticipated. This reduction in blowdown duration allowed for the efficient use of both air and heat. These efficiencies, in turn, allowed for as many as twelve blowdowns to be accomplished in a run day. In fact, during the critical data-taking months of February and March, eighty-five blowdowns with e-beam injection were accomplished.

Details of the computer control system are given in Appendix A3.

3. Electron Beam and Accelerator

The previous energy addition experiment had achieved 100 kW of energy addition for a maximum of 3 ms. In that experiment, because of reflections back out of the nozzle, only about 25% of the beam power was deposited into the blow-down air; because of the potential for thin film window failure, most of the run durations were limited to 1 ms (which was less than the response time of the pressure sensors); because the beam was tightly spiked on centerline, good data were hard to obtain; and because of magnet limitations, the beam was bent only 11 degrees going into the nozzle (which is much too small an angle for the final facility). So the goals for the electron beam and accelerator for the 1-MW experiment were

- To demonstrate a substantial increase in predictable power deposition by delivering 1 MW into flowing supersonic air with an electron beam
- To minimize beam reflections through high-efficiency extraction of electrons from the cathode into a magnetic field that is continuous into the nozzle
- To demonstrate stability of energy deposition at these higher power levels for 5 ms (approximately 10 flow transit times)
- To demonstrate extraction of the beam from the Hawk accelerator through a differentially-pumped gas dynamic window so the beam current density is not limited by a thin film window
- To demonstrate a uniform electron heated core flow
- To demonstrate beam bending between the Hawk exit and the nozzle entrance sufficient to provide an uninhibited air expansion and meet MSHWT requirements.

The reason that the previous 100 kW experiment had both low efficiency and low power was that 75% of the beam was reflected by the converging magnetic field lines in the nozzle because the beam was born in a field-free zone. It was anticipated that placing the cathode in a strong magnetic field and maintaining a continuous field all along the beam transport route would solve that problem because there would be less of an overall field gradient to overcome in penetrating the nozzle. Accordingly, a set of magnet coils was built around the HAWK accelerator and additional solenoids were placed along the beam path. This required numerous modifications to the HAWK internal structures so as to accommodate the applied fields.

During the previous energy-addition experiments, the duration of e-beam injection was limited because the beam was extracted into air through a beryllium foil. For example, during the 100 kW experiments, the period of e-beam injection was typically 1 ms and never more than 3 ms because at longer durations (or higher powers) the foil would melt. To overcome these limitations, a differential pumping system was developed that allowed the beam to be extracted through a series of small apertures that were open to air and that had a series of pumps placed between the apertures. The continuous magnetic field allowed the beam radius to be compressed

at these apertures which, in turn, allowed for a reduction in the aperture size and hence a reduction in the pumping requirements. When initially tested, the pumping system did not work as well as desired, so a compromise was reached in which the final aperture (adjacent to room air) was covered with a thin acetate foil. When HAWK was fired, the emitted e-beam “burned” through the acetate in about 0.05 ms. Upon completion of injection, a fast-closing valve near the accelerator was actuated. The additions of the acetate window and fast-closing valve reduced the influx of air into the accelerator enough to allow the existing differential pumping system to function well.

The original concept for the differential pumping system included a “plasma porthole” based on a concept demonstrated at Brookhaven National Laboratory [5]. While the Sandia team did implement the porthole successfully without an applied magnetic field, in the presence of the HAWK ambient magnetic field, the porthole could only be made to operate when the ignition electrode was placed on the centerline – thus precluding e-beam injection. This unfortunate fact, as well as concerns about stability and thermal load, led to the “exploding window” alternative described above. A discussion of the plasma porthole is given in Appendix A4.

By starting the beam within a magnetic field, the beam would not be focused as tightly along the centerline as in the previous 100 kW experiment. This modification allowed a broader central zone within which to make measurements. Nonetheless, scattering of the beam in the air within the nozzle caused the otherwise uniform beam to broaden into a Gaussian shape (including a peaked center). To help restore the flatness of the beam radial intensity profile, an annular cathode was used. With the use of the annular cathode, as the beam scattered, some of the electrons scattered inward to fill the hole in the annulus. With a carefully chosen annular thickness, a fairly flat beam profile was achieved within the nozzle.

To minimize the size of the final aperture in the differential pumping system, a 5-Tesla superconducting magnet was introduced at the exit of the accelerator. Because the magnet had a large bore (15 cm free access), it exerted a strong influence over a relatively large area. This enabled the e-beam that exited HAWK to be bent around 45° with minimal need for additional magnets within the bend. This large bending angle prevented the nozzle airflow from impinging onto any beam-delivery hardware. The bending action caused by the two magnet systems – the superconducting exit magnet and the nozzle magnets - can be understood by noting that when two solenoid magnets placed end-to-end are separated slightly and bent, the field lines “bow” like a bundle of straw held in two hands. An emitted e-beam following the bent field lines would hence be constrained to exit the HAWK and follow the field lines into the nozzle. Some fine-adjustments to the positions of the magnets were needed to cause the beam to follow the centerline of the nozzle. Such adjustments as were needed were carried out *in situ* by trial and error.

In addition to the changes discussed above, several modifications to the HAWK accelerator, data acquisition, and exit air handling systems were made subsequent to the 100 kW experiments. In all cases the modifications were carried out in anticipation of the 1 MW experiment. The important modifications included the following:

- The addition of nine pulsed magnets and one superconducting magnet to control the beam
- Modification of internal Hawk electronics to tolerate the magnetic field

- Modification of internal Hawk hardware to immobilize them in the magnetic field
- Development of a differential pumping system, fast valve, and timing system
- Addition of a 5-Tesla superconducting magnet to minimize the open aperture into the Hawk and guide the beam around 45^0 into the nozzle entrance
- Increase in the size of the main capacitor bank to increase Hawk beam power and duration
- Addition of a “jet deflector” to capture the exiting nozzle air, cool it and deflect it upward
- Upgrade of the control electronics to enable easier operation and safety checks

Figure 3.1 shows the overall configuration of the accelerator system after the modifications.

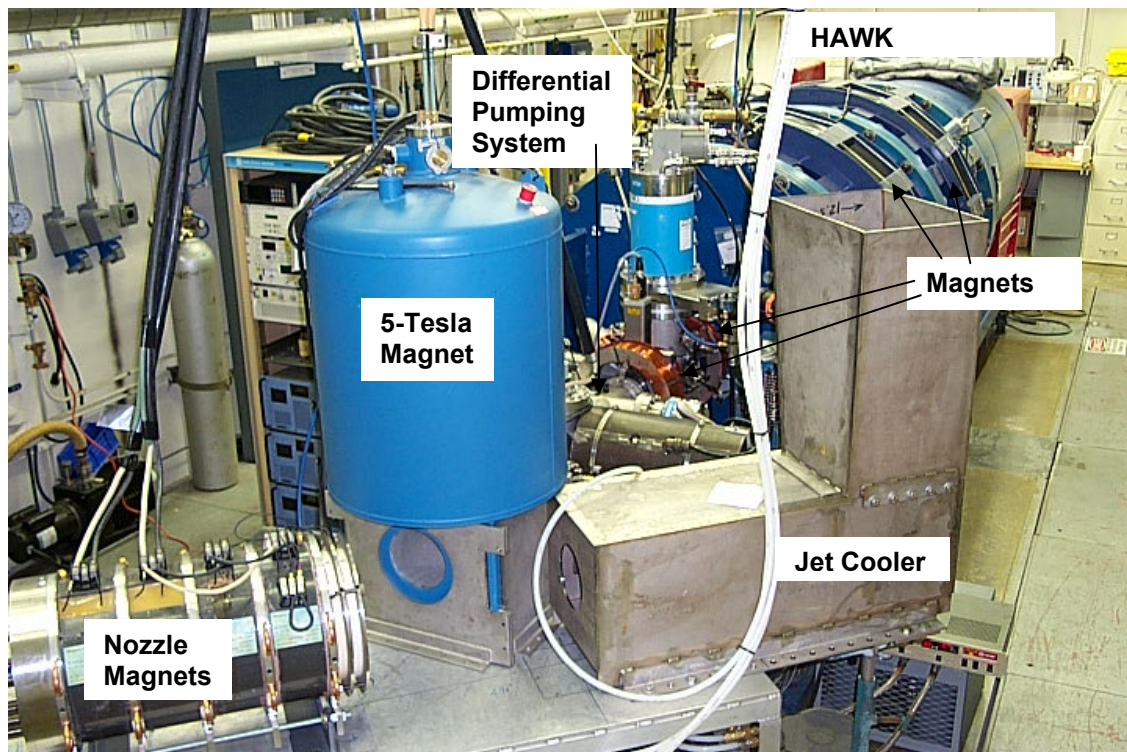


Figure 3.1: An overview of the HAWK accelerator system: Seen in the foreground of this picture is the nozzle/magnet assembly as well as the jet cooler used to deflect upwards the air from a blowdown. The 5-Tesla magnet and dewar are shown just in front of the differential pumping station. The accelerator with external magnetic coils can be seen in the background.

The net result of the modifications was the injection of a 1-MW, 5-ms, 600-kV beam into the nozzle. Figure 3.2 shows a picture of a 600-kV, 1.3-A, 0.5-ms (780 kW) beam bending and striking a graphite target positioned near the exit of the nozzle. Figure 3.3 shows the current trace measured using a graphite probe during four shots, after the additional work on the accelerator. Unfortunately the beam current was even more erratic at higher voltages, probably due to the beam being slightly larger and increased scraping on internal apertures. It is believed that the erratic beam current is due to acoustically driven vibrations of beam apertures inside the Hawk. During the experiments the local acoustic noise level is in excess of 140 db.

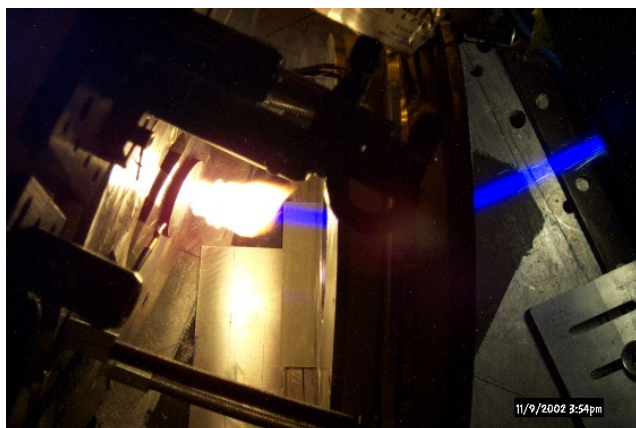


Figure 3.2: 600 kV, 1.3 A, 0.5 ms, 390 J

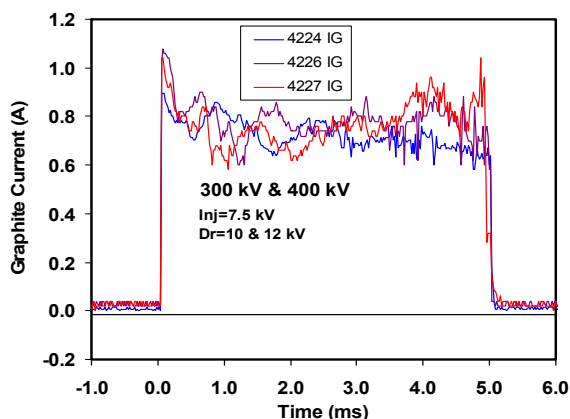


Figure 3.3: Current into graphite at nozzle exit

The beam was aligned into the nozzle by running at very low current and monitoring its location with thin film scintillator disks that were inserted at various stations inside the nozzle and observed with a camera. Figure 3.4 shows the beam hitting these scintillators inside the nozzle at various distances from the throat. This method of alignment is satisfactory if one can assume that the electron beam location does not change when the current is increased and that electron beam scattering in the high pressure air is symmetric. Even so, the beam diameter is predicted to increase due to strong scattering from the air. The beam heating is greatest along the centerline leading to a decrease in the air density in that region, so the scattering is not radially uniform. That will lead to a change in the beam profile as the beam penetrates far into the nozzle. The presence of large beam current fluctuations suggests that the beam may be clipped inside the accelerator, and thus it may be significantly changed by the time it arrives in the nozzle.

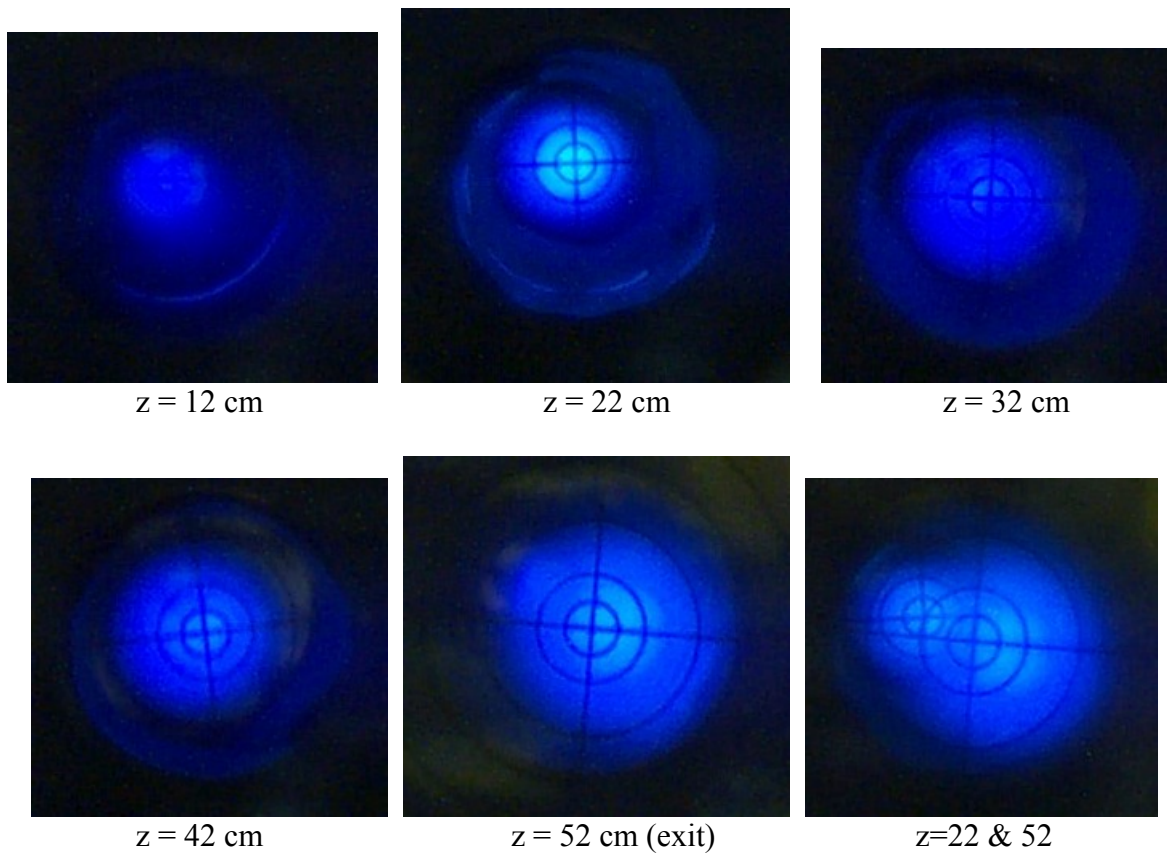


Figure 3.4: Beam shot photos taken at various nozzle locations

4. Diagnostics Employed

Measurements involving several diagnostic systems were taken in an effort to characterize the flow field both internal and external to the nozzle as well as with and without e-beam heating. A brief summary of the diagnostics employed is presented in Table 4.1 below. The locations of the pressure and temperature sensors along the nozzle are given in Table 4.2. A more complete description of the diagnostic suite is given in Appendix A5.

Table 4.1: The diagnostics employed during the 1 MW experiments

Diagnostic System	Parameter Measured	Comment / Equipment
Omega Pressure Transducer	Plenum Pressure	See Table 4.2 below
Thermocouples	Plenum & Nozzle Temperatures	See Table 4.2 below
Optrand Transducers	Nozzle Pressures	Slow Thermal Drift Good Fast Data
Shadowgraph	Mach Angle	Verdi Laser PSI Camera
Direct Spark Velocimetry	Air Speed (w / wo e-beam)	YAG Laser PSI Camera
Shadow/Spark Velocimetry	Air Speed & Sound Speed (wo e-beam)	Verdi Laser PSI Camera
Rayleigh Scattering	Air Density	Multi-pulse YAG laser PSI Camera
Nozzle Return Current	Current through Nozzle to Ground	Nozzle floated by 5.5 Ω Resistor
Accelerator Exit Return Current	Current Returning to HAWK Exit	Floating (10 Ω) Copper Disk at HAWK Exit
X-Ray Luminosity	X-Rays from Beam / Air Interaction	Blackened Photomultiplier
NO Spectroscopy	UV Absorption at 226 nm due to NO Formation	Xenon Lamp NO Spectrometer

Table 4.2: Location of the Optrand sensors along the nozzle and thermocouples measured from the throat.

Channel #	1	2	3	4	5 (exit)
Distance (cm)	6.281	18.96	31.53	44.25	51.16

5. Numerical Simulation of the Airflow

During the experiments, the e-beam voltage was observed to be a slowly varying in time but the nozzle current was seen to fluctuate in an unpredictable manner. The resulting unsteady power deposition represented a considerable challenge to the numerical modeling of the experimental data. A time-dependent approach was eventually developed that could take into account the measured unsteady power deposition and allow for comparisons between measured and calculated parameters such as nozzle pressure, exit velocity and density.

This numerical model involved solving the axisymmetric Euler equations. The equations were first discretized using a second order, cell-centered finite-volume spatial scheme. All thermodynamic quantities employed in the code were obtained from NIST 14, the real gas equation of state tabulated by NIST. After undertaking a study of the errors generated by using a finite number of electrons, it was determined that 16,000 electrons represented a reasonable trade-off between the accuracy obtained by the code balanced against the CPU time needed to make predictions describing unsteady energy addition. The anticipated error generated by the choice of 16,000 electrons was found to be only 1%. A more complete description of the modeling work is given in Appendix A6.

6. Development of Shots with Moderate and High Powers

Moderate-Power Shots

As was mentioned above, the erratic nature of the measured nozzle current-to-ground had not been anticipated. At high e-beam powers (> 450 kW), large fluctuations in the nozzle current generally began about 1 - 1.5 ms into the injection and varied greatly from shot to shot. This behavior can be seen in Fig 6.1 below. It was also observed with the shadowgraph that at power levels above approximately 450 kW the exit flow became subsonic.

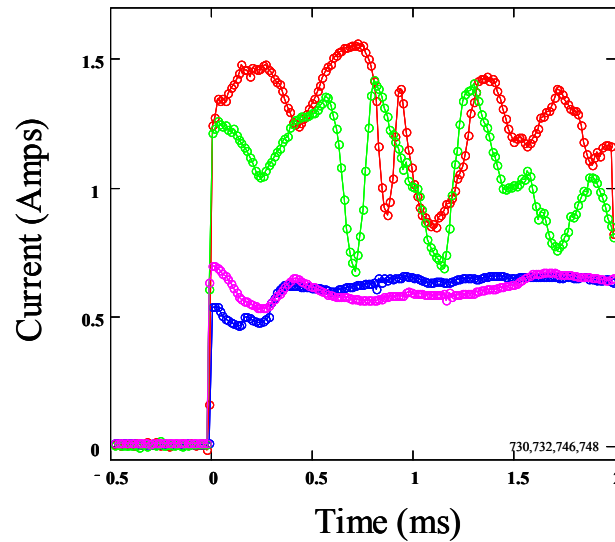


Figure 6.1: In this figure are shown two examples each of the measured current from high-power (> 450 kW) and moderate-power (380 kW) shots. Clearly improved behavior, at least for the first 2 ms of e-beam injection, can be seen in the current measured during the moderate-power shots.

These findings necessitated changes to the plan for the 1 MW experiment. During the closing weeks of the experimental campaign it was decided that a standardized moderate-power (SMP) shot (300-400 kW) that would remain supersonic during the entire duration of e-beam heating had to be developed. This standard shot was developed for two reasons (1) the analysis of such a shot would be simplified as compared to a high power shot that was driven subsonic and (2) the stability of the nozzle current for moderate-power shots was observed to be *moderately* better than that of high-power shots. It was anticipated that this latter feature would also simplify subsequent data analysis and comparison to theory. A considerable fraction of the subsequent experimental effort was then devoted to the generation and diagnosis of these so-called SMP shots.

The typical plenum pressure for the SMP shots was 2150 ± 25 PSI while the typical plenum temperature was 605 ± 3 K. The operating pressure was chosen by trial and error in the laboratory to allow for reasonably deep penetration of the moderate-power e-beam into the nozzle. As discussed below, under these plenum conditions, e-beam injection with 380 kW was observed to penetrate slightly more than 50 percent of the length of the nozzle. Further, these SMP shots remained supersonic for the entire duration of e-beam injection as will also be discussed below.

Diagnostic measurements with the shadow / spark velocimetry system outlined in Appendix A5 were used to determine the unheated characteristics of the SMP blowdowns. Shown in Fig 6.2 below are representative shadowgraphs of a spark introduced a few millimeters in front of the nozzle exit into the airflow of a typical SMP blowdown with no e-beam injection (shot 734). The shadow of the spark can clearly be seen to travel downstream as time progresses. Also visible is the shadow of the weak circular shock wavefront propagating radially outward from the impressed spark. The airflow in this case is clearly supersonic because the weak shock wave propagating upstream (to the left) is slower than the flow. Measurements of the positions of both the spark shadow and the weak shock wave are shown in Fig 6.3. The slopes of the straight

lines fitted through the data represent measurements of the flow speed and the speed of sound in the airflow. In the next section of this report, these measured values are compared to the predictions of the Euler code as well as to velocity measurements made by another technique. Shadow / spark velocimetry measurements were not used to characterize e-beam heated airflow because no shadowgraphs were obtainable when the e-beam was injected. This was likely due to the lowering of the central density during e-beam injection and the related reduction in the index of refraction.

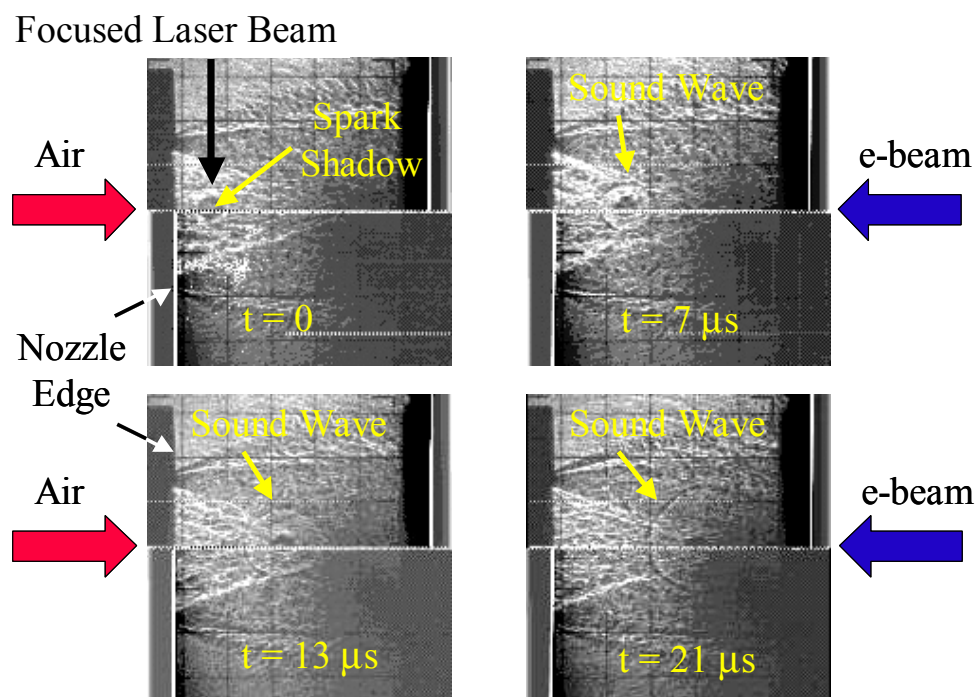


Figure 6.2: Shadowgraph/spark images for a typical SMP blowdown with no heating.

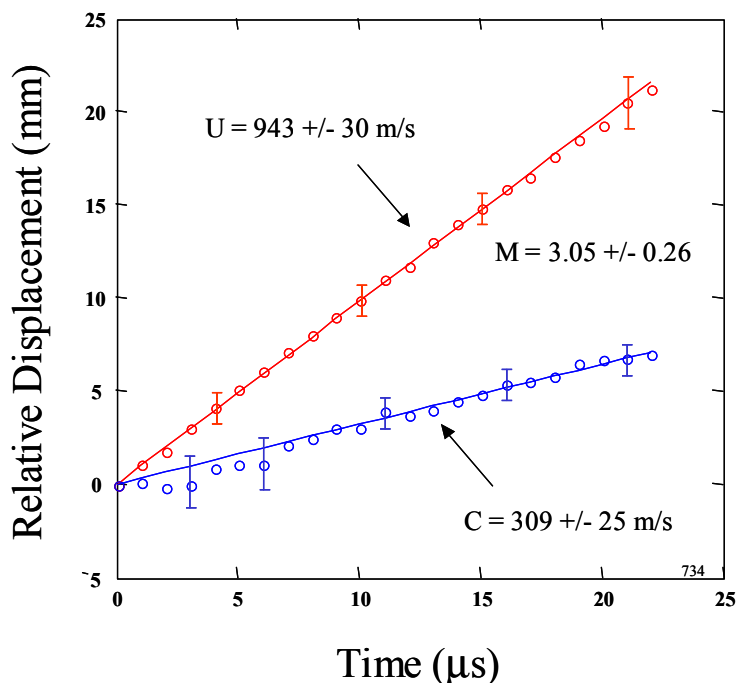


Figure 6.3: The relative displacements of the spark shadow and the acoustic wavefront for the typical unheated SMP shot discussed above. The two slopes, fitted by the method of least squares, represent the flow velocity and the speed of sound. The ratio of the slopes represents the Mach number of the flow.

High-Power Shots

Aside from the intrinsic instability shown in Fig 6.1, the generation and subsequent analysis of high-power shots presented several more challenges than SMP shots. For example, it was observed that, for shots with injected power greater than about 400 - 450 kW, the airflow was driven subsonic. This was considered to be an unwanted complication in the effort to model the behavior of beam-heated airflow.

The depth of e-beam penetration for high-power shots was also a concern. For example, in order to generate measurable amounts of NO, it was determined that high power shots with deep penetration of the e-beam into the nozzle were needed (see discussion in Appendix A5). To achieve this deep penetration experimentally, the plenum pressure was adjusted by trial and error between high-power shots while monitoring the pressure transducer located closest to the nozzle throat (Optrand channel 1). This adjustment procedure was, of course, intrinsically risky because it put the nozzle surface at risk of damage. An example of the measured nozzle pressures for one of these high power shots is given in the next section of this report (see Fig 7.12 below).

7. Comparison of Data and Predictions

Airflow in Standard Medium-Power Shots

The goals in developing the SMP shots were to find operating parameters (plenum pressure, plenum temperature, beam voltage and nozzle current) that would be reproducible while ensuring that the airflow remained supersonic during the entire duration of e-beam injection. To verify that these shots remained supersonic, shadowgraph measurements of the flow Mach angle were taken for these types of shots. Representative examples taken with the PSI high framing rate camera are shown in Figs 7.1 and 7.2 below. This camera had the capability of capturing 28 frames at up to 1 MHz rates. For these applications the camera was run so that the 28 frames encompassed a short time before the electron beam was turned on and the time evolution of the flow during the electron beam heating period. A scribe was placed in the flow and acted as a sting that generated a shock wave that traversed the heated region. The shadowgraph of that shock was observed with the high framing rate camera. Typically, the shock generated by the sting could be seen in all 28 frames of the data encompassing the entire duration of the SMP e-beam injection. When the injected power was raised well above the 300 - 400 kW level employed for these SMP shots, the shock angle was observed to approach 90 degrees and the associated shadow was seen to disappear as would be expected when the flow was driven subsonic.

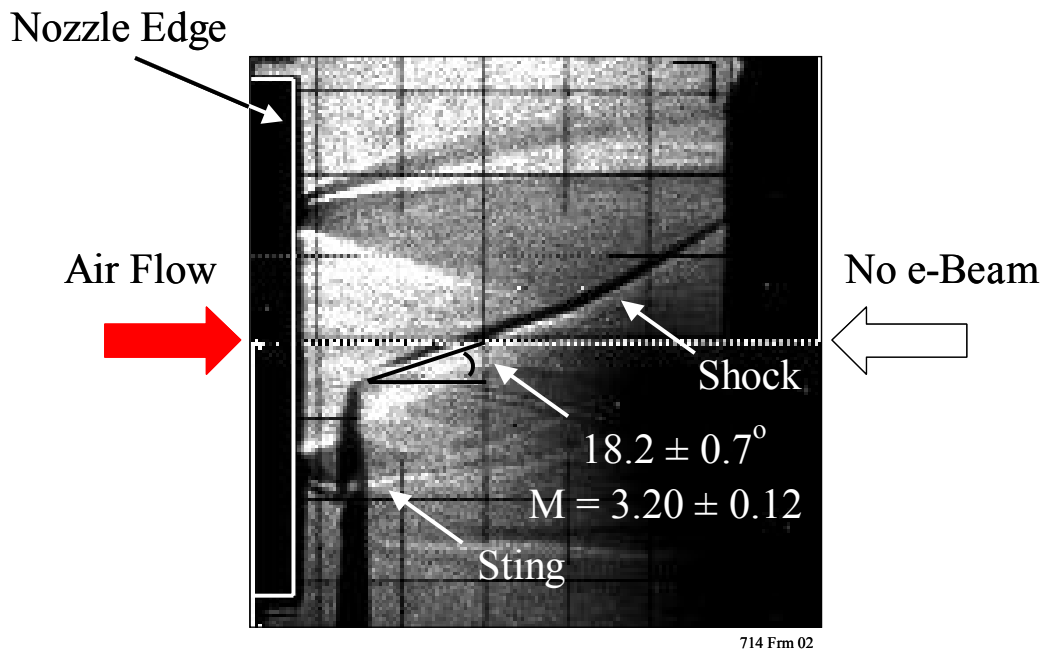


Figure 7.1: This shadowgraph was taken during an SMP blowdown just before e-beam injection. A clear and stable shock wave is seen emanating from the sting. The Mach number calculated from the measured shock angle for this flow was 3.20 ± 0.12 . The error was estimated from the uncertainty in the measurement of the angle as shown above.

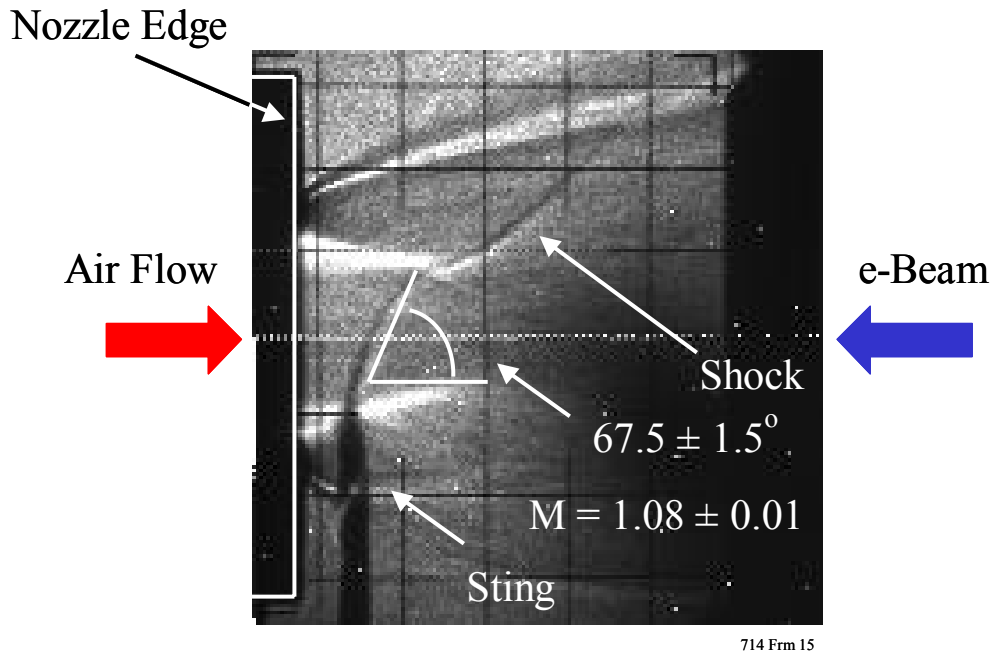


Figure 7.2: This shadowgraph was taken during the same blowdown as above but well after the establishment of steady airflow during e-beam injection. A clear and stable shock is still seen and indicates that the flow remains supersonic. The calculated Mach number for this flow was 1.08 ± 0.01 .

The Mach number for the unheated SMP blowdown discussed in Fig 7.1 was calculated from the measured shock angle to be 3.20 ± 0.12 . The predicted value using the invicid Euler code discussed above was 3.21. The measured steady-state Mach number taken during e-beam injection was 1.08 ± 0.01 (Fig 7.2). The predicted value for this shot was 1.43. This represents a 29 percent difference between prediction and experiment. Hence it appears that more heating was taking place in these SMP shots than was predicted by the Euler code.

In order to study the increase in nozzle pressure due to SMP e-beam injection, a careful selection of well-behaved shots was undertaken. SMP shots that had nearly identical current during the initial period of heating were chosen for study. The nozzle currents for three such standard shots are plotted in Fig 7.3. As can be seen, in each case the current remained reasonably constant for the first 2 ms of e-beam injection. The change in nozzle pressure as measured by the five Oprand transducers during SMP e-beam injection for each of these shots was found to be so reproducible, for the first 2 ms, as to be considered virtually identical, channel-by-channel. The data from these three shots was, therefore, averaged in order to increase the signal-to-noise ratio of the measurement. In Fig 7.4 are shown the average measured pressure increases for these shots.

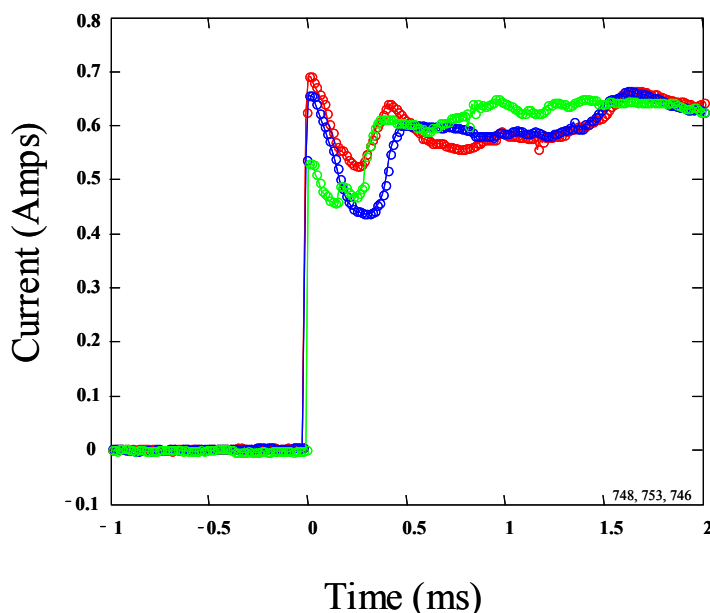


Figure 7.3: The measured nozzle currents for three SMP shots chosen for study.

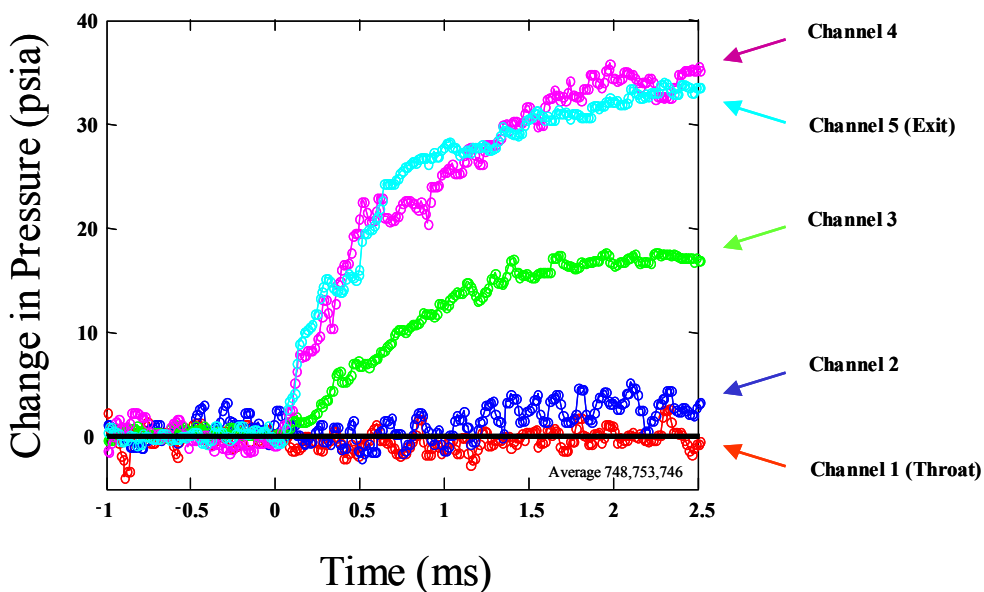


Figure 7.4: The average measured pressure increases from all five Optrand channels. The injected power for all three shots was about 380 kW. Virtually no differences were seen in the pressure data from shot to shot for these three blowdowns.

A few salient features can be seen in Fig 7.4. The depth of e-beam penetration may be determined by noting that a pressure rise can be seen on four of the five Optrand channels. A small pressure increase was seen on the channel 2 transducer located 25.2 cm from the nozzle exit (see Fig 2-A1 and Table 1-A1). Hence the beam penetration exceeded 50 percent of the nozzle length for these shots. It may also be seen that the pressure rise seen in channel 4 is larger

than that seen in channel 5 at the nozzle exit. This observation is consistent with the numerical predictions described below.

One of the well-behaved SMP shots discussed above was chosen in order to compare numerical predictions against experiment. The particular shot chosen (shot 746/4371) was heated with 7 ms of e-beam injection and exhibited large variations in the nozzle current *after* the first 2 ms of injection. Using the time-dependent approach outlined in Appendix A6, the increases in nozzle pressure due to e-beam injection were modeled taking the measured temporal variations of the nozzle current into account.

Two results of the SMP modeling work are presented below. (1) In Fig 7.5 are shown the measured and predicted steady-state nozzle pressures with and without e-beam heating. The data are plotted as a function of position along the nozzle axis as measured from the throat. The steady-state values for the heated cases were generated by averaging the injected power over the time interval 1 - 2.5 ms when the nozzle current was nearly constant (See Fig 7.3). (2) In Fig 7.6 is a comparison of the numerical simulations shown against the pressure data from shot 746/4371. It is interesting to note that the time-dependent model captures the dynamic features seen in the data. The model further predicts that the channel 5 pressure exceeds the channel 4 data as was seen in data and noted above.

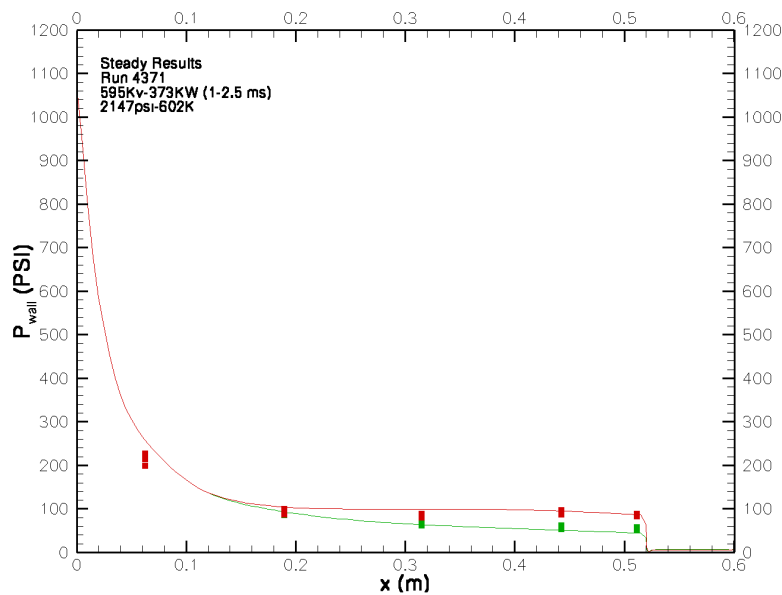


Figure 7.5: The predicted steady-state nozzle pressures for an SMP shot compared against the pressures measured using the Optrand transducers. Both the unheated and the heated cases are shown. The injected e-beam power for this blowdown was 383 kW. The predictions are shown as solid colored lines, green for the unheated case and red for the heated case. The measurements are shown as points (representing the high and low values of the data) with the corresponding color. The uncertainty in the measurements is represented by the vertical extent of the points and is mostly due to the slow thermal drift experienced by the pressure transducers (see Appendix A5).

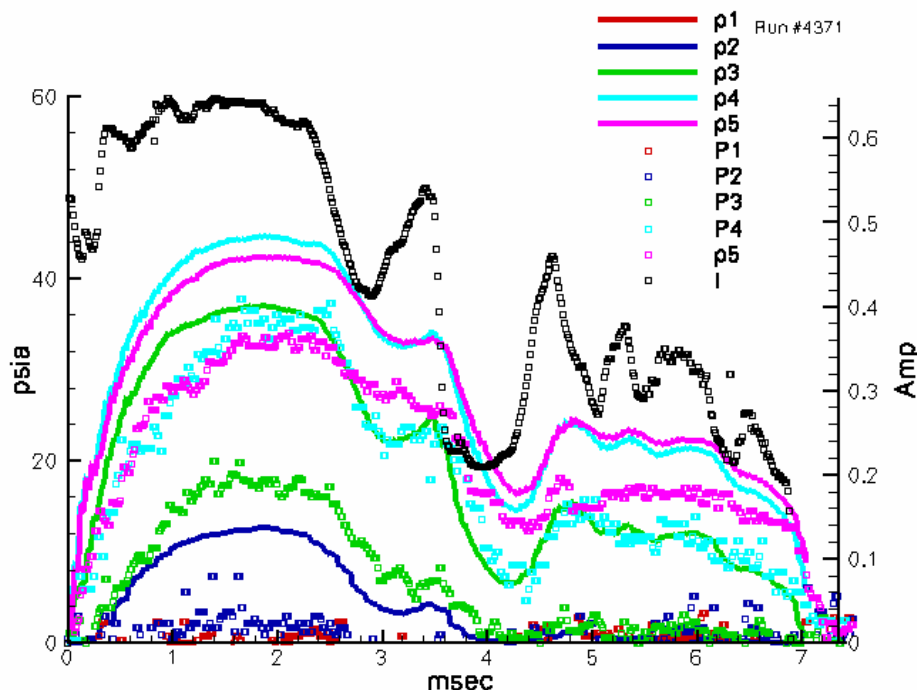


Figure 7.6: The predicted and measured nozzle pressure increases for shot 746/4371, an SMP shot. Also shown in black is the measured nozzle current. The experimental data is shown channel-by-channel as colored points while the corresponding predictions are shown as solid lines of the same color. A color legend is also shown in this diagram in which p1 represents the pressure measured/predicted at the transducer station nearest to the nozzle throat and p5 is measured/predicted nearest to the exit. For this 7-ms shot, the current was approximately constant for the first 2 ms of injection, long enough for steady-state airflow to be established.

The numerical modeling also allows for predictions about the flow velocity in SMP shots with and without heating. Shown in Fig 7.7 are reduced data from the direct spark velocimetry diagnostic described in Appendix A5. The data points shown represent displacements measured while tracking downstream the images of a laser-induced plasma introduced into the airflow just in front of the nozzle exit. The direct spark velocimetry technique was used to characterize both heated and unheated flow as compared to the shadowgraph/spark method that was only effective for unheated airflow (as discussed in section 6 above). A few images of the plasma luminosity used to generate the Fig 7.7 data points are shown in Fig 6–A5 of Appendix A5. In Fig 7.7 the reduced velocimetry data are shown for two SMP shots having identical plenum conditions. The blowdown without e-beam heating (shot 741) can be seen to have a velocity of 959 ± 63 m/s. The data associated with e-beam heating was taken from shot 746/4371, the same well-behaved 380 kW SMP shot that was analyzed above. In this case the laser-induced plasma was introduced 2.5 ms after the start of e-beam injection. The measured on-axis flow velocity can be seen to be 926 ± 80 m/s. The two measured velocities are hence within 3.5 percent of each other and can be considered equal within the experimental errors. These measured values compare reasonably well to the value of 907 m/sec predicted using the invicid Euler code and the value 942 ± 30 m/s determined by shadowgraph/spark velocimetry (see Fig 6.3).

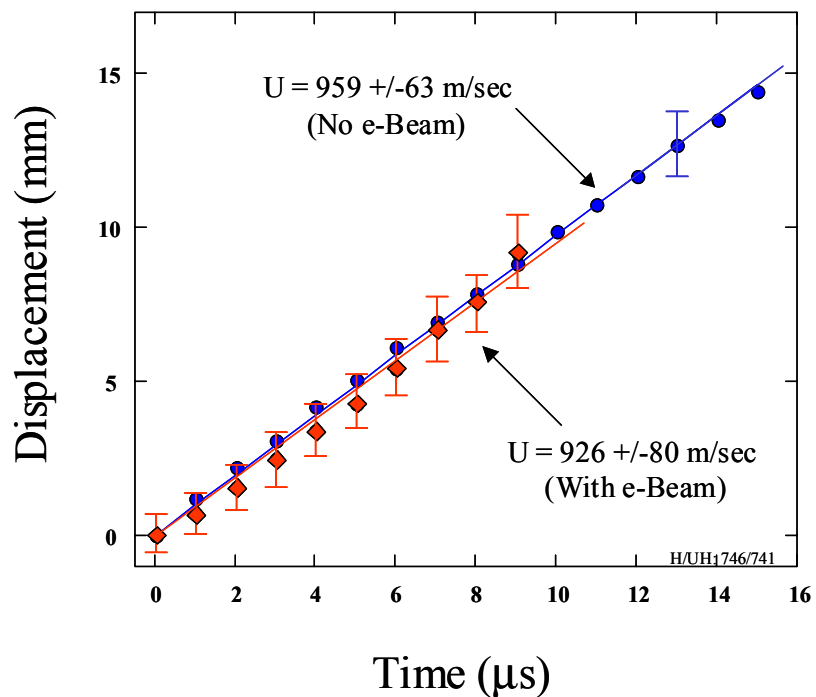


Figure 7.7: The flow velocities determined by direct spark velocimetry. Some of the images associated with this diagram can be seen in Appendix A5, Fig. 6-A5.

Predictions about the flow structure of SMP blowdowns were also compared to measurements. In Fig. 7.8 is shown a shadowgraph with predicted angles for the expansion wave and the jet boundary superimposed on the picture.

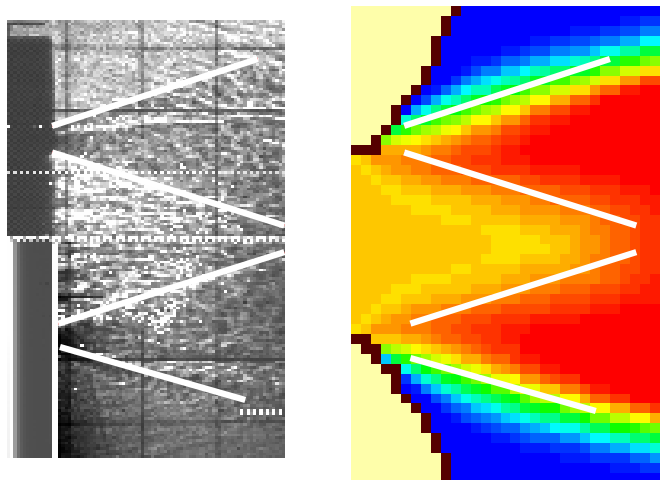


Figure 7.8: Predictions about the structure of the airflow near the nozzle exit are compared to a shadowgraph taken during an unheated SMP blowdown.

Predictions about the air density during SMP shots were also attempted. Rayleigh scattering measurements were taken during SMP shots both with and without e-beam heating. Shown in Fig 7.8 below are two measured Rayleigh scattering profiles. The first profile was measured $2\ \mu\text{s}$ before e-beam injection. The second profile was measured $1.6\ \text{ms}$ after the start of injection and, therefore, near in time to the establishment of steady-state airflow conditions. Also shown in this diagram are simulations of the air density calculated from the Euler code.

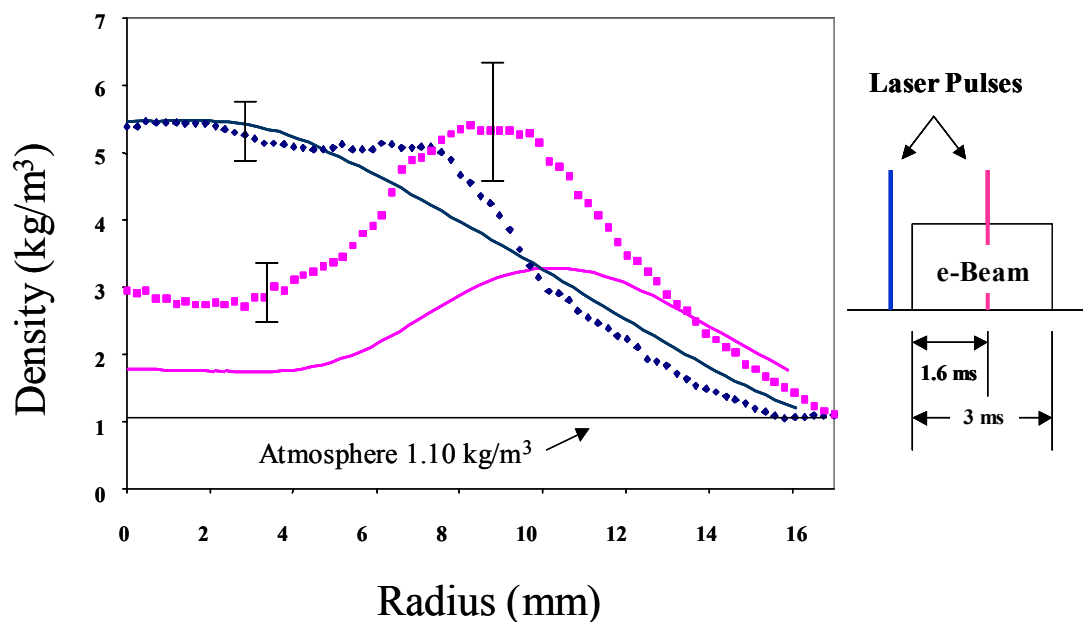


Figure 7.9: The air densities from Rayleigh scattering measurements taken $2\ \mu\text{s}$ before e-beam injection and $1.6\ \text{ms}$ after the start of SMP injection. The blue curves represent the unheated cases and the purple curves represent the heated cases. Experimental data are shown as points while the simulations are shown as lines. The error bars represent the shot-to-shot variability in the Rayleigh profiles for shots having identical plenum conditions and similar injected power.

It may be noted in Fig 7.9 that the agreement between measurements and predictions is fairly good in the unheated cases but poor in the heated cases. This is thought to be due a systematic error in the calibration process as discussed in Appendix A5. Hence quantitative information derived from Rayleigh scattering data is not considered to be reliable.

A summary of the measurements and predictions discussed above and pertaining to well-behaved SMP shots is given below in the form of two tables. In Table 7.1 are shown the predicted and measured values of parameters for the case of unheated airflow. Shown in Table 7.2 is a comparison for the e-beam heated case. It should be noted that in Table 7.2 the *change* in pressure at the nozzle exit due to the heating of the e-beam is listed while in Table 7.1 the value of the unheated exit pressure is given.

Table 7-1: A comparison of the predicted and the measured airflow properties for the case of an unheated SMP shot. The diagnostics employed to make the measurements are also indicated; they as follows: (a) shadowgraph, (b) shadowgraph/spark velocimetry, (c) direct spark velocimetry, (d) Optrand transducer, (e) Rayleigh scattering. The plenum conditions are also summarized.

Plenum: P=2147 psi T = 605 K	Mach Number	Flow Speed (m/s)	Sound Speed (m/s)	Pressure @ Exit (psi)	Density @ 17 mm (kg/m ³)	Enthalpy (MJ/kg)
Predicted Values	3.21	907	283	45.16	5.44	0.74
Measured Values	^a 3.20±0.12 ^b 3.05±0.26	^c 959±63 ^b 943±30	^b 309±25	^d 53.5±5.2	^e 5.5 ± 0.8	0.82±0.08

Table 7-2: A comparison of the predicted and measured airflow properties for the case of an SMP shot with 380 kW of heating. The indicated diagnostics are as given in Table 7-1 above.

Plenum: P=2147psi T = 605 K	Mach Number	Flow Speed (m/s)	Sound Speed (m/s)	ΔPressure @ Exit (psi)	Density @ 17mm (kg/m ³)	Enthalpy (MJ/kg)
Predicted Values	1.43	907	635	41.24	1.97	1.64
Measured Values	^a 1.08±0.01	^c 926±80	-----	^d 31.5±2.0	^e 2.8±0.5	2.76±0.50

A power accounting was also accomplished for the well-behaved SMP shots discussed above. For these shots with moderate injected power (380 kW) it has been observed that about 95 percent of the beam power from HAWK was absorbed by the airflow.

In order to confirm the amount of power absorbed in the flow, a simple expression for the total power absorbed is given. The power can be determined by the difference between the total power of the flow with and without heating at the exit of the nozzle:

$$Q^{\circ} = \int [\rho u H]_h - [\rho u H]_n dA$$

Where Q° is the power absorbed by the flow, ρ is the density, u is the velocity, and A is the nozzle exit area. The subscript h refers to the heated case and n refers to the unheated case [6]. Numerical simulations show that the difference in flow velocities between the heated and the unheated case should be negligible and the velocity measurements discussed above have

demonstrated this point (Fig 7.7). Moreover, since the pressure is essentially constant across the nozzle exit, the power added to the flow is given by the following simple expression:

$$Q^o = u \frac{v}{v - 1} \Delta p A$$

Where v is the specific heat ratio, Δp is the exit pressure difference between the heated and the unheated flow, and A is the nozzle exit area.

Applying the expression given above to one of the well-behaved SMP shots (746/4371), where the velocity was measured to be $u = 926 \pm 80$ m/s and the measured change in pressure at the exit was $\Delta p = 31.5 \pm 2$ psia, the calculated total power added to the flow is 363 ± 36 kW. This value is in good agreement with 383 ± 30 kW, the value calculated from measurements of the HAWK voltage and the nozzle current. The ratio of these two powers is 0.95 ± 0.12 . Hence, at least for the well-behaved SMP shots, the measured power leaving the HAWK accelerator has been accounted for as having entered the airflow. It thus can be demonstrated that, for medium power shots, the product of the nozzle current-to-ground and the accelerator voltage is a good measure of the power actually delivered from HAWK.

Airflow in High-Power Shots

Because the nozzle current of the shots with power > 450 kW exhibited large fluctuations over the entire duration of e-beam injection, those high-power shots were more difficult to characterize and more challenging to simulate by computational fluid dynamics (CFD). An example of a high-power shot that was chosen for study because it was reasonably well behaved is shown in Fig 7.10 below. In this diagram are shown the measured changes in nozzle pressure for shot 699/4311 as a result of e-beam injection. Also shown in this diagram is the nozzle current. The maximum power in this case was about 700 kW and the fluctuations in current were considered moderate as compared to other high-power shots (see the high current shots shown in Fig 6.1). The measured increases in nozzle pressure show some interesting behavior. Initially, the e-beam can be seen to penetrate very deeply into the nozzle because a transient pressure rise is observed on Optrand channel 1 located only 6.3 cm from the nozzle throat. The pressure rise seen in this channel subsides after about 1 ms. It should be noted that the predicted rise in pressure for this channel was zero. Hence it appears that the e-beam penetrates deeper than predicted if only transiently.

It may be noted that, even though the current fluctuations are moderate, there is no time during e-beam injection when the current delivered to the nozzle may be considered constant (as contrasted against the SMP cases discussed above). This particular shot is also interesting because the nozzle pressures measured toward the exit (channels 3, 4 and 5) reach a clear steady state for 2 - 2.5 ms. Because the blowdown airspeed has been measured to be about 930 m/s, this 2 - 2.5 ms steady state represents 4 - 5 generations of fluid particles passing through the nozzle without the development of a beam-induced instability.

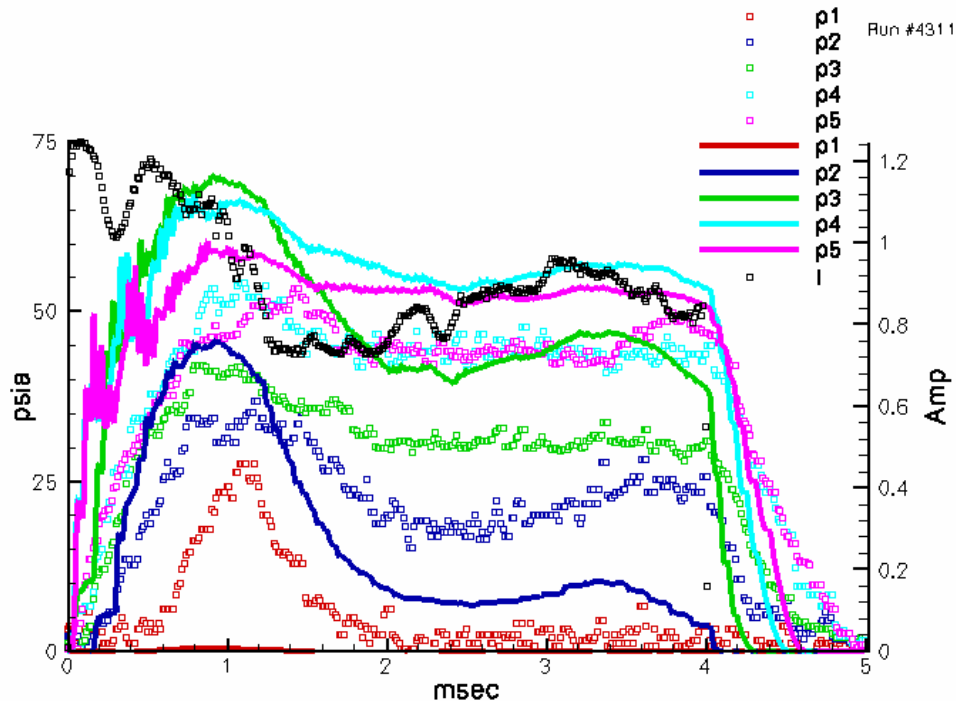


Figure 7.10: The measured and predicted increases in nozzle pressure for a reasonably well-behaved high-power shot (shot 699 / 4311). The experimental data is shown channel-by-channel as colored points while the corresponding predictions are shown as solid lines of the same color. The measured nozzle current is shown in black. A color legend is also shown in this diagram in which p1 represents the pressure measured/predicted at the transducer station nearest to the nozzle throat and p5 is measured/predicted nearest to the exit. In this particular shot the current varies greatly for the first 1-2 ms of injection and subsequently becomes more steady.

The modeling also allowed for predictions to be made about the steady-state behavior of the high-power shot shown in Fig 7.10 above. As an example shown in Fig 7.11 below are the measured and predicted steady-state nozzle pressures with and without e-beam heating for shot 699 / 4311. This shot had an initial injected power of 700 kW that fell to about 480 kW as the current became more steady after the first 2 ms of e-beam injection (see Fig 7.10).

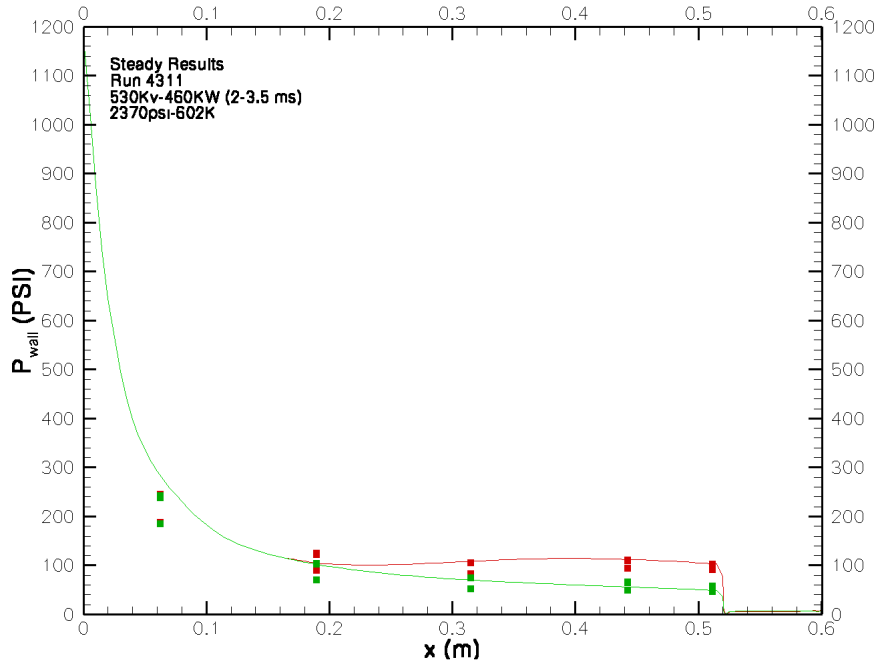


Figure 7.11: The predicted steady-state nozzle pressures for shot 699/4311 compared against the pressures measured using the Optrand transducers. Both the unheated and the heated cases are shown. The injected e-beam power for this shot started at 700 kW but fell to about 480kW after the first two ms of injection. The steady-state values for the heated cases were generated by averaging the injected power over the time interval 2 - 3.5 ms when the nozzle current was fairly steady constant (See Fig 7.10). The predictions are shown as solid colored lines, green for the unheated case and red for the heated case. The measurements are shown as dual points (high and low values) with the corresponding color. The uncertainty in the measurements is represented by the vertical displacements of the dual data points and is mostly due to the slow thermal drift experienced by the Optrand pressure transducers (see Appendix A5).

As demonstrated in Figs 7.5, 7.6, 7.10 and 7.11 above as well as in Tables 7.1 and 7.2, the results of the inviscid modeling, wall pressure, exit Mach number, exit velocity, and density profile, compared fairly well to the measurements in the unheated cases. On the other hand, for the heated cases, the predicted pressure fluctuations closely follow the measured pressure fluctuations but with a different amplitudes.

Rayleigh Scattering in High Power shots

Rayleigh scattering measurements were taken during several high-power shots. A four pulse frequency doubled Nd:YAG laser was used, along with the PSI high speed framing camera. Examples of Rayleigh images are shown in Fig 7.12 below.

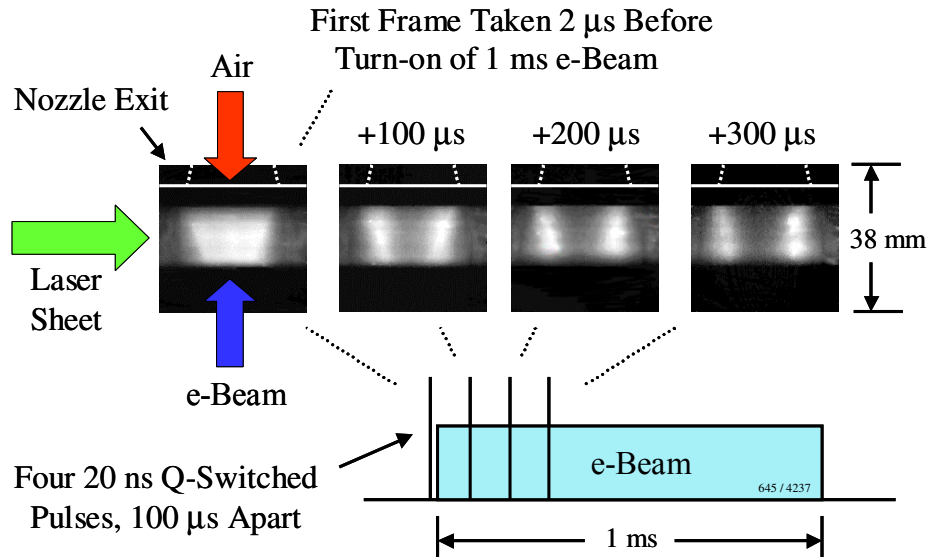


Figure 7.12: Rayleigh scattering images taken during a high-power shot. The laser beam incident from the left took the form of a sheet 1 mm thick \times 1.5 cm wide.

Unfortunately, at the time when most of the Rayleigh measurements were made, the high-pressure dielectric union that served to isolate (i.e. float) the nozzle/magnet system from electrical ground was malfunctioning. The measurements, therefore, cannot be compared to predictions because no measurement of the nozzle current exits for these high-power shots was made. Some semi-quantitative information can, however, be gleaned from these measurements. In particular, the first Rayleigh image shown in Fig 7.12 was taken 2 μ s before the injection of a high-power e-beam. A converging expansion wave may clearly be seen in this initial image. The remaining three images were taken at 100 μ s intervals after the start of heating. Clearly, the central density decreases and the edge density increases immediately upon the start of injection. All frames in Fig 7.12 were taken within 300 μ s of the start of heating. It is interesting to note that because the transit time of air particles in the nozzle is about 500 μ s, the observed deep collapse of the central density takes place well before the first generation of air particles leaves the nozzle after the start of e-beam heating.

The initial e-beam voltage for the case shown in Fig 7.12 was 604 kV and the HAWK current measured internally was 1.26 amps. Hence this particular shot had a nominal initial power of 760 kW.

NO Production in High-Power Shots

Spectral UV-absorption measurements were performed to quantify line-of-sight NO concentrations slightly downstream of the nozzle exit plane. The measurements, assumptions and results are described further in Appendix A5. No absorption was observed during the experiments using SMP shots. This lack of absorption can be attributed to both the intrinsically

low NO concentrations present in SMP shots as well as problems with the measurement resulting from the shallow penetration depth of the SMP e-beam into the nozzle. As a result, the NO-UV measurements are not adequate for quantifying NO concentrations at low-to-medium power conditions.

In order to maximize the likelihood of detecting NO, a set of operating parameters was chosen that resulted in high-power shots penetrating extremely deep into the nozzle (as discussed in Section 6 above). Shown in the Fig 7.13 are the measured increases in nozzle pressure for shot 728/4358, a shot that was developed to maximize NO production. Also shown in this diagram is the measured nozzle current to ground. This shot received a stable injected power of about 813 kW over the entire 1.2 ms duration of e-beam injection. The depth of e-beam penetration can be discerned by noting that all five Optrand channels exhibited pressure increases in the range of 40-60 psia. Hence, the e-beam for this shot can be said to have penetrated the entire length of the nozzle.

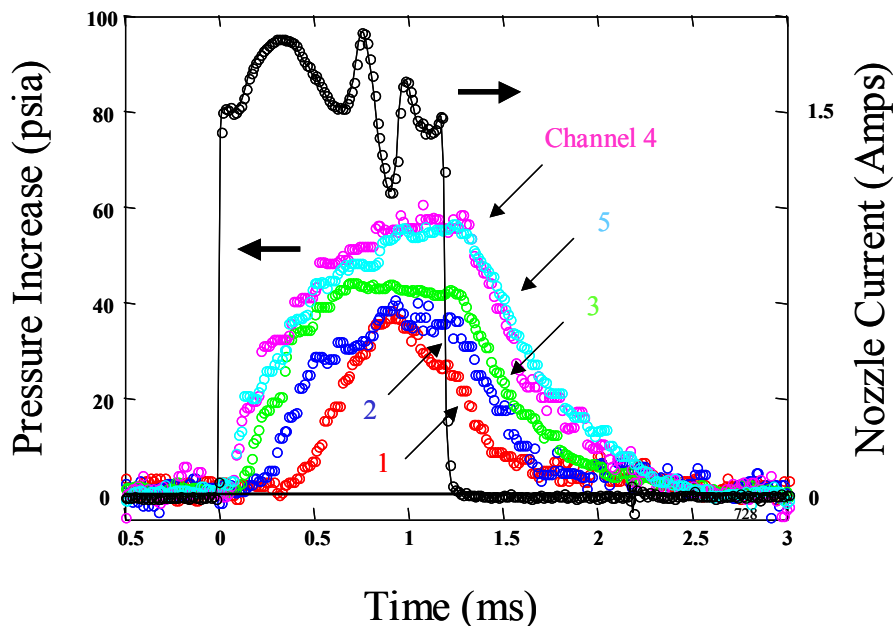


Figure 7.13: The measured increases in nozzle pressure as a result of deeply penetrating e-beam injection in a shot designed to maximize NO production. The maximum power attained during this shot was 926 kW. The power averaged over the entire duration of e-beam injection was 813 kW. Also shown is the measured nozzle current to ground.

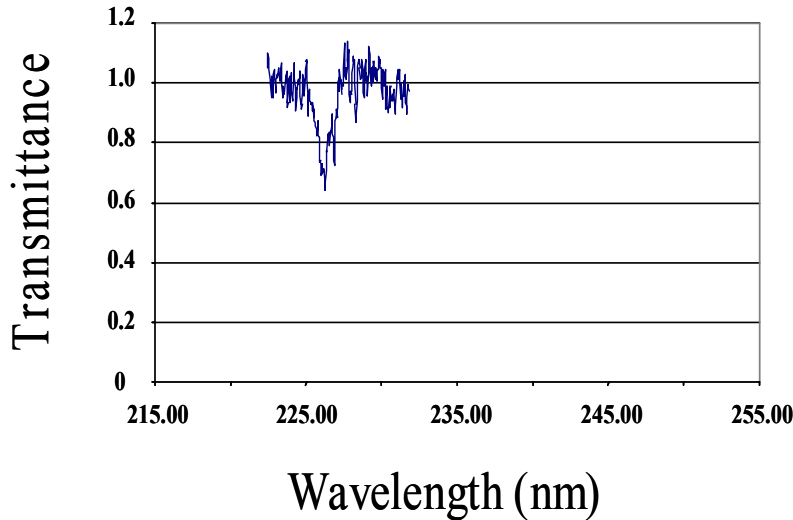


Figure 7.14: The transmittance measured during shot 728/4358 showing a thirty percent drop due to the presence of NO.

NO-UV absorption measurements were made after the e-beam shutoff but during the time e-beam heated air was still exiting the nozzle. The timing of the measurements is explained in detail in Appendix A5. Absorption due to NO was obvious at 226 nm as shown in the example spectrum in Fig. 10-A5 and the corresponding transmittance curve in Fig. 7.14. The measured NO-UV transmittances from shot-to-shot ranged from 0.67 to 0.83 during the high-power shots investigated.

The NO line-by-line radiative transfer modeling code, employed to deduce NO number density from the NO-UV measurement, required an independent determination of radial and axial static temperature and static pressure profiles. Data from other diagnostic measurements, however, were not adequate to provide the temperature and pressure profiles. The Princeton University CFD model was, therefore, used to provide estimates of static pressure and static temperature at the nozzle exit ~ 0.25 ms after e-beam shut down using the simulated run (shot 699/4311) and the experimental pressure history for shot 728/4358. The CFD estimates were $P_{\text{exit}} = 5.92 \pm 0.59$ atm and $T_{\text{exit}} = 1100 \pm 200$ K.

The radial profiles of static temperature and pressure for the three distinct axial locations of the 3-pass UV-beam would ideally be used as inputs to the NO radiative transfer model. Additional Princeton CFD calculations, however, predicted negligible fall-off of properties along the axis within the NO-UV measurement region. Thus, the flow-field in the region of the measurements was treated as a single homogeneous zone of constant temperature, pressure and NO number density.

The NO number density was calculated for shot 728/4358 using the estimated conditions described above and assuming an absorption path length of 7.62 cm (3 passes times 2.54 cm). The NO number density was $3.70\text{E}+16$ ($\pm 12\%$) cm^{-3} for the measured transmittance 0.70 ± 0.03 .

The NO-UV measurements determined the NO number density for a fixed path length. To convert the number density to a fractional concentration, the total number density was calculated using the ideal gas law and the estimated static temperature and pressure. The fractional NO concentration using the estimated 5.92 atm static pressure and 1100 K static temperature was calculated to be 0.0010 ± 0.0003 . Thus, treating the measurement volume as a

homogeneous medium gives about 0.1% NO, recognizing assumptions and approximations in deriving this result. A more detailed description of the NO measurements is given in Appendix A5.

Enthalpy Addition in High-Power Shots

Using the high-power shot discussed above (shot 728/4358, see Fig. 7.13) an estimate of the percentage increase in enthalpy attained during the 1 MW experiments can be made. Specifically, since the final stagnation enthalpy, H_{of} , at the nozzle exit is simply the initial stagnation enthalpy, H_{oi} , in the plenum plus the heat added per unit mass. We can write:

$$H_{of} = H_{oi} + \frac{Q}{\dot{m}} = H_{oi} + q$$

Where Q is the power absorbed by the flow, \dot{m} is the mass flow rate, and q is the heat added per unit mass. The total enthalpy ratio is, therefore:

$$\frac{H_{of}}{H_{oi}} = 1 + \frac{q}{H_{oi}}$$

An initial injected power of 926 KW was attained in shot 728/4359 while the power averaged over the 1.2 ms e-beam duration of was 813 kW. The corresponding ratio $\frac{H_{of}}{H_{oi}}$ thus attained a maximum value of 3.0 and an average value of 2.76. Both of these numbers compare well to the value of 2.79 envisioned for the MSHWT.

8. Results and Conclusions

The following is a summary of the conclusions drawn from the research described above compared against of the objectives of the experiment:

1. To attain an input power of 1 MW using e-beam energy of 1 Mev and current of 1 Amp
 - Injected powers exceeding 890 kW were attained using beam energies in the neighborhood of 600 keV and currents of approximately 1.5 Amps.
2. To demonstrate bending of the e-beam sufficient to avoid impingement of the high-temperature airflow generated during the experiments on e-beam delivery components
 - Bending of the electron beam through 45 deg was successfully demonstrated.
3. To demonstrate the extraction of the e-beam through a gasdynamic window. This was to incorporate the plasma porthole concept proposed by Brookhaven Laboratory.
 - While the plasma porthole technology proved unsuccessful, an alternative approach was developed using a ruptured diaphragm, a fast acting valve and differential pumping. This proved successful with a window diameter of four millimeters.
4. To demonstrate the efficient extraction and focusing of an e-beam from an annular cathode immersed in a magnetic field
 - The annular cathode concept was successfully demonstrated for the production of a quasi top-hat energy deposition profile.
5. To attain an enthalpy ratio comparable to that envisioned for the MSHWT (2.79)
 - At high powers (approximately 900 kW), the enthalpy ratio h_{of}/h_{oi} was 3.0, exceeding the requirement for the MSHWT (2.79). No indications of flow instability were detected in the wall pressure measurements.
6. To validate energy deposition and e-beam steering models
 - In the unheated case, measurement of nozzle wall pressure, exit Mach number, velocity, and also density profile (Rayleigh scattering) were in close agreement with predictions, see Table 7.1.
 - For the medium power shot (380KW) and the high power shot (750KW), which were modeled in detail, the beam current was fluctuating in time; the measured nozzle wall pressure fluctuations correlated closely with the beam current fluctuations. The predicted pressure fluctuations also closely follow the measured pressure fluctuations but with an amplitude at each station along the nozzle that was different in detail from the measured amplitude (see Figs. 7.6

and 7.10). The reason for this difference could not be ascertained particularly because no measurements were made of the beam current density profile, *in situ*. A difference in beam penetration was also observed but the significance of this difference is not certain and it was not possible to determine its cause. The predictions were based on the assumption that the boundary layer displacement thickness was the same in both the heated and the unheated cases. An additional viscous calculation gave some improvement in the agreement between prediction and experiment for the steady, heated case. Further experiments are now needed with a steady beam current of known profile before the models can be more adequately validated.

7. To establish the effect of the e-beam on the chemistry of the heated air

- While there is uncertainty, the absorption measurements indicate an NO mole fraction of 0.1% in the high power case.

8. To gain an understanding of the e-beam current return path

- Efforts to find any current path from the beam to ground other than through the nozzle wall were unsuccessful (see Fig 7 – A5). It was also found for the medium power shot (380 kW) that the product of current to ground and accelerator voltage was close to the measured energy flux in the flow.

9. To observe whether or not arc discharges occur in the nozzle

- No spikes in the current to ground from the nozzle were found and the nozzle remained pristine and undamaged by any current discharge. Thus no discharge arc was found.

Further Conclusions

1. Concerning the diagnostics

- The measurement of the static pressure, velocity and the Mach number were successful. Calibration of the Rayleigh scattering measurements during e-beam deposition was not achieved with sufficient precision.
- In future experiments a diagnostic technique to measure the beam current density profile prior to absorption in the flow will be required.

2. Concerning the HAWK Accelerator

- Medium power shots (380 KW) provided some cases for which the beam current was reasonably stable. The fluctuations in beam current are believed to be due to the scraping of the beam on internal apertures. This is speculated to be due to vibration. It proved to be a major limitation in the acquisition of data and in the validation of models.

9. Future Work and Possible Improvements

The most critical improvement required for future experiments is in the design of the new accelerator that will allow for operation at voltages up to 1 MV and for delivery of current to the nozzle without significant fluctuations. This new accelerator is currently being built under contract to Sandia. In addition, some method of measuring the electron beam profile during the run will be critical. The models are very sensitive to the electron beam profile, and any changes in that profile will lead to significant disagreement in the prediction of the penetration depth and the thermodynamic heating path of the air as it passes through the nozzle. The measurement of the distribution of the electron beam current return along the nozzle wall also need to be done as a check on the pressure measurement of the beam penetration. The time uniformity of that current deposition will also give another method to measure the stability of the energy addition process. Beyond these critical changes, there are opportunities to improve the existing air delivery system and the data collection procedure.

Rapid Blowdown / e-Beam Injection Scenario

Several improvements to the high-pressure air delivery system could be implemented in a reasonably straightforward manner. In particular, the duration of blowdowns can be shortened significantly from the current 2 second limit, and this shortening should lead to improvements in other areas such as the quality of the nozzle pressure measurements.

During most of the 1 MW experiments, an overshoot and subsequent recovery of the plenum pressure was routinely observed during the first second of all blowdowns (see Fig 1-A5). During the closing days of the experiments, however, it was found that the pressure overshoot could be eliminated. After changing the position of the sensing tap that controlled the master high-pressure regulator (Fig 1-A1), reproducible plenum pressures such as those shown in Fig 9.1 were attained. Apparently, moving the sensing tap closer to the dome-loaded regulator allowed for faster pneumatic feedback to occur within the regulator and this, in turn, allowed for the rapid establishment of a steady state plenum pressure. As demonstrated in Fig 9.1, the elimination of the pressure overshoot will allow future blowdowns to achieve steady state in about the first half-second after opening the high-pressure valve.

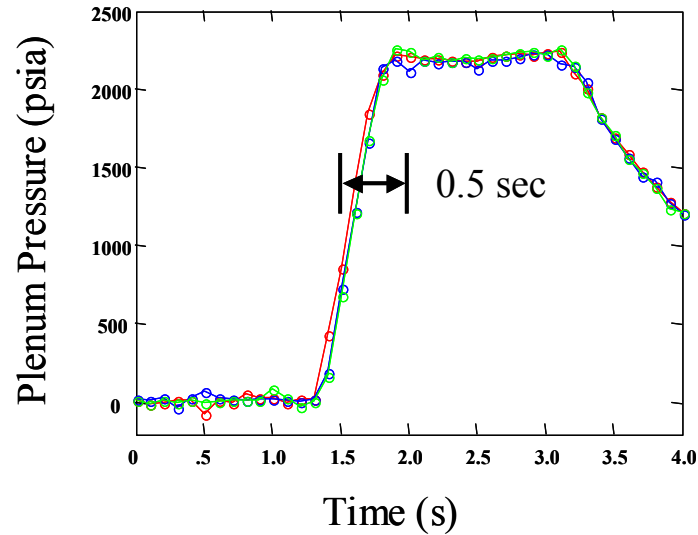


Figure 9.1: The measured plenum pressures for three consecutive blowdowns attained after repositioning the sensing tap on the master regulator.

In future experiments, the rapid establishment of steady-state plenum conditions could be exploited to improve significantly the slow measurements of the nozzle steady-state pressure. To understand this it is necessary to recall that the largest source of uncertainty associated with the nozzle pressure measurements was caused by the downward thermal drift experienced by the Optrand transducers when exposed to the hot air introduced into the nozzle during a blowdown (See Figs 3-A5 and 4-A5). By establishing a steady target pressure quickly, e-beam injection could be accomplished in the first 0.5 sec of the blowdown rather than having to wait for 1.1 - 1.3 sec as required previously (Fig 1-A5). This reduced wait time will decrease the Optrand thermal drift by decreasing the temperature rise experienced by the nozzle and the embedded Optrand sensor during a blowdown. It should here be noted that the reason e-beam injection had to be delayed for about 1.2 sec after the start of a blowdown was to allow the nozzle magnets the time needed to reach a steady-state field. The magnets, it will be recalled, were not triggered until the plenum pressure was measured to be above a threshold value (See Fig 4-A3). Hence, using the protocol of the experiments just concluded, the blowdown air had to be introduced into the nozzle for at least 1.1 secs before e-beam injection could be accomplished. This allowed the Optrand thermal drift to proceed for 1.1 sec before e-beam injection. By reducing this time to 0.5 secs a significant reduction of the drift should be achievable.

To accomplish this improvement, it will be necessary to change the Labmaster software to allow the magnets to fire about 0.6 sec *before* the high-pressure valve is opened and the blowdown begins. Under this new scenario, the plenum pressure and the nozzle magnet field will reach steady state simultaneously about 0.5 sec into the blowdown. This rapid blowdown/ e-beam injection scenario should not only allow for improved nozzle pressure measurements but should also result in significant reductions in the use of both high-pressure air and heat from the pebble bed heater.

The addition of a second set of pressure sensors to the nozzle located at the same axial stations as the Optrand sensors, but on the other side of the nozzle, is also recommended. These sensors will measure the same pressures as the Optrands. This second set of pressure sensors will be connected by thin tubing so that they can be located some distance from the nozzle and

thereby avoid the effects of the temperature fluctuation during the one or two second blowdown. Although they will have a slower response time because of the air volume in the thin tubes, they will be able to follow the pressure with enough time resolution to provide an independent measurement of the pressure at each Optrand station in the nozzle at the time of the electron beam injection. Thus the temperature drift of the Optrand sensors can be largely compensated and only the rapid change in pressure during the few milliseconds of run time will need to be followed by the Optrand sensors. During this short time, the temperature of the Optrand sensors is not expected to change significantly.

In the future, it would also be desirable to take steps in the laboratory that ensure the reliable start of blowdowns. As discussed above, delays as long as 2 sec sometimes occurred between the nominal opening of the high-pressure valve and the actual beginning of the airflow. While these delays proved to be completely benign using the version of Labmaster discussed above, such delays would be undesirable if the rapid blowdown / e-beam injection scenario were to be adopted in future experiments because they would lead to an aborted e-beam injection and the associated loss of air and heat.

Faster Collection of Slow Data

During the 1 MW experiments collection of the slow data was accomplished at a data rate of 10 Hz. The choice of this rate was driven by the fact that the diagnostic lasers employed during the experiment operated at a repetition rate of 10 Hz. It was convenient, therefore, to synchronize the lasers with the data collection because both were actuated at the same rate. Careful inspection of the slow data, however, has suggested that a 10 Hz data rate was slightly too slow to capture all temporal features present in the nozzle pressure measurements.

In addition, the correction of the Optrand data for the thermal drift discussed above would benefit from an increase in the slow data rate. Because the plenum pressure transducer did not exhibit thermal drift, all Optrand data was corrected by demanding that each nozzle pressure measurement be proportional to the plenum pressure. The constants of proportionality were assumed to be independent of temperature because they were measured during the first 400 ms after the start of the blowdown. During this period of rapidly rising pressure, a minimal amount of thermal drift could be expected because neither the nozzle nor the embedded transducers had sufficient time to heat up. The correction of the nozzle pressure data, therefore, relied on averaging the ratios of data taken over the critical 400 ms period. At a 10 Hz data rate, however, only four data points contributed to that ratio. Clearly, a better average can be constructed and, therefore, a more accurate correction could be achieved with more data points.

It is for the reasons given above that a slow data rate of perhaps 50 – 60 Hz would better meet the needs of future experiments. Some modification to the existing Labmaster software would be required to implement a higher data rate. In addition, a faster personal computer would be needed because a faster data rate will require that decisions be made more rapidly. The computer used to run Labmaster during the 1 MW experiments employed a 200 MHz CPU. In Fig 2-A3 the amount of CPU time needed to carry out the tasks performed by Labmaster is shown to be about 5ms, a small percentage of the 100 ms available between 10 Hz clock pulses. The latest generation of personal computers with CPU speeds in the 1 GHz range could easily make the same decisions in a small percentage of the 15 ms between clock pulses operating at (say) 60 Hz. Hence it appears realistic to increase the data rate into that range in future

experiments. Such an increase would be especially important if the rapid blowdown / e-beam injection scenario were employed.

References

1. R. Miles, G Brown, W. Lempert, R. Yetter, G.J. Williams, S.M. Bogdonoff, D. Natelson and J.R. Guest, AIAA Journal, 33, 1463 (1995)
2. A. Morgan, P. Barker, R. Anderson, G. Brown and R. Miles, AIAA-98-2498, 20th Advanced Measurement and Ground Testing Technology Conference, Albuquerque, NM, June (1998)
3. P. Barker, J. Grinstead, A. Morgan, R. Anderson, G. Brown, R. Miles, R. Lipinski, K. Reed, G. Pena, L.Schneider, AIAA-99-0688, 37th Aerospace Sciences Meeting, Reno NV, Jan 10, 1999.
4. P. Barker, J. Grinstead, P. Howard, R. Anderson, G. Brown, R. Miles, R. Lipinski, G. Pena, L. Schneider, R. Howard, AIAA-2000-0159, 38th Aerospace Sciences Meeting, Reno NV, Jan 10, 2000.
5. A. Herscovitch, "A Plasma Window for Transmission of Particle Beams and Radiation from Vacuum to Atmosphere for Various Applications", Physics of Plasmas, Vol. 5, No. 5, May 1998, pp 2130-2136.
6. P.Barker, P. Howard, B. Anderson, R. Miles, G. Brown, R. Lipinski, G. Pena, J. Grinstead, and R. Howard, "Proof of Principle Energy Addition Experiments for the RDHWT/MARIAH II Hypersonic Wind Tunnel," Paper #AIAA-2000-2276, 21st AIAA Aerodynamic Measurement Technology and Ground Testing Conference, Denver, CO, June 19-22, 2000.

APPENDIX A1: Details of the Air Delivery System

Clean, dry, compressed air was supplied to the experiments from a commercial tube trailer with a storage capacity of 124,000 ft³. The 2500 psi delivery pressure was boosted to 6000 psi with a Haskell model 56131 air-driven intensifier and stored in a tank farm of twenty size 1U compressed gas cylinders. The pneumatic drive consumed about twenty percent of the supplied air in this boost process. The tank farm capacity was greater than 26 ft³ and, when charged to 6000 psi, provided about 20 seconds of run time as the pressure dropped to 5000 PSI. The booster compressor was capable of replenishing this 20-second run time volume of air in about 6 hours.

The air was delivered to the test cell by a 1.5 inch schedule XXS stainless steel piping system that was acoustically and thermally insulated with two-inch rock wool insulation covered with an aluminum skin. Upon entering the test cell, the high-pressure air passed through a triple set of rotary joints to comply with thermal expansion requirements and a dielectric union fitting needed to allow nozzle current measurements. The airflow was started and stopped by computer control of a high-speed (requiring about 500ms to open) pneumatically operated master control valve equipped with a spring-operated fail-safe closed position. The 6000 psi delivery pressure was then reduced to 2650 psi with a dome-loaded pressure regulator. The regulator set point range of 500 to 3000 psi was controlled manually from outside the test cell with a dome-loader regulator mounted on a size 1U gas cylinder air supply. Downstream of the regulator, the piping size increased to two-inch schedule 160 stainless steel pipe. The air then passed through a “tee” fitting that employed a pressure relief valve set at the maximum allowable working pressure of 3000 psi in the branch leg. In the event of an overpressure condition, excess pressure was relieved through a three-inch schedule 40 vent pipe and directed safely from the building roof.

At this point the cold high-pressure air entered a spring-mounted pebble bed heater (ASE Inc.) that was preheated to 660°K. The heater employed electrical resistance band heaters operating at 6 kW and was designed for unattended operation. The storage media was a 40-inch - long 10-inch schedule 160 stainless steel pipe filled with ¼ inch stainless steel balls. The design heat capacity of the heater allowed for four six-second-long blowdowns per day with a temperature droop of about 30°K at a 3kg/sec flow rate. The heated air followed piping to the stagnation section that was fabricated from three-inch schedule 160 stainless steel pipe. A flange connected the stagnation section to an adaptor flange that held the nozzle and formed the upstream end of the nozzle / magnet assembly.

After exiting the nozzle, the heated air entered a diverter tunnel that cooled and directed the air upward toward the ceiling of the HAWK bay.

During the course of the experiments it became clear that, at the original design plenum pressure of 2650 psi, the maximum attainable plenum temperature was about 615 K, or 35 K lower than the original design temperature of 650 K. In order to increase the attainable plenum temperature, auxiliary heating was added to the “gooseneck” piping leading from the bottom of the pebble bed heater to the plenum (see Fig 4-A1 below). One kW of additional heating was supplied in the form of two resistive tubular heaters. At the same time that the auxiliary heating was added, a decision was made to operate the HAWK accelerator at lower voltage (600 – 700 kV) than was called for in the original plan (1 MV). Further, the nozzle was moved 10 cm away from the HAWK in order to accommodate the placement of an extra turning magnet between HAWK and the nozzle exit. This repositioning had the effect of adding more high-pressure air in

the e-beam path before it would penetrate the nozzle. In order to accommodate these changes and allow for penetration of the lower voltage e-beam into the repositioned nozzle, the operating pressure in the plenum was lowered from 2650 psi to about 2150 psi.

The net effect of adding auxiliary power to the “gooseneck” while simultaneously lowering the operating pressure of the plenum was that the new attainable plenum temperature was about 605 K at 2150 psi. For the reasons outlined above, after the auxiliary heating was installed, the air delivery system was not used at the original design pressure again; hence it is not possible to quantify the improvement to the plenum temperature brought about by the additional heating at the original operating temperature. It was observed, however, that as the plenum pressure was raised slightly above 2150 psi, the attainable plenum temperature rose slightly (on the order of 1 - 2 K per 300 psi increase in operating pressure).

The majority of subsequent useful shots were taken at a plenum temperature of 605 ± 3 K and at plenum pressures in the neighborhood of 2150 ± 50 psi.

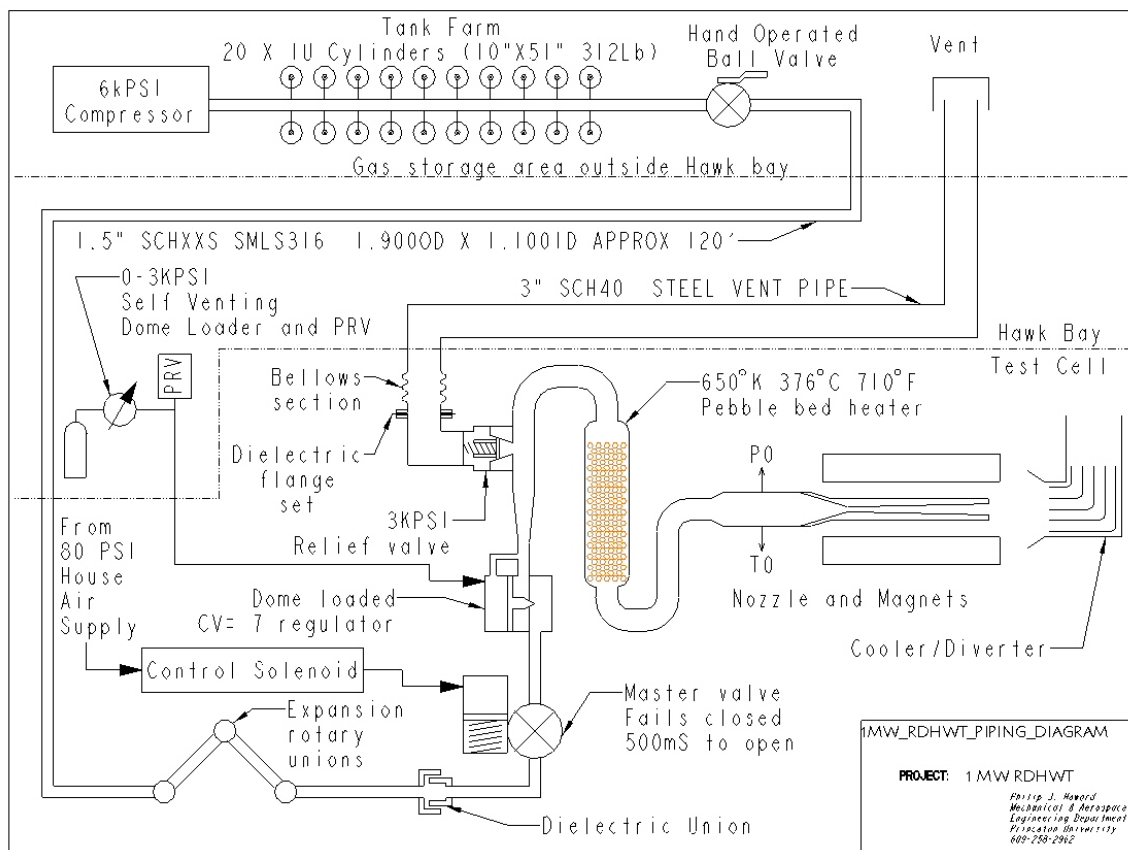


Figure 1-A1: The high-pressure air delivery system piping diagram

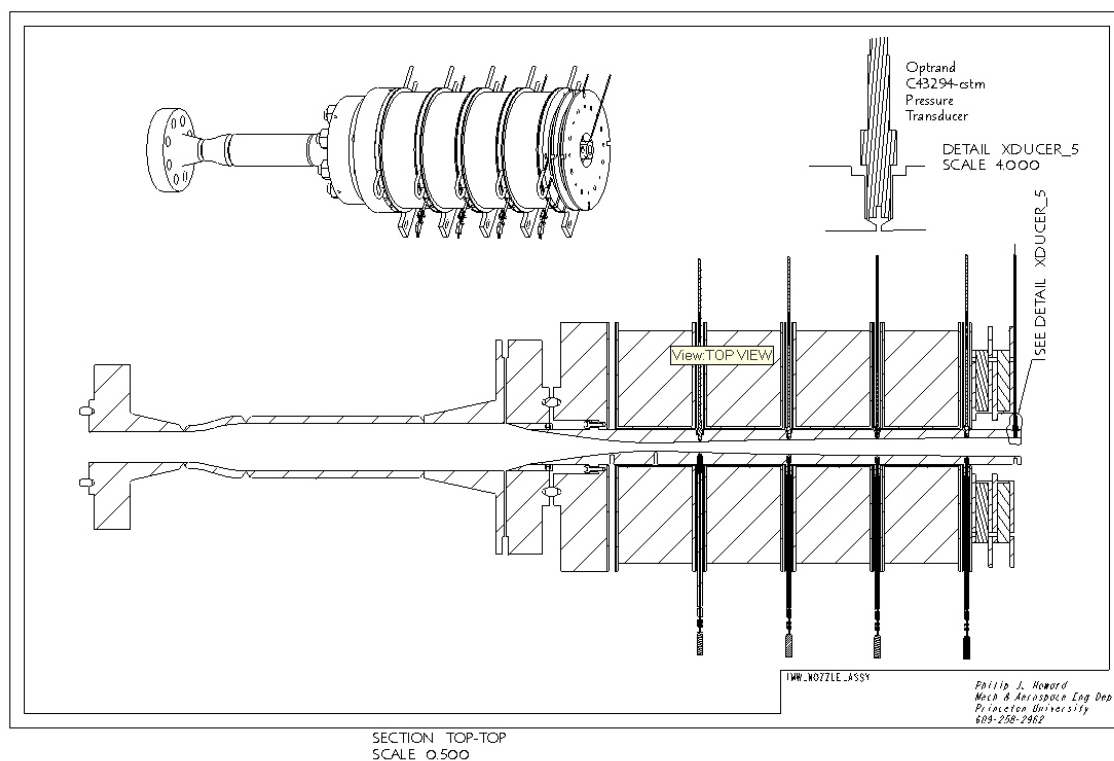


Figure 2-A1: The nozzle assembly shown embedded in the magnetic solenoids. The Optrand pressure transducers and the nozzle thermocouples are shown protruding through cooling plates that separate the individual solenoids.

Table 1-A1: Locations of the Optrand transducers and nozzle thermocouples as measured from the throat.

Channel #	1	2	3	4	5
Distance (cm)	6.281	18.96	31.53	44.25	51.16

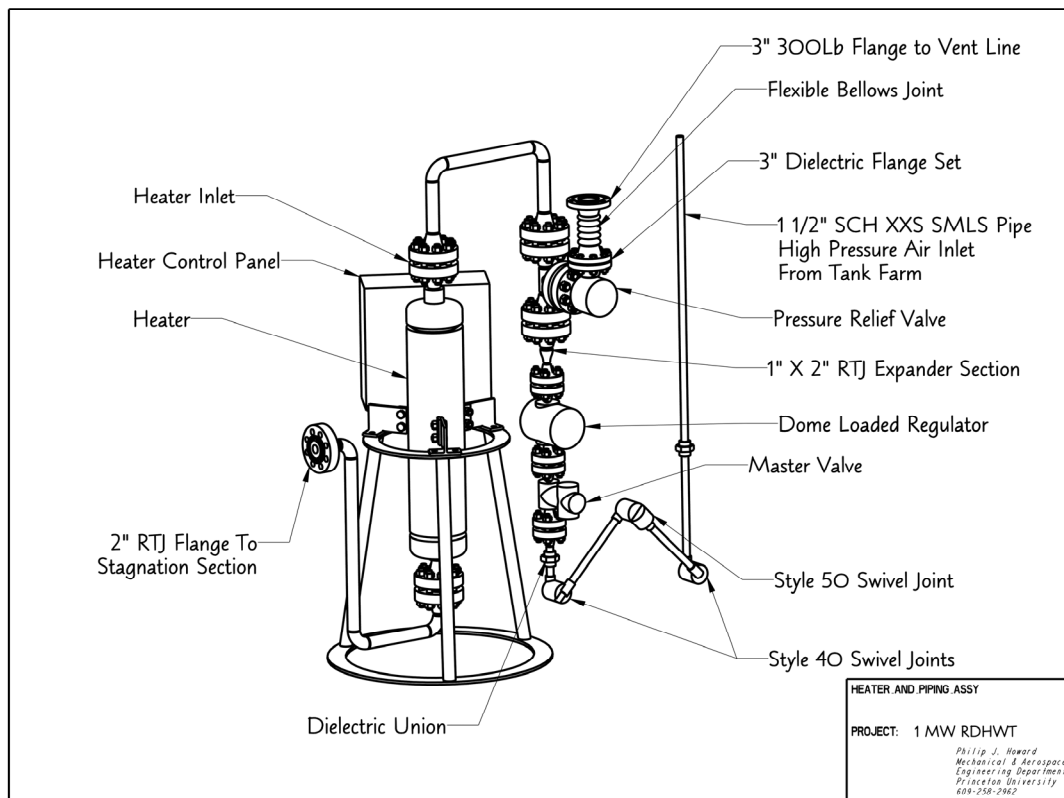


Figure 3-A1: The heater and piping assembly drawing.

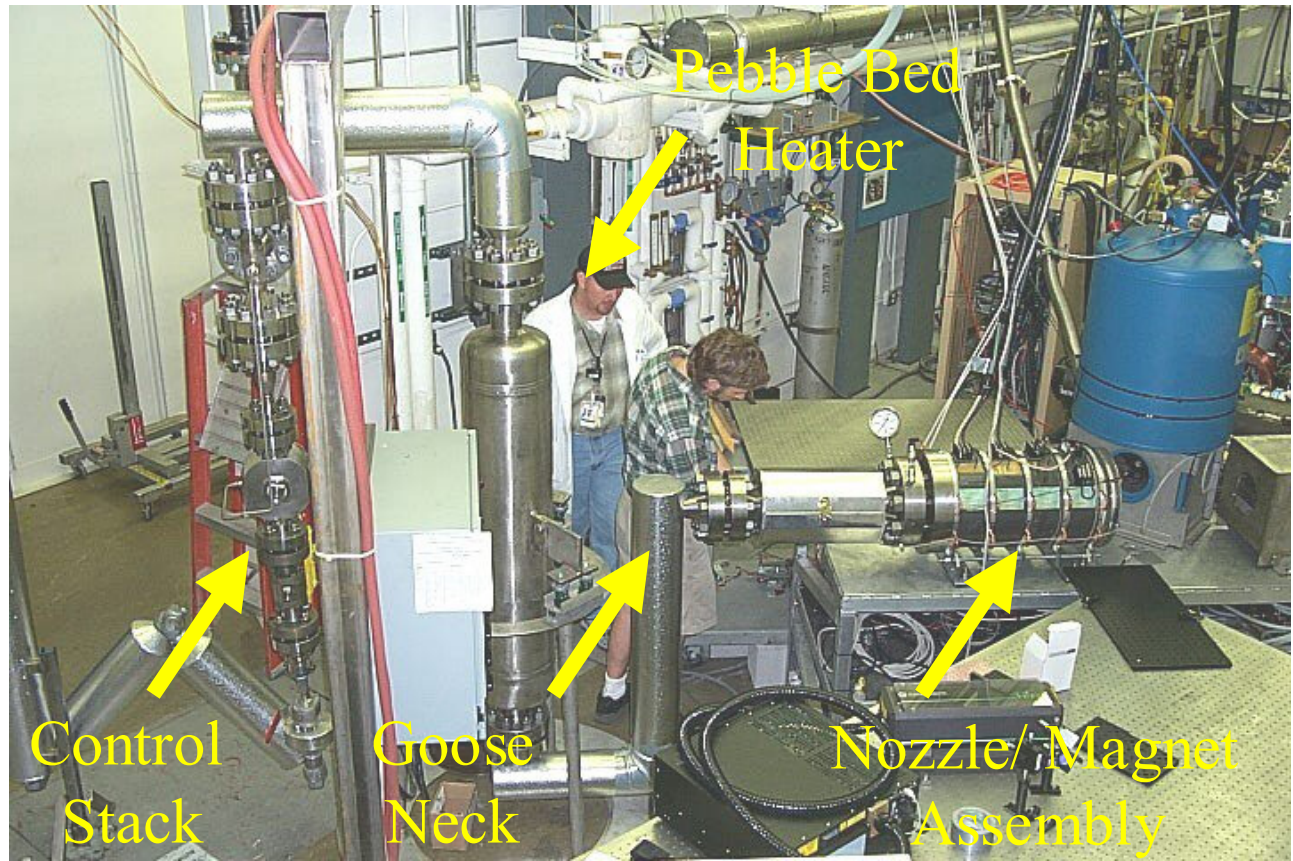


Figure 4-A1: Elements of the as-built high-pressure air delivery system.

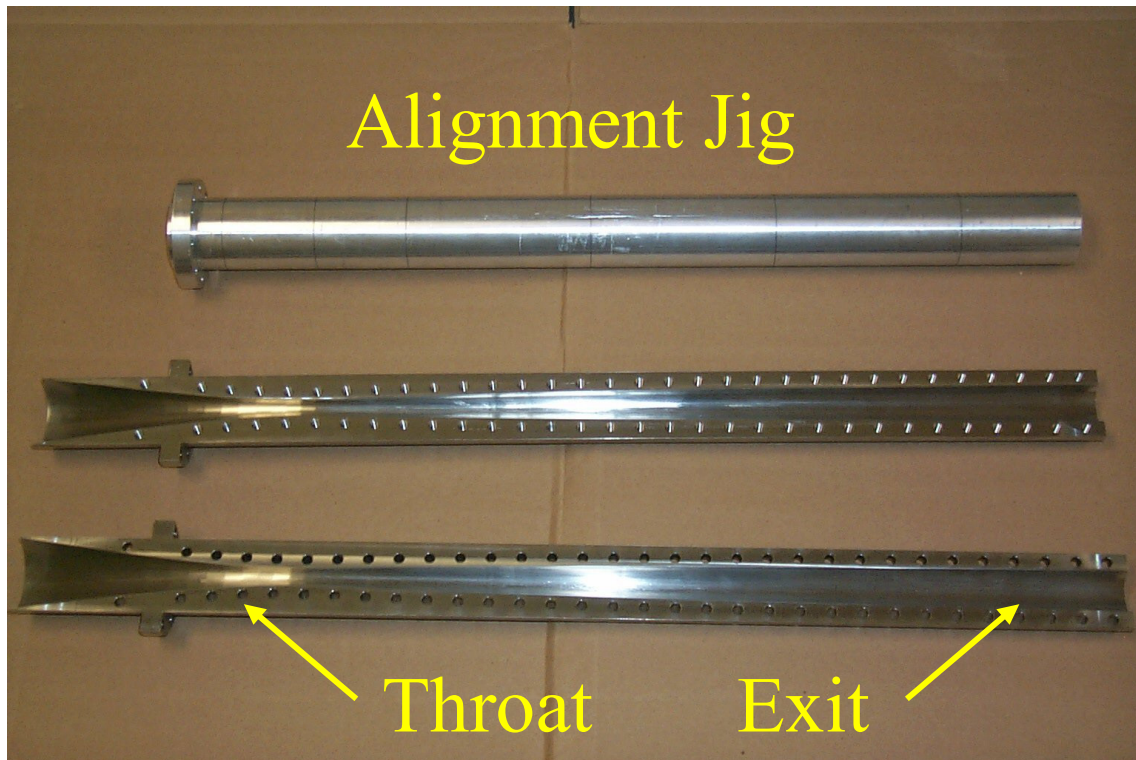


Figure 5-A1: The two halves of the nozzle are shown together with an alignment jig used during the construction of the magnet nozzle assembly.

APPENDIX A2: Details of the Nozzle Design Procedure

1MW Ideal Thermodynamic Path (Thermodynamic Considerations)

The ideal path for the 1MW experiment, compared with the MSHWT case, is shown in Figure 1-A2. Taking into account the available pressure and temperature sources, the upstream stagnation pressure and temperature were chosen to be 2650psi (~17.9MPa) and 650K, respectively. For the ideal path chosen, the flow is expanded isentropically to Mach 1.5 and then heat is added at constant Mach number. Heat is added until the desired total enthalpy ratio is achieved. Finally, the flow is expanded isentropically to flight conditions in the atmosphere. The stagnation and the test section conditions are summarized in Table 1-A2 and the flow thermodynamic properties at different downstream locations are shown in Table 2-A2. This design resulted in a total enthalpy ratio of 2.76 and a nozzle throat diameter of 5.73 mm, compared with 2.79 and 5.65 mm for the MSHWT case.

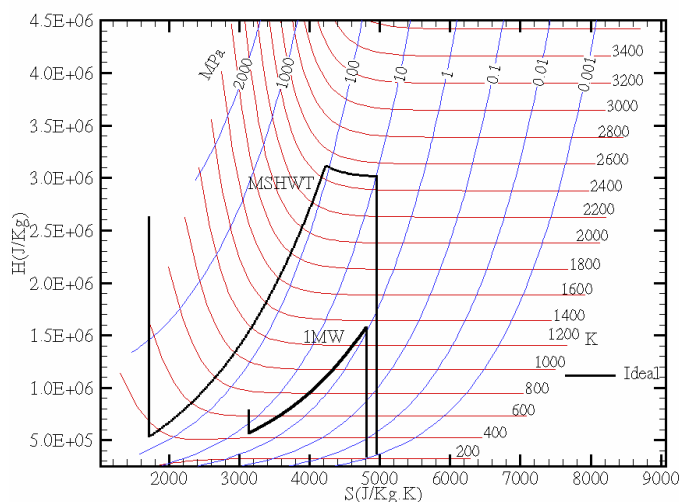


Figure 1-A2: Thermodynamics ideal path

Table 1-A2: Ideal Core Design

Stagnation Condition			Test Section					
Po (Mpa)	To (K)	Ho (MJ/Kg)	Mach #	m' (kg/sec)	Altitude (Km)	Dynamic Pressure (psf)	Hof (MJ/Kg)	Diameter (m)
17.9	650	0.79	6.3	0.72	28.9	800	2.17	0.15

Table 2-A2: Ideal Core Flow Thermodynamic Properties

	Diameter (mm)	T (K)	P (MPa)	ρ ((kg/m ³)/
Throat	5.7	541.6	9.3	57.5
Start Heating	6.2	450.6	4.8	36.8
End Heating	18.1	1351.5	1.0	2.6

Nozzle Design (One-Dimensional Nozzle Optimization)

To develop the nozzle shape, an analytic formula for the energy deposition was used. This analytic formula was developed at Sandia by R. Lipinski fitting results obtained with the Monte Carlo, ITS code for a range of one-dimensional cases in which beam energy was deposited into uniform air. Although there is no particular physical basis for the formula employed (except possibly the Gaussian form), it nonetheless fit the ITS calculated data to better than 10% for beams in the 1MV to 5MV range. This empirically derived analytic formula was then used in conjunction with a quasi one-dimensional Euler flow solver. With this approach, an objective function and a simplex method was developed in order to find the optimized nozzle shape such that the thermodynamic path closely followed the ideal path. The results of the one-dimensional nozzle optimization for a 0.8MV e-beam are shown in Figure 2-A2 where the actual thermodynamic path that can be achieved is compared with the ideal path.

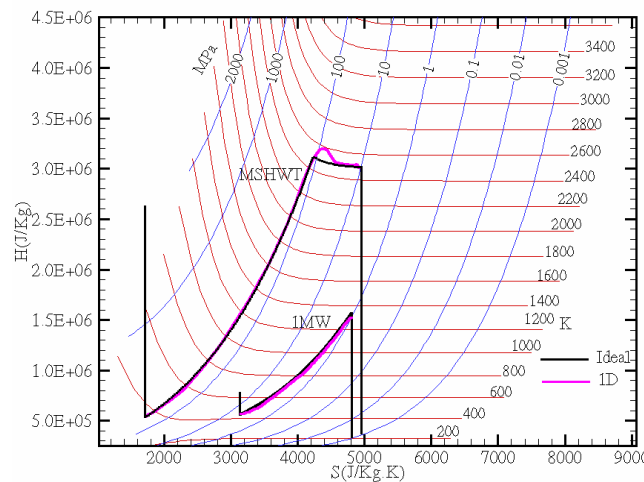


Figure 2-A2: One-dimensional modeled path compared to the thermodynamics ideal path

The optimal nozzle shape determined for the heat addition region is shown in Figure 3-A2. Of course this one-dimensional calculation was only one step towards a much more accurate Monte Carlo simulation of the energy deposition and a fully coupled two-dimensional fluid mechanics calculation in which the e-beam was kept away from the wall. To keep the beam away from the wall required a modification to the one-dimensional, optimized, nozzle shape.

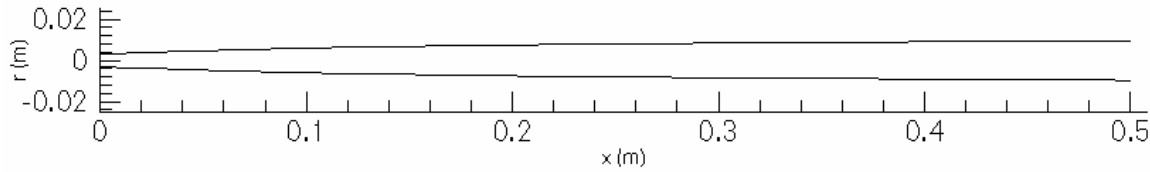


Figure 3-A2: The optimal nozzle shape (heat addition region)

Modified Nozzle

Since it was desirable to keep the e-beam energy away from the nozzle wall, an outer annular flow region was added to the ideal one-dimensional nozzle core flow. In this ideal case the outer flow was not to be heated. The corresponding outer annular area distribution was calculated by assuming that the outer flow was isentropic and had a pressure at each downstream location that was the same as it was for the heated core flow determined by the one-dimensional solution.

The optimized one-dimensional throat diameter was approximately 5.7 mm; this was increased to 11.4 mm to provide for the outer annular flow and to reduce the heat losses to the wall. This resulted, of course, in a mass flux (2.89 kg/sec) that was four times larger than the ideal one-dimensional mass flux. The modified nozzle shape is shown in Figure 4-A2 while the modified nozzle geometry is summarized in Table 3-A2.

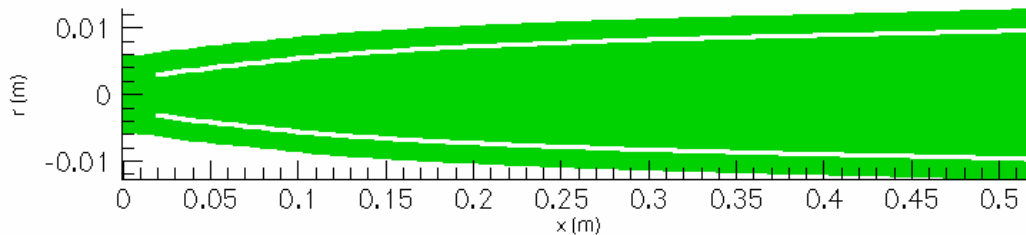


Figure 4-A2: The modified nozzle shape (x-axis and y-axis have different scales)

Table 3-A2: Modified nozzle geometry

	Diameter (mm)
Throat	11.4
Start Heating	12.4
End Heating	25.6

With this overall approach to the development of the nozzle shape in the heat-addition region it was then possible to use a full two-dimensional Euler simulation, coupled with the detailed Monte Carlo simulation for the energy addition, to determine how closely this idealized

approach could achieve the desired test-section conditions and whether a shock-free flow could be obtained.

Predicted Flow Field in the Nozzle

Inviscid Axisymmetric Simulation

In the inviscid case the axisymmetric Euler equations were discretized using a second-order, cell-centered, finite-volume scheme in space and a four-point Runge-Kutta scheme in time. The Jameson-Schmidt-Turkel scheme was used so that any shock formation was captured. The steady-state heat addition to every cell was determined by an iterative approach in which the density calculated from the axisymmetric Euler flow solver was provided as an input to the ITS, Monte Carlo, e-beam simulation code and the resultant energy lost from the e-beam in each cell was then transferred to the Euler code as the local heat addition for a given cell. When this iterative approach was adopted, a converged solution was obtained in 3 iterations.

The uniformity of the heating profile was improved, as compared with an earlier generation of predictions, by allowing for both an increase in the field strength at the HAWK cathode and by assuming a larger diameter, annular cathode. In order to avoid magnetic reflection, a design was adopted in which the HAWK cathode was immersed in a solenoidal magnetic field with field lines extending from the cathode to the nozzle. This design resulted in a beam that was uniform for approximately 30% of the nozzle diameter. The final design of the nozzle contour permitted approximately 12% of the heat energy to be lost to the nozzle wall. The magnetic field and the heating profile that were calculated using the TRICOMP and CYLTRAN codes are shown in Figures 5-A2 to 7-A2.

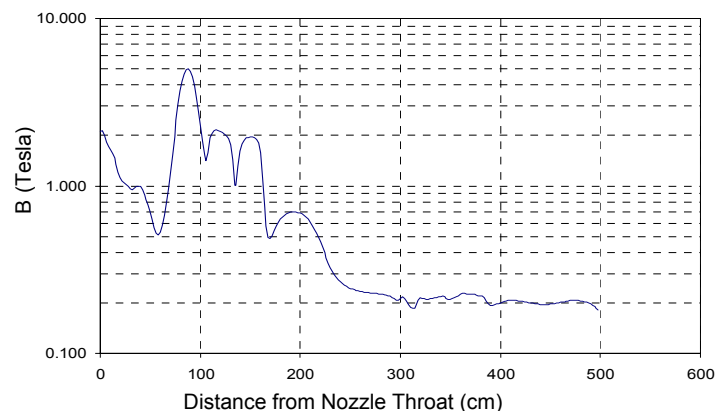


Figure 5-A2: Magnetic field from the nozzle throat to the cathode

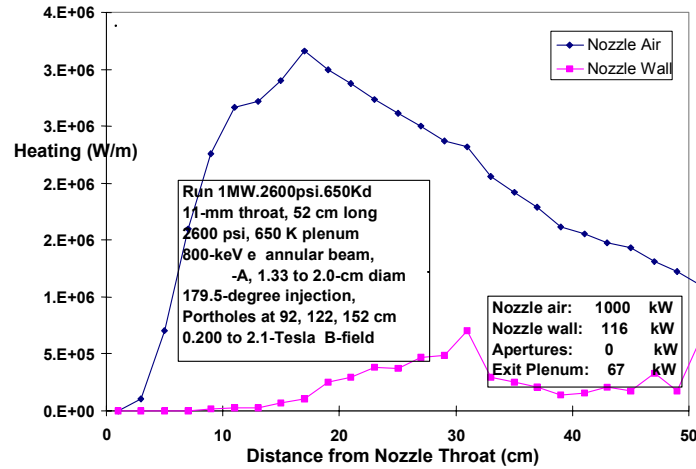


Figure 6-A2: Power deposition profiles as determined by CYLTRAN with TRICOMP

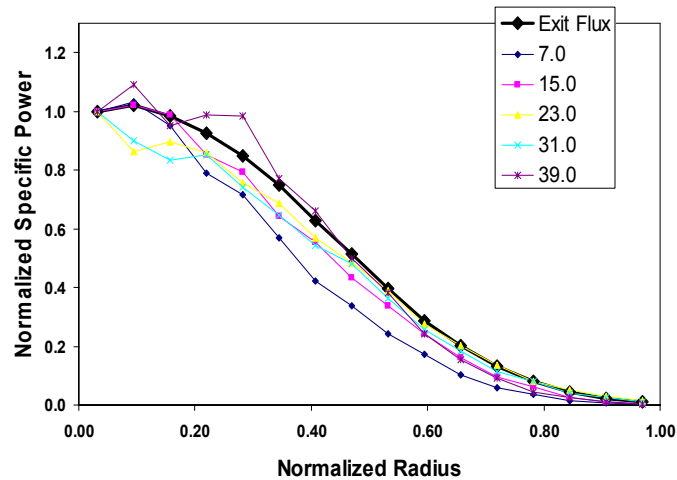


Figure 7-A2: Normalized power density (per unit volume) at various axial locations in the nozzle

With the approach and models described above, the results described below were obtained for the fully coupled, inviscid simulation of the 1MW experiment. In Figure 8-A2, the contours of total enthalpy show that the e-beam provided nearly uniform heating to 30% of the diameter of the nozzle flow while the outer annular flow near the wall was relatively unheated. Figures 9-A2 and 10-A2 show the predicted temperature and Mach number contours, respectively.

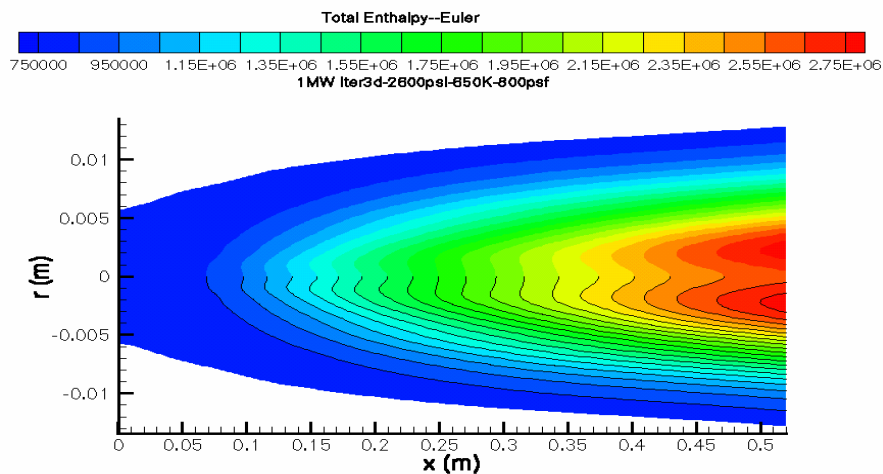


Figure 8-A2: Total enthalpy profile

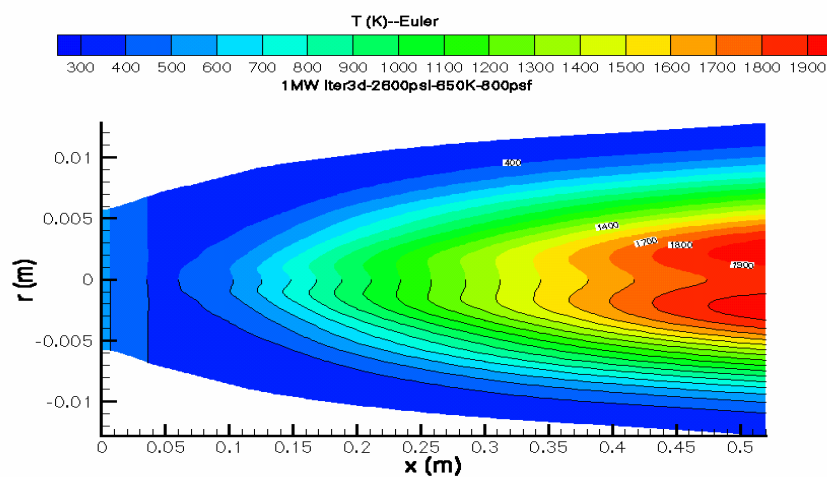


Figure 9-A2: Temperature profile

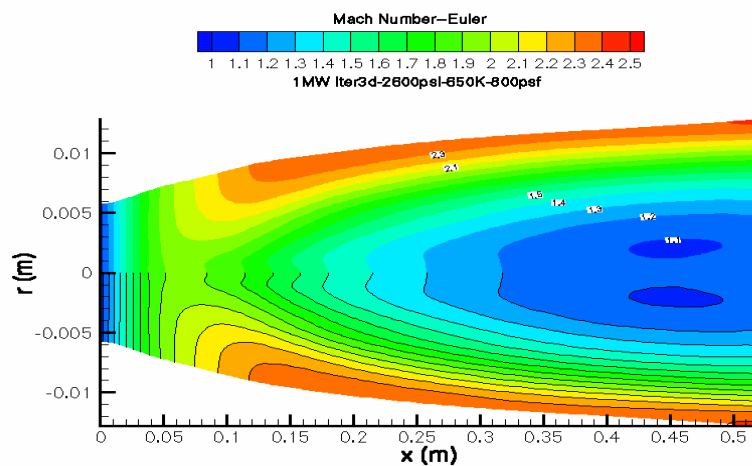


Figure 10-A2: Mach number profile

Viscous Axisymmetric Simulation

Further calculations were completed using the two-dimensional Reynolds-averaged Navier-Stokes equations and the Baldwin-Lomax turbulence model in order to include boundary layer effects. The nozzle area distribution was again increased in an iterative fashion to include the boundary layer displacement thickness. The spacing of the numerical mesh near the wall was constructed in order to capture the laminar sublayer that leads to a near-wall spacing of the order of y^+ . As shown in Figures 11-A2 and 12-A2, no major changes occur to the heated core flow region.

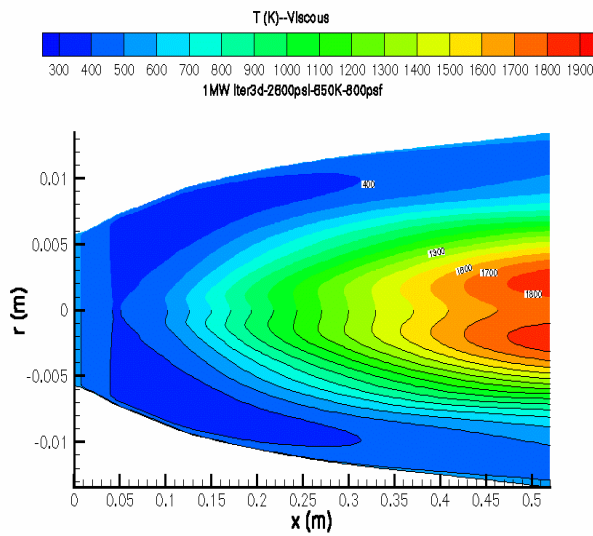


Figure 11-A2: Temperature profile

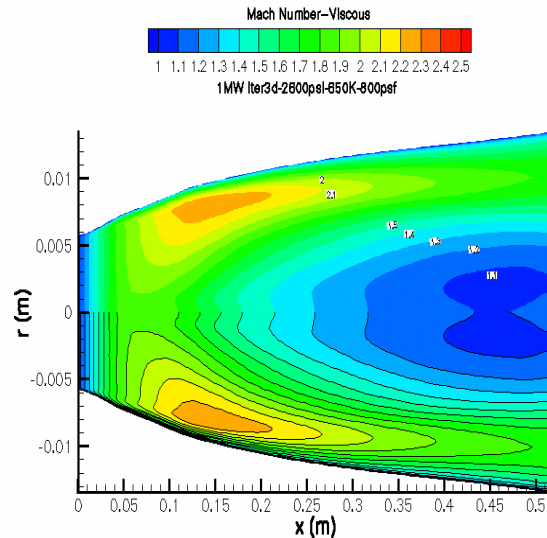


Figure 12-A2: Mach number profile

Figure 13-A2 shows the corresponding thermodynamic path along the centerline. The overall design strategy produced a thermodynamic path in the core flow that closely approximates the proposed ideal thermodynamic path. The temperature at the centerline, however, increased to approximately 1800K and the Mach number dropped to 1.2, as shown in Figure 12-A2, because the assumed heating profile was not a uniform "top-hat" profile.

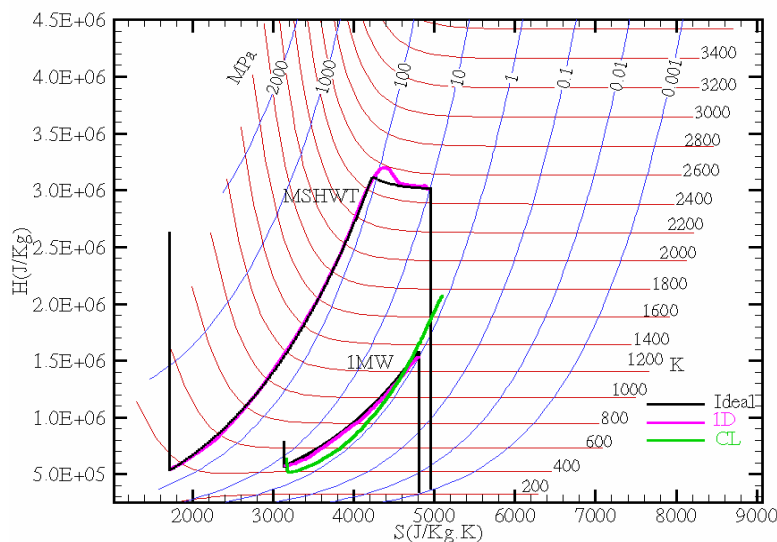
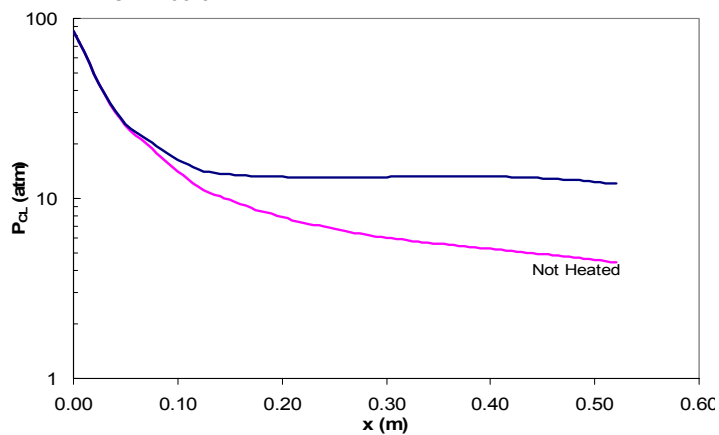


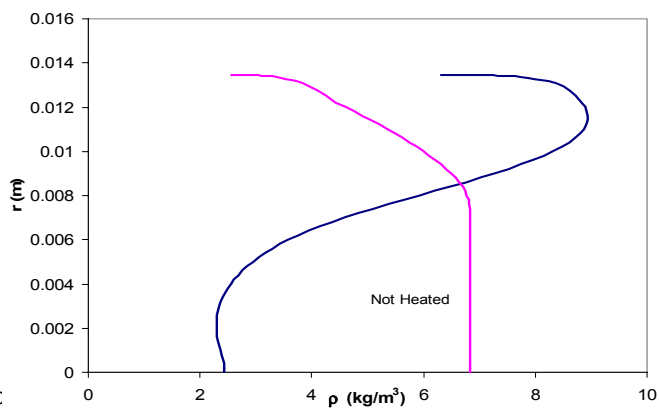
Figure 13-A2: Centerline thermodynamics path compared with both the one-dimensional and the ideal paths.

Predicted Pressure Distribution and Exit Flow Profiles

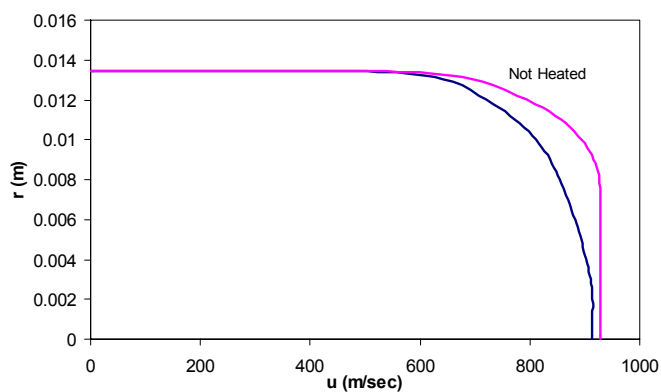
Figure 14-A2 shows the predicted pressure distribution and exit flow profiles with and without heat addition. These results have been obtained from the fully coupled e-beam and 2D viscous flow solver. A smooth adiabatic wall has been assumed for the turbulent boundary layer that develops.



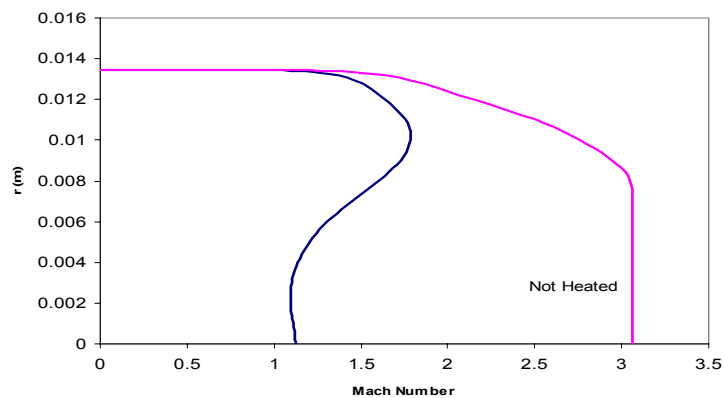
(a)



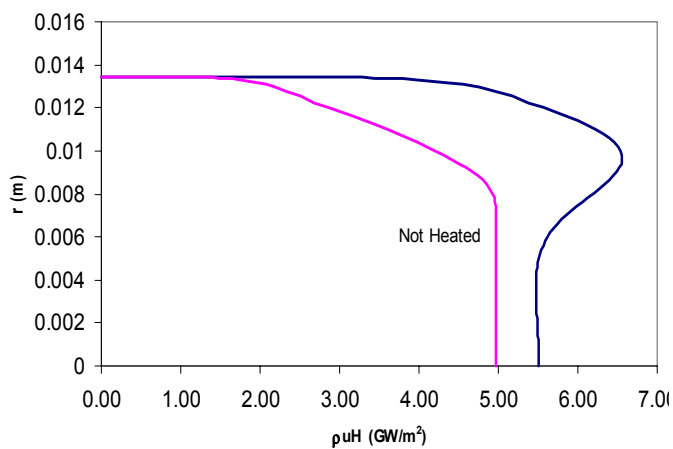
(b)



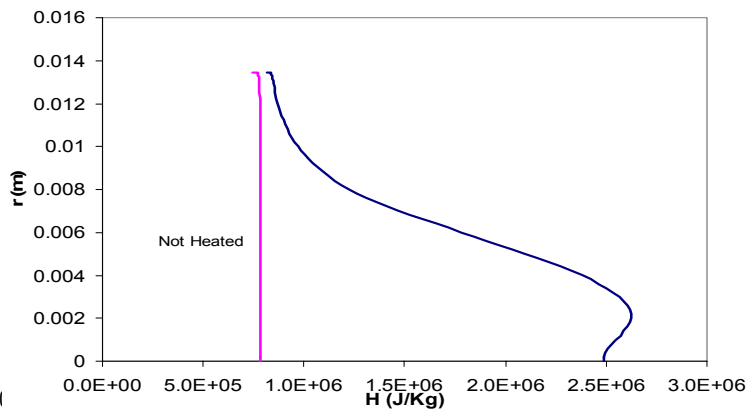
(c)



(d)



(e)



(f)

Figure 14-A2: Nozzle exit profiles with and without energy addition, a) centerline pressure distribution, b) density profile, c) velocity profile, d) Mach number profile, e) energy flux profile, and f) total enthalpy profile.

APPENDIX A3: Details of the Computer Control System

Synchronization of All Hardware

The synchronization of all hardware (lasers, cameras, magnets, HAWK ...etc) was accomplished with the use of a precise 10 Hz master clock supplied by a single Stanford model DG535 digital pulse / delay generator (DD/PG) operating in internal mode. The master clock was used to drive Labmaster while simultaneously synchronizing two other identical pulse generators each operating in external mode. Labmaster, in turn, was used to modulate (inhibit or disinhibit) the output of one of these DD/PGs as will be described below. In this way two types of timing pulses were generated: those that were generated and propagated continuously at 10 Hz and those that were generated continuously at 10 Hz but propagated only once because they were normally inhibited by Labmaster. The continuously propagated pulses were used, for example, to drive the diagnostic YAG lasers that had to be run continuously so as to avoid thermal shock while still remaining synchronous with all other experimental hardware. The one-time pulses were used to accomplish tasks such as triggering magnets, arming cameras, starting the collection of fast data and anything else that had to be accomplished only once just prior to the firing of HAWK. The system used to control the hardware during the 1 MW experiments is shown schematically in Fig 1-A3 below.

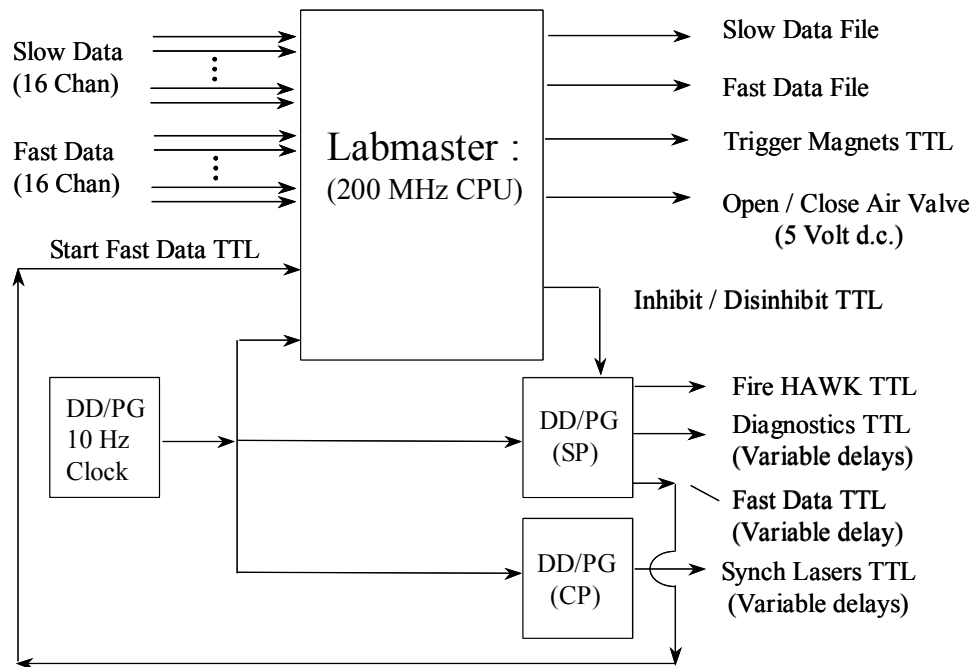


Figure 1-A3: A schematic representation of the computer system used during the 1 MW experiments. A 10 Hz master clock from a DD/PG drove all timing. Data was collected and analyzed in real time by the Labmaster code upon receipt of each clock pulse. The program, in turn, modulated the outcome of the single period (SP) DD/PG by either inhibiting or disinhibiting the propagation of TTL pulses. An uninterrupted stream of TTL pulses were sent to the appropriate laboratory equipment at 10 Hz by the continuous propagation (CP) DD/PG. The actions of the two DD/PGs used during the experiments are summarized below in Figs 2-A3 and 3-A3.

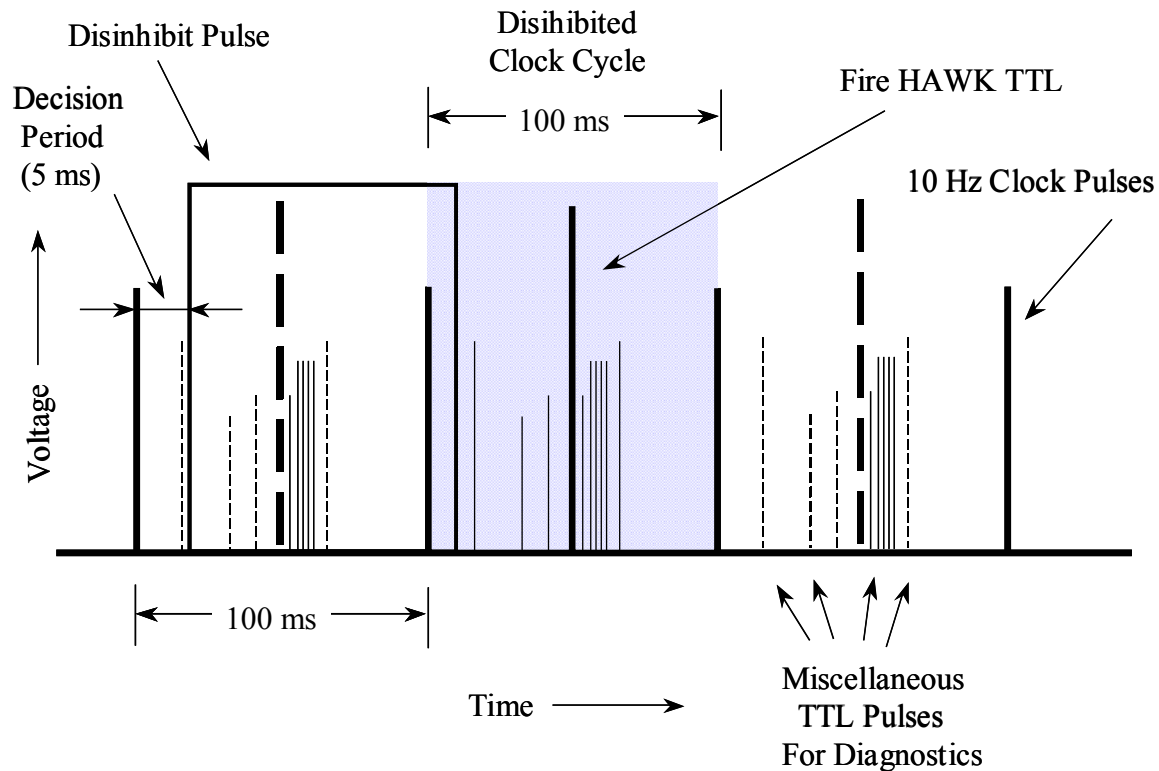


Figure 2-A3: Various TTL pulses from the two output DD/PGS are shown over three clock cycles. The dashed lines indicate that the associated TTL pulses were generated but not propagated. When real-time blowdown conditions were determined by Labmaster to be acceptable, a disinhibit pulse was generated and sent to the SP DD/PG. During the next clock pulse (and only during the next clock pulse) the generated TTL pulses were propagated to the appropriate equipment. Employing a 200 MHz CPU, the time required for Labmaster to make all required decisions was, as is indicated above, about 5 ms.

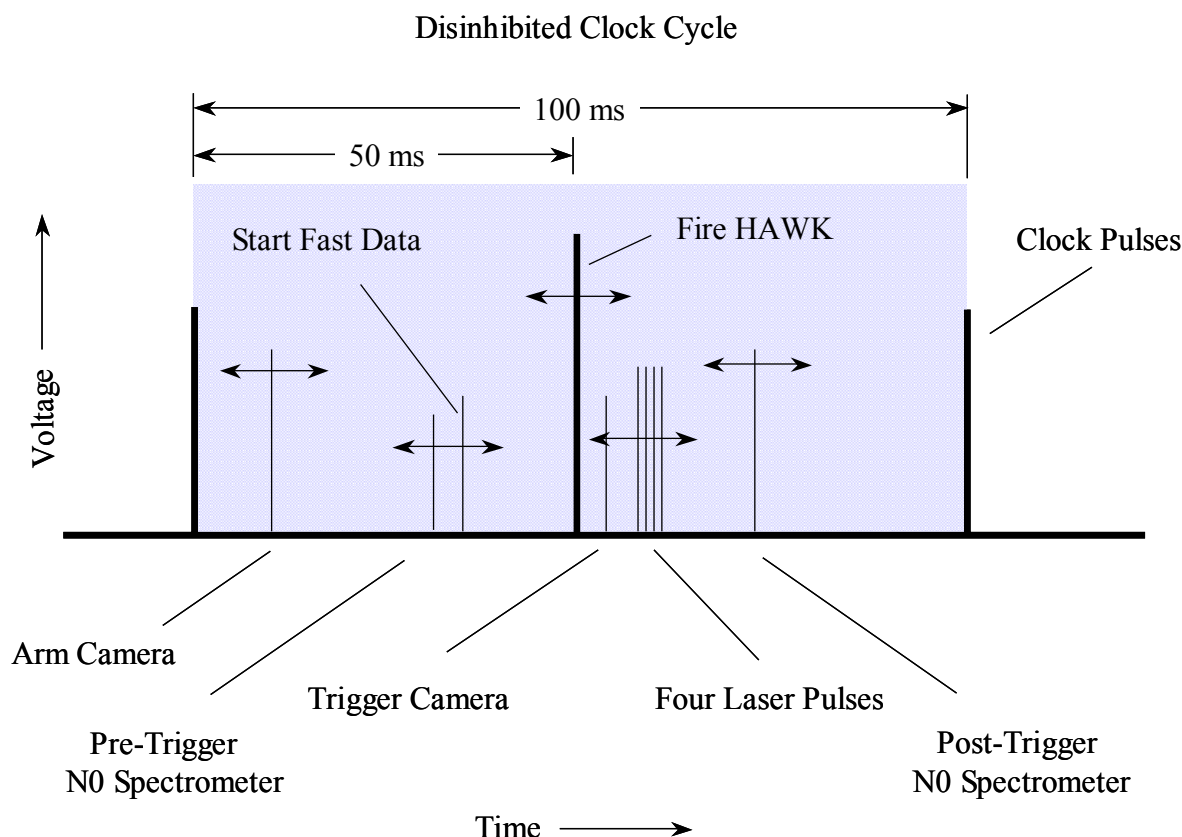


Figure 3-A3: Shown are examples of some TTL pulses propagated during the disinhibited clock cycle that is also shown in Fig 2-A3. All pulses are represented as solid rather than dashed lines because all pulses were propagated during this clock cycle. The arrows are meant to indicate that the timing of all pulses with respect to the clock pulses could be adjusted simply by changing the settings of the appropriate DD/PG.

Collection and Processing of the Slow Data

Two types of data were generated during the 1MW experiments and processed by Labmaster; these were designated the slow and fast data. The slow data was collected synchronously with the master clock at 10 Hz. An example of slow data is given in Fig 4-A3 below. Slow data collection began upon initiation of the Labmaster program. This data was used to characterize air pressures, temperatures, magnetic field levels and other phenomena that occurred over the few seconds associated with a standard blowdown. Slow data was collected and processed in real time so as to make decisions about what actions to take during a blowdown (i.e. whether or not to open valves, trigger magnets or fire HAWK). This data was collected for a total of 40 seconds (400 clock pulses) so as to allow most parameters to return to their baseline values after a blowdown. After termination of a blowdown, the slow data was automatically written into data files.

The actions of the Labmaster program were completely determined by the TTL pulses supplied externally by the DD/PG 10 Hz master clock. Each individual clock pulse triggered a scan of up to 16 slow data terminals connected to the computer CPU by a data acquisition board. In the 100 msec between each clock pulse, a 200 MHz CPU mathematically converted the collected voltages into physically meaningful quantities such as temperatures and pressure values. These parameters were then compared to threshold (or inhibit) values stored in the Labmaster software. If certain threshold levels were attained then appropriate TTL signals were generated during the next clock cycle and various actions were taken (or inhibited) in the laboratory.

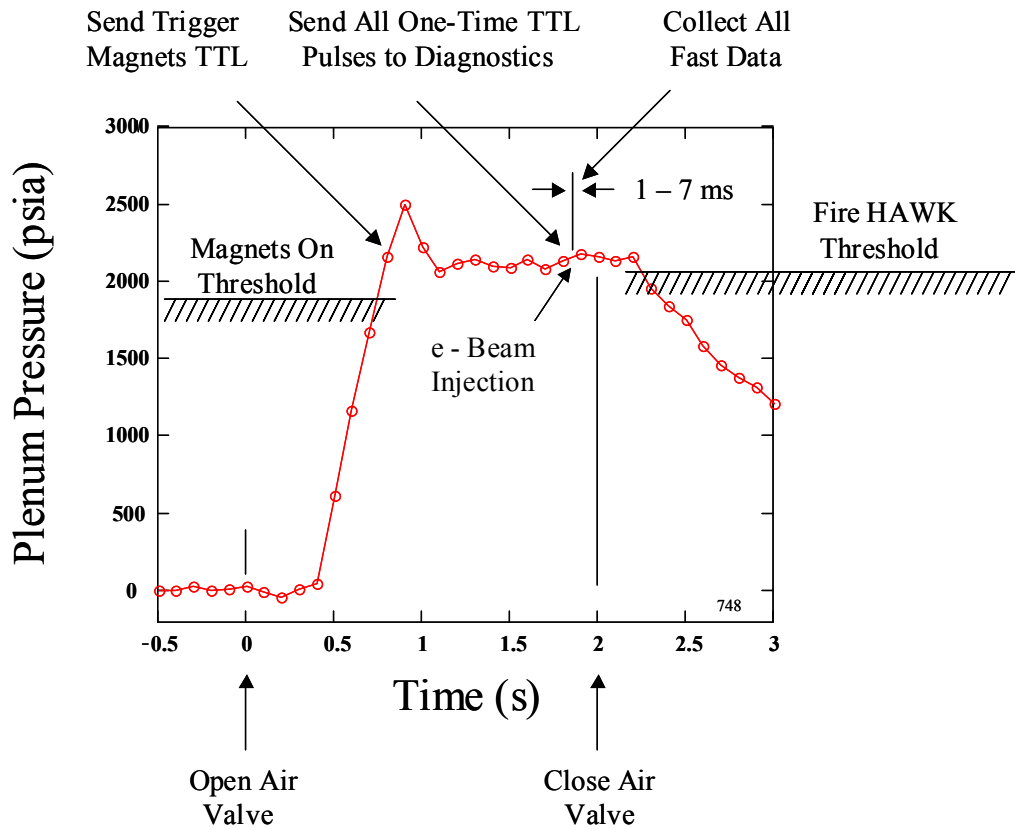


Figure 4-A3: Shown in this figure is an example of slow (10 Hz) data. The measured plenum pressure is shown as a function of time. Also indicated is the entire duration of e-beam injection that was captured using fast (75 kHz) data collection during a 15 ms data collection window. Several actions taken by Labmaster during the course of this blowdown are also indicated. Some of the threshold levels used by Labmaster to make decisions in real time are also shown

Triggering and Collection of the Fast Data

Fast data was taken at a much higher rate (75 kHz) and collected over a much shorter period (15 ms) as compared to slow data. The data were strobed into memory using a high frequency clock internal to the LabView data acquisition board. The collection of fast data was triggered externally by the arrival of a TTL pulse from the one-time pulse generator that was used to fire HAWK (see Figs 3-A3 and 4-A3). The fast data collection window thus could be carefully centered over the 1 – 7 ms HAWK injection duration in order to measure the change in parameters caused by e-beam injection. The data collected in the fast mode included the increase in nozzle pressure, and the nozzle current to ground. The fast data was not used in real time but rather was stored into data files separate from the slow data.

Control of the Air Delivery System

The most fundamental task undertaken by Labmaster was to control the high-pressure air delivery system so as to initiate and terminate blowdowns. In this regard, the program received real-time signals from a pressure-to-voltage transducer and a thermocouple that were each positioned in the plenum. When Labmaster was initiated, data was taken for 10 seconds to establish baseline levels. The program next started the blowdown by sending a 5-volt d.c. signal (Open / Close Air Valve, Fig 4-A3) to the solenoid switches controlling the high-pressure valve. Later in the blowdown after the decision was made to fire (or inhibit) HAWK, Labmaster waited one more 100 ms clock cycle before allowing the 5 volt d.c. signal to return to ground hence closing the valve and ending the blowdown.

Triggering the Magnets

Several sets of magnets had to be energized in order to have a successful blowdown. In particular, solenoids both internal and external to the HAWK pressure vessel as well as several nozzle solenoids had to be fired in a predetermined sequence. The firing sequence of the magnets was set in advance of the blowdown by a bank of DD/PGS under the control of the HAWK operator. The function of Labmaster was to provide the initial TTL pulse to start the magnet firing sequence. After the firing sequence was initiated, a delay of approximately one second was needed before HAWK could be fired. This delay allowed the nozzle magnetic field to reach a steady state. The one-second delay, moreover, was close to the maximum allowable current pulse duration so as to avoid thermal damage to the magnetic solenoids – 1.4 seconds. Triggering the magnets, therefore, had to be accomplished in a manner that was carefully timed with respect to the airflow.

The timing of the magnet trigger pulse was complicated, however, by the fact that the mechanical response of the high-pressure valve to the opening of the switches was not always immediate. In fact, delays ranging between 0.3 and 2.0 seconds were observed before the nominally opened valve actually allowed air to flow into the plenum. In order to compensate in

real-time for this large and unpredictable delay, Labmaster was programmed to delay the firing of all magnets (the first step in the blowdown / e-beam injection process) until the measured plenum pressure attained a threshold value (typically 1700 psia, see Fig 4-A3). During the next clock cycle after the threshold pressure was attained, Labmaster sent a TTL pulse to the HAWK control console that initiated the magnet firing sequence.

Protecting the Nozzle and Firing HAWK

Another critical task accomplished by Labmaster was to issue the fire HAWK TTL signal to the HAWK control console. Melting of the stainless wall would have taken place immediately if the HAWK e-beam had been injected into the nozzle without the protection of dense blowdown air as well as the presence of a sculptured magnet field.

In this regard, Labmaster had to process the slow data in real-time to see if several conditions had been met before HAWK could be fired.

In particular, when the Trigger Magnets TTL was issued and after the 1 sec delay discussed above, HAWK was eligible to fire. However, before HAWK could actually be fired, several conditions had to be confirmed during the clock period just prior to the FIRE HAWK TTL pulse being issued. In particular, *both* the measured plenum pressure and temperature had to be verified as being above threshold values. In addition, *both* the magnetic fields immediately external to the HAWK pressure vessel and at the nozzle had to be *verified* as being “on”. Placing magnetic reed switches in proximity to the solenoids in question and then wiring the switches in series accomplished this latter task. The switches provided Labmaster with a magnetic field status signal. Only when these conditions were verified could a disinhibit signal be generated by Labmaster and sent to the one-time DD/PG to allow not only the fire HAWK TTL to be issued, but also all associated one-time TTL pulses need for diagnostic purposes (see Figs 3-A3 and 4-A3).

APPENDIX A4: Details of the Electron Beam and Accelerator

The Radiatively Driven Hypersonic Wind Tunnel concept involves several broad areas, including an ultra-high pressure source, high-temperature nozzle, energy addition beam and accelerator, energy-addition physics and modeling, diagnostics, controls, and system integration. This appendix describes the electron beam and hardware involved in the 1 MW, 5-ms experiment.

4.1 Energy-Addition Objectives

The previous energy addition experiment had achieved 100 kW of energy addition for a maximum of 3 ms. In that experiment, only about 25% of the beam power was deposited into the blow-down air and most e-beam injections lasted only 1 ms which allowed the resulting airflow to only barely approach a steady state. The e-beam employed, moreover, was so tightly spiked on centerline that good data were difficult to obtain. Further, the beam was bent only 11 degrees going into the nozzle, which is much too small an angle for the final MSHWT facility. Accordingly, the energy-addition goals for the 1 MW experiment were:

- Demonstrate a substantial increase in predictable power deposition by delivering 1 MW into flowing supersonic air with an electron beam
- Demonstrate high-efficiency beam extraction into a magnetic field with a cathode immersed in the magnetic field
- Demonstrate stability of the energy deposition process at high power levels for 5 ms
- Demonstrate extraction of the beam through a differential-pumping window
- Demonstrate more uniform power deposition on centerline
- Demonstrate strong beam bending sufficient to avoid the intense air stream of this experiment and scalable to the MSHWT requirements.

To meet these objectives numerous upgrades and modifications to the beam delivery hardware were needed. The following sections describe these changes. They are in order of presentation:

4.2 Upgrade from 100 kW to 1 MW and from 25 to 85-percent efficiency

4.2.1 Magnetic transport first-principle analysis

4.2.2 Magnetic transport code simulations

4.2.3 Magnet system

4.2.4 High-Voltage deck electronics

4.3 Upgrade to 5 ms duration

- 4.3.1 Large capacitor bank upgrade
- 4.3.2 Cathode capacitor upgrade
- 4.3.3 Differential pumping system
- 4.3.4 5-Tesla superconducting magnet
- 4.4 Better beam uniformity: Annular cathode
- 4.5 Bending Angle of 45°
- 4.6 Beam alignment into nozzle
- 4.7 Beam states during blowdown and data acquisition
- 4.8 Beam Conditions for the Primary Data Set (March 2003)
- 4.9 Summary

Figure 4.1.1-A4 shows the configuration of the HAWK laboratory. In this figure the HAWK electron beam accelerator is the large blue horizontal cylindrical tank at the upper right. The beam exited from the accelerator through a 5-Tesla superconducting magnet seen in the center of the photo under a blue liquid helium dewar. The emitted beam propagated around a 45° bend to enter the nozzle from the downstream end. The nozzle was located along the centerline of a bank of solenoid magnets. The air from the nozzle was directed into a steel box (far right) where a series of parallel plates removed heat from the air before it was directed up toward the ceiling.

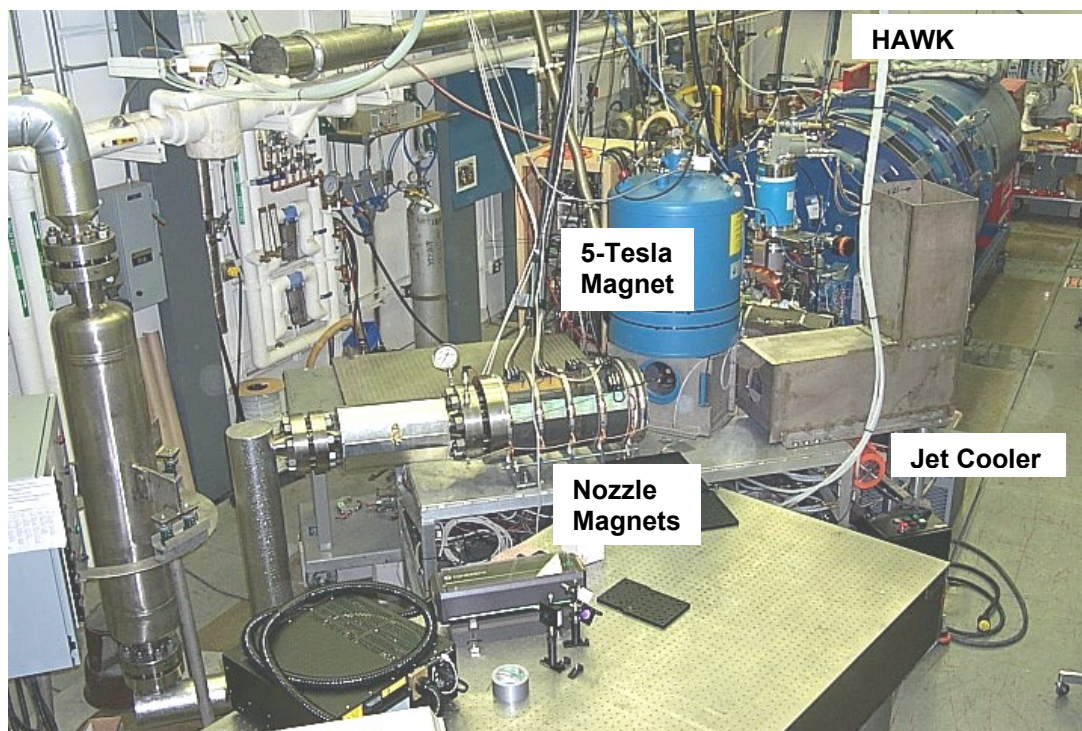


Figure 4.1.1-A4: Lab overview.

4.2 Upgrade from 100 kW to 1 MW and from 25 to 85-percent Efficiency

4.2.1 Magnetic Transport First-Principles Analysis

The primary difficulty in achieving high power during the previous 100 kW experiment was magnetic reflection of the electrons out of the nozzle as the magnetic field attempted to converge the beam toward the throat. As mentioned previously in this report, the electron beam was guided into the nozzle and forced to converge as it approached the throat by a strong axial magnetic field. The field lines converged toward the throat (because the magnets were designed to have a stronger field there) and the electrons spiraled around these lines. However, there was also an average repulsive force directed out of the nozzle that was caused by the $\mathbf{v} \times \mathbf{B}$ force stemming from the forward velocity of the electrons and the radial portion of the converging magnetic field lines. Hence there is a tendency for the electrons to reflect out of the converging field zone. This effect was important in the 100 kW experiment because the beam was created in a cathode that was free of magnetic fields and, therefore, the electrons had to pass over a continuum of strongly-increasing radial field components as they entered the nozzle. Indeed, it was only the scattering in the air that allowed a large fraction of beam electrons to penetrate the nozzle by fortuitous forward scattering.

This lack of penetration during the 100 kW experiments is demonstrated in Fig 4.2.1-A4. This figure shows the measured beam current as a function of the distance from the nozzle throat in the 100 kW experiment in 0.82-atm air. The beam duration was about 50 microseconds long, so the effect on air density from heating was small. There was no blowdown for these measurements, and no nozzle either, so there were no losses to a nozzle wall. As can be seen, less than 40% of the beam passes the 50-cm location where the nozzle exit would have been, and only 15% reaches 10 cm from where the throat would have been. With thick blowdown air, the total beam absorption was only around 25%. Also shown are the Integrated Tiger Series code (to be described later) predictions. As can be seen in the figure, the agreement between the predictions and the measurements was reasonable.

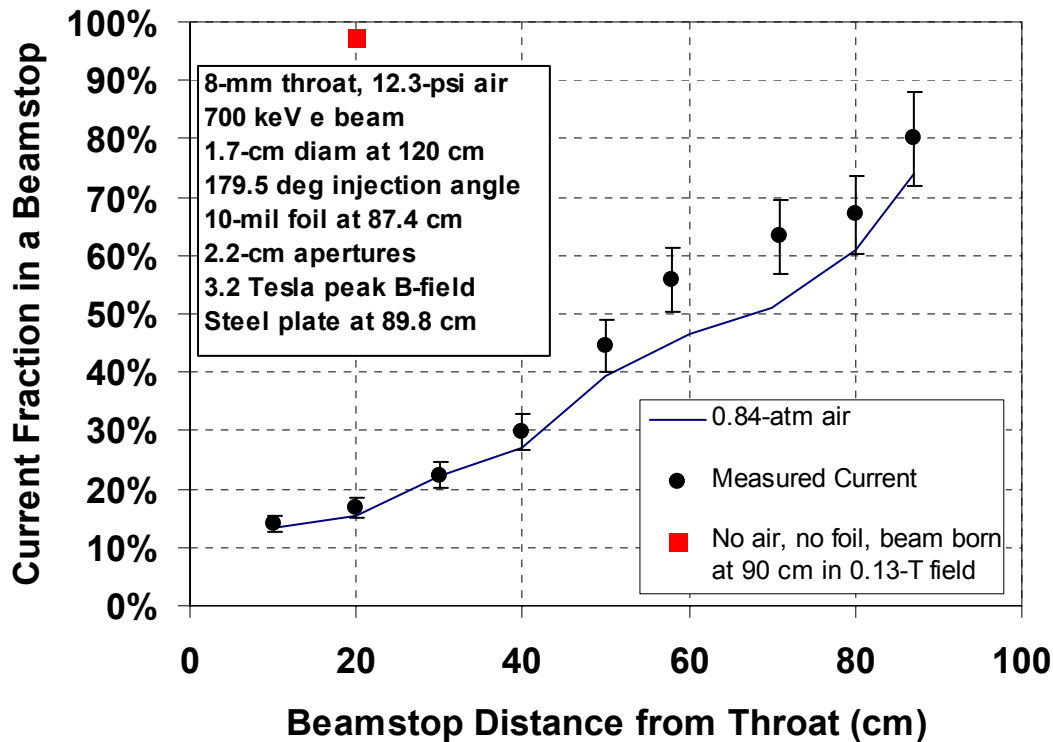


Figure 4.2.1-A4: Beam current collected in a beam stop vs. distance from throat in 0.8-atm air for the previous (100-kW) experiment.

In order to increase the fraction of beam power penetrating the converging field, the cathode had to be embedded in a solenoid magnetic field that extended to the nozzle throat so the beam did not cross as much radial magnetic field thus acquiring angular momentum as it entered stronger fields. Such a case was modeled assuming an absence of air to see the effect for this geometry, and the result was 97% current transport (see the square in Figure 4.2.1-A4).

Hence it was determined that the keys to increasing beam transport efficiency was to have the e-beam born in a strong magnetic field and to have it follow a continuous field all the way to the throat. As will be discussed below, these tactics are also important to achieving good beam quality and air-heating uniformity within the nozzle, as well as to limiting the amount of nozzle wall heating.

The desired radial beam current profile has sometimes been called a “top hat” profile. A top hat energy deposition profile is one that looks like a top hat when intensity is plotted on the vertical axis and position is plotted on the two horizontal axes (x and y, or r and θ). A Gaussian profile is one that looks like a “bell curve”. Figure 4.2.2-A4 shows the two profiles.

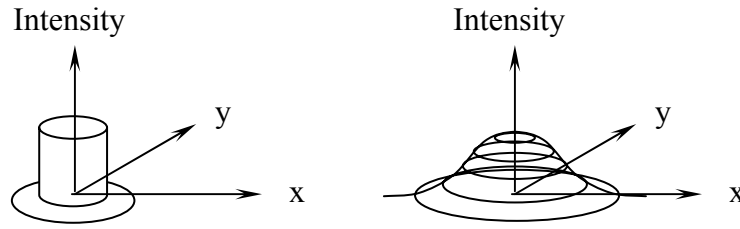


Figure 4.2.2-A4: Top hat and Gaussian energy deposition profiles.

It should be noted that Energy deposition is linearly proportional to beam intensity. The equation for a top hat distribution is:

$$I = I_0 \text{ for } r < r_b \quad (1)$$

$$I = 0 \text{ for } r > r_b \quad (2)$$

Where I is the energy deposition density (W/m^3), I_0 is the deposition on the centerline, r is the radial distance from the axis, and r_b is the beam radius. The equation for a Gaussian distribution is:

$$I = I_0 \exp\left(-\left(\frac{r}{r_G}\right)^2\right) \quad (3)$$

Where r_G is the “Gaussian radius” of the beam and is the radial distance from the centerline where the beam intensity is $1/e$ (36.8%) of the centerline intensity. If one integrates the power density from the centerline out to infinity for a Gaussian distribution, the integral is simply:

$$P = \pi r_G^2 I_0. \quad (4)$$

This is the reason for using r_G instead of (say) the half width at half maximum.

If the electron beam starts out as a top hat (uniform) distribution, it will slowly degrade into a Gaussian distribution as it passes through air and scatters off air molecules. A strong axial magnetic field can reduce the spread of the beam in the radial direction and slow down the change in shape, but it cannot stop the degradation. The art of making a top hat energy deposition distribution profile in the nozzle air near the throat is in choosing a magnetic field configuration and accelerator configuration that reduces the amount of degradation to acceptable levels.

As noted previously, an electron beam gains canonical angular momentum as it penetrates into an increasing magnetic field. That is, the forward motion of the electrons begins to be transferred into transverse circular motion without loss of kinetic energy. Eventually, the electrons will be reflected back out of the field. To minimize this effect, the beam must be born within the magnetic field that is parallel to the intended path of the beam (usually along the axis of the accelerator). There is a precise interplay between the desired beam size and profile at the nozzle, the size of the cathode, and the strength of the magnetic field at the cathode.

As long as the beam is in a vacuum, the beam radius at any axial location is simply a function of the magnetic field at that location and at the cathode:

$$r_{bv} = \sqrt{\frac{B_c}{B}} r_c \quad (5)$$

Where B is the local magnetic field strength, B_c is the field strength at the cathode, and r_c is the radius of the cathode. If, as is usually the case, the cathode emits electrons uniformly, the beam still has approximately a top hat distribution at this location.

As the beam enters air, it scatters, and the amount of scatter can be estimated as some number times the local average Larmor radius of the electrons as they spiral around the field lines:

$$r_L = \frac{\gamma m_e v \beta_p}{e B} \quad (6)$$

Where γ is the relativistic mass factor, m_e is the mass of the electron, v is the electron velocity, β_p is the component of the electron velocity perpendicular to the magnetic field, e is the electron charge, and B is the magnetic field strength. Hence, to a simple approximation, the beam radius in air after scattering is:

$$r_b = r_{bv} + n r_L \quad (7)$$

With these considerations, one can estimate the fields needed to achieve a desired amount of beam uniformity in the nozzle. Let f_s be the fraction of the local nozzle radius that is the slope or shoulder of an approximate top hat distribution, and let f_f be the fraction that is essentially flat (before the shoulder begins). Then the field strength needed in the nozzle at any particular location is:

$$B_n = \frac{n \gamma m_e v \beta_p}{e f_s r_n} \quad (8)$$

Where n is approximately 1 (based on simulation experience). The field strength needed at the cathode is then:

$$B_c = \left(\frac{f_f r_n}{r_c} \right)^2 B_n \quad (9)$$

The field strength needed at the apertures of the differential pumping station that transitions from the accelerator vacuum to open air, (and which will be described later) must also be considered and may be obtained from equation (5):

$$B_{pp} = \left(\frac{r_c}{r_{pp}} \right)^2 B_c = \left(\frac{f_f r_n}{r_{pp}} \right)^2 B_n \quad (10)$$

Where B_{pp} is the magnetic field at the pumping port and r_{pp} is the radius of the port aperture.

The magnetic field also should be strong enough at the bend between the pumping port and the nozzle so that the beam electrons undergo at least several cyclotron oscillations (spirals) along the curve. This will keep the beam from expanding too much on the curve. Hence one can write:

$$B_{bend} = \frac{2 \pi \gamma m_e v n_{bend}}{e L_{bend}} \quad (11)$$

Where n_{bend} is about 5 and L_{bend} is the length of the bend. The problem is that strong magnets require considerable power and weight and both can cause considerable additional expense. The field strength in a long solenoid is:

$$B = \frac{\mu I n_{turns}}{L_s} \quad (12)$$

Where μ is the magnetic permeability of free space (1.26×10^{-6}), I is the current in the wire, n_{turns} is the number of turns (wraps around the solenoid) in the wire, and L_s is the length of the solenoid. The power needed to drive the solenoid at steady state is therefore:

$$P = I^2 R = \frac{I^2 2 r_s n_{turns} \rho_e}{r_w^2} \quad (13)$$

Where r_s is the radius of the solenoid, ρ_e is the electrical resistivity of the wire material, and r_w is the radius of the wire. Equation (13) demonstrates that the power required to drive the solenoid can be reduced by increasing the wire radius, or the total mass of wire (more copper means less resistance and thus less power):

$$P = \left(\frac{2 \pi B r_s L_s}{\mu} \right)^2 \frac{\rho_e \rho_m}{m_w} \quad (14)$$

Where ρ_m is the density of the wire and m_w is the total mass of wire. To reduce the costs associated with the power and copper needed, therefore, one should reduce the solenoid field strength, radius and length. Then the number of turns or wire diameter can be adjusted to yield a convenient voltage or current.

4.2.2 Magnetic Transport Code Simulations

The equations given above were used to make initial estimates for the required magnetic field strengths. The system was then modeled explicitly with the TRICOMP field codes to

determine the z-dependent magnetic field for various configurations of magnets. These fields were then used with the TRICOMP electron trajectory code to see if magnetic reflection would occur even without scattering in the air. Following that the TRICOMP-derived fields were inserted into the Integrated Tiger Series (ITS) code for beam transport in air. (The cylindrical version of ITS is called CYLTRAN). CYLTRAN is a Monte Carlo code that follows the paths of individual beam electrons through the accelerator and as they scatter off air molecules. It includes the effect of magnetic fields and determines energy deposited by the beam electrons in air and other materials as the electrons slow down.

Figure 4.2.3-A4 shows the geometry modeled for the magnetic field calculation. The magnets are all cylindrical solenoids and are labeled with arrows. The beam transport hardware is also shown, as well as the major HAWK tank structures. The nozzle throat is at $z=0$. In actuality the nozzle magnets were at roughly a 45-degree angle relative to the beam line axis, but for this simulation the nozzle was treated as though it was aligned. In this layout, there needed to be a sufficiently large gap to allow both a large bend and access to the nozzle exit for diagnostics. The diagnostic gap chosen in the model was 45 cm. The actual bent configuration near the nozzle is shown in Figure 4.2.4-A4 for reference. In Figure 4.2.3-A4, the cathode is on the centerline the left edge of the box labeled “HV Deck”. The numerous detailed magnets between the accelerator and nozzle will be described later; they were tailored to accommodate the various pumps, valves, and apertures in the transport system.

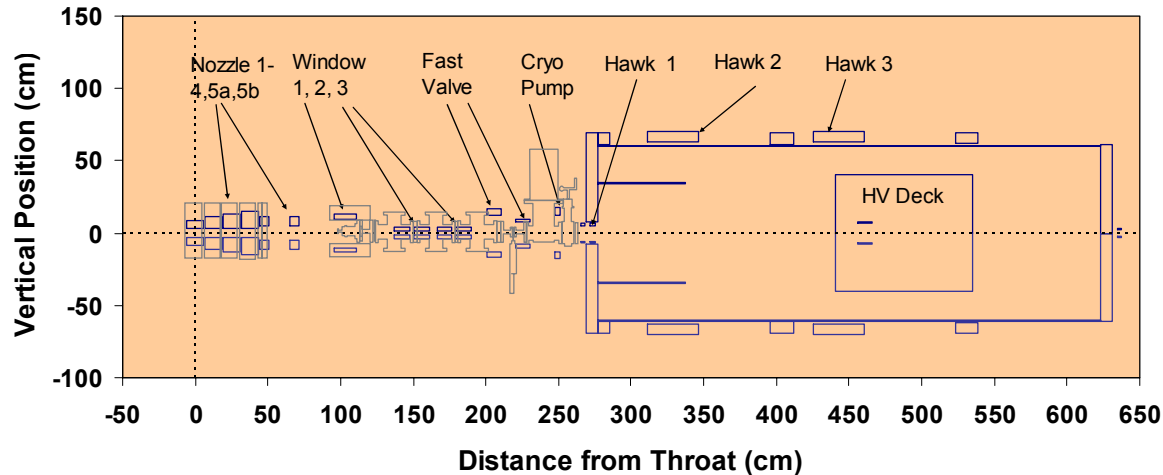


Figure 4.2.3-A4: Magnet configuration for the TRICOMP model.

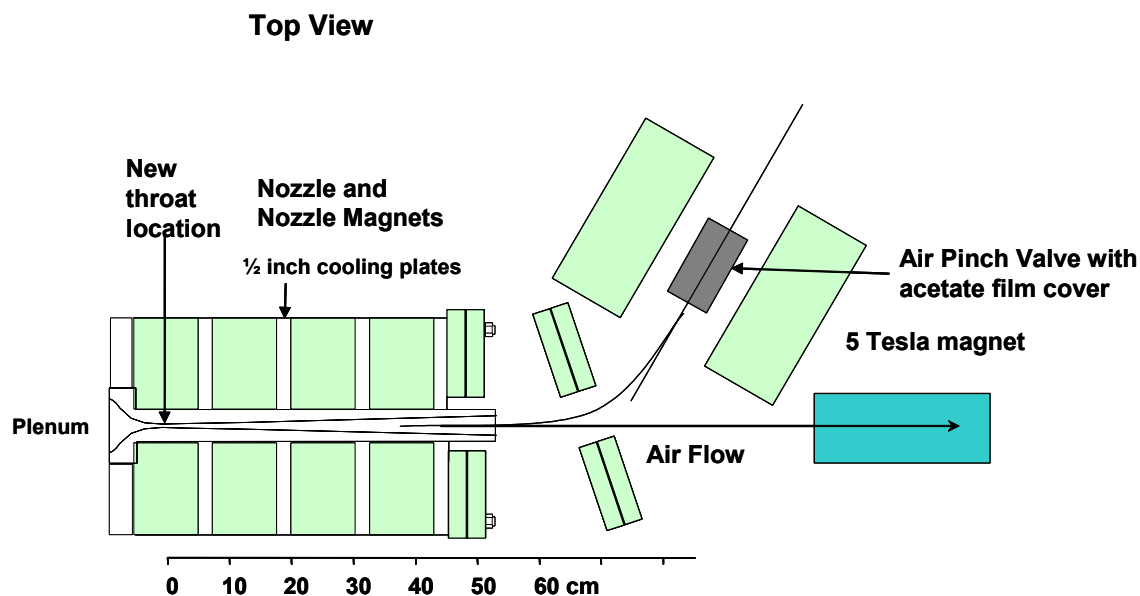


Figure 4.2.4-A4: Configuration of magnets at the nozzle and the bend in the beam path.

Figure 4.2.5-A4 shows the resulting magnetic field along with the magnet radii for the copper windings, in meters. The field strength at the cathode ($z=441$ cm) is 0.167 T, it increases to about 2 T at $z=140$ to 190 cm where the beam enters the first two apertures of the differential pumping windows (to be described later). It then increases to 5 T at the air pinch valve that acted as the final aperture (also to be described later). To reduce power requirements, a superconducting magnet provided the 5 T field. The field then decreases to about 0.6 T to allow the beam to expand before entering the nozzle where the field slowly increases to 2 T.

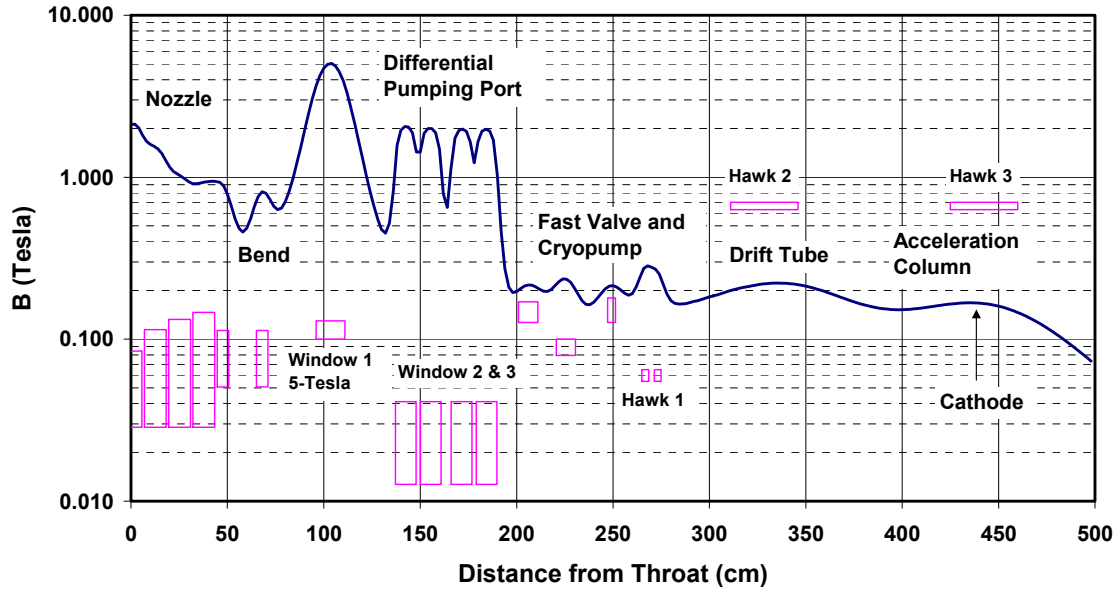


Figure 4.2.5-A4: Magnetic field from the nozzle throat to the cathode and magnet radii (m).

The magnetic field was combined with a 600 kV electric field over the vacuum stack region and used in the TRICOMP trajectory code. Figure 4.2.6-A4 shows the results for an electron emitted with 10 eV at 60 degrees and 1 cm from the axis, which is the outer radius of the HAWK cathode. There is no air in this problem, and the electron makes it through the entire nozzle without magnetic reflection. The line between 140 cm and 190 cm is the inner diameter of the differential pumping port apertures. The beam is close to these apertures edge but should have cleared them. Both the data analyses and the experiments, however, suggest that this was not the case.

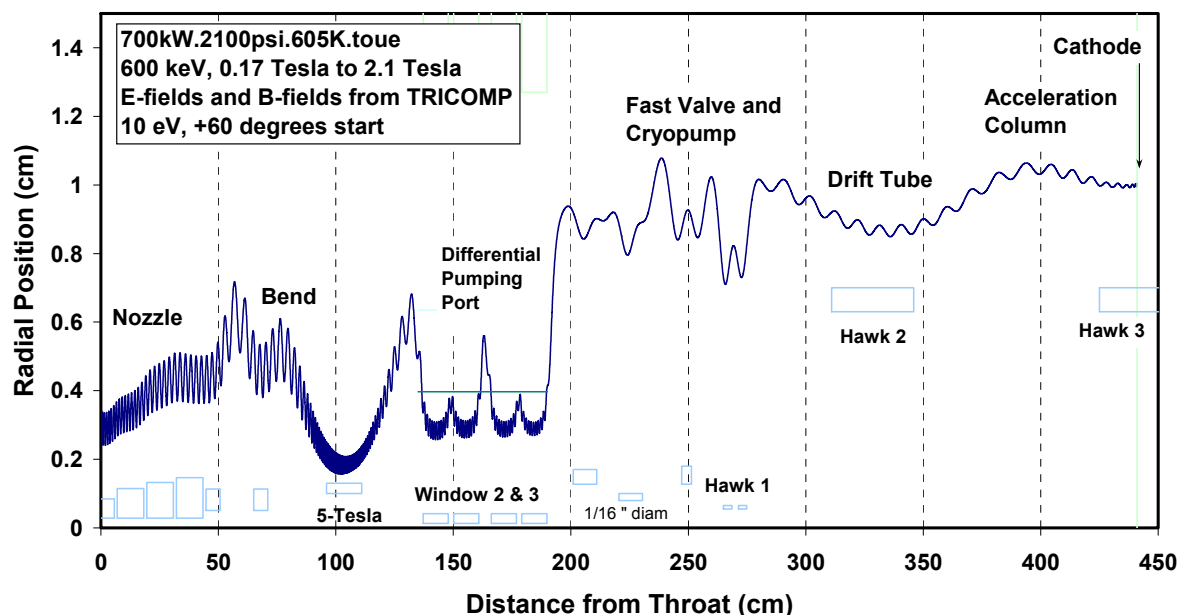


Figure 4.2.6-A4: Electron trajectory by Tricomp from the cathode through the nozzle (no air).

The TRICOMP code was not written to include beam scattering in air; the CYLTRAN code, however, was designed for that purpose. As a check on the consistency of the codes, the CYLTRAN trajectories in a vacuum were compared with the TRICOMP trajectories and were found to be essentially identical. CYLTRAN then was used in an iterative process with the gas density determined by the Princeton 2-D CFD model for a blowdown with a 14.1 MPa (2100 psia) plenum pressure. Figure 4.2.7-A4 shows a trajectory into the nozzle with blowdown air present for a 586-keV beam (after 3 iterations). The grid array used in the nozzle is also shown. The vertical scale is expanded for clarity. By comparing Fig 4.2.7-A4 against 4.2.6-A4, the effects of scattering of the electrons in the nozzle airflow can be noted. In particular, the monotonically decreasing radius of the electron beam shown in Fig 4.2.6-A4 for the region 0 - 50 cm should be compared against the more erratic behavior of the electron radius displayed in Fig 4.2.7-A4. The difference in behavior between the two cases is due to the presence of airflow in Fig 4.2.7-A4 which is absent in Fig 4.2.6-A4.

The resulting power deposition profile is shown in Figure 4.2.8-A4. The initial current needed to achieve 1 MW deposition in the nozzle air is 1.973 Amp, corresponding to an 1156 kW initial beam. Hence the predicted beam transport efficiency is about 86.5% with about 4% of the beam energy is predicted to go into the nozzle wall. It thus appears that the high transport and deposition efficiency resulting from the immersion of the cathode in an axial magnetic field should allow for the attainment of 1 MW energy deposition into blowdown air.

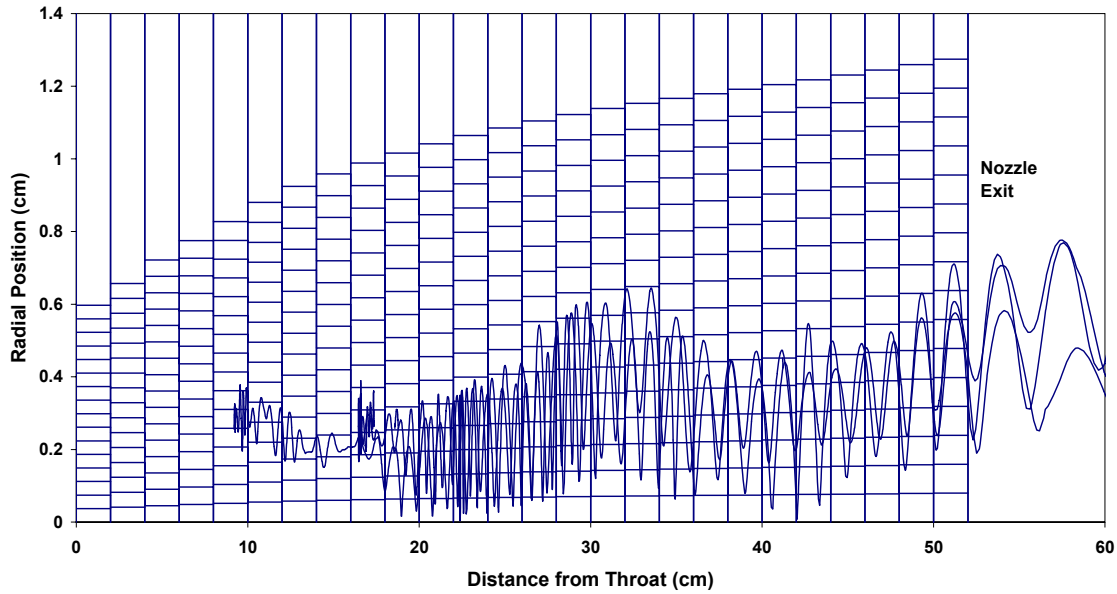


Figure 4.2.7-A4: Electron trajectories into the nozzle with blowdown air present.

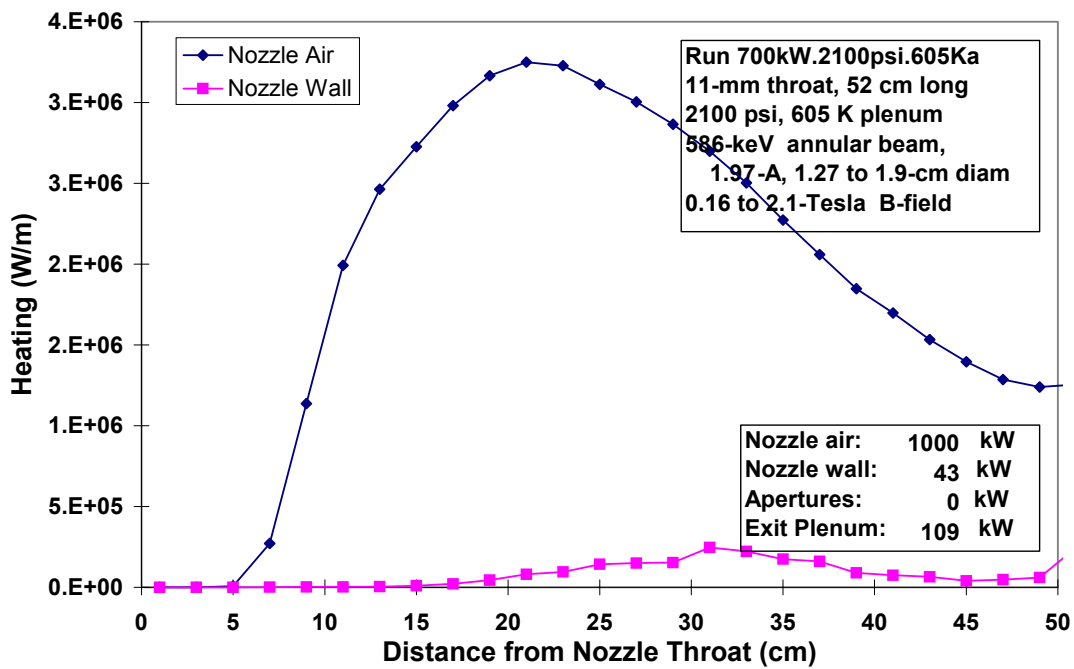


Figure 4.2.8-A4: Power deposition profiles as determined by CYLTRAN with TRICOMP fields.

The radial power deposition per gram is shown in Figure 4.2.9-A4 for various distances from the throat and integrated along z . The power density is normalized to the power density on the axial centerline, and the radius is normalized to the local nozzle radius. The intent is to have uniform heating out to a fixed fraction of the nozzle diameter at all axial locations within the

nozzle. The diameter of the flat heating zone is proportional to the square root of the ratio of the cathode field strength to the nozzle field strength. The amount of edge (or skirt) on the heating profile is proportional to the Larmor radius, which in turn is proportional to the beam voltage divided by the nozzle field strength. Strong magnetic fields are thus needed along the entire beam path to maintain a flat heating zone with a reasonably sharp falloff at the edges.

The initial CYLTRAN runs assuming a uniform cathode showed that the beam was much more Gaussian than desired. To overcome this difficulty within the existing time and budget constraints (i.e. the limited magnetic field strengths available), a decision was made to use an annular cathode rather than a uniform cathode. It was assumed that the beam would remain annular until it reached the air. At that point, the beam electrons would scatter into the central annulus as well as outward from the edges. It was anticipated that the adoption of an annular cathode would thus result in a relatively uniform central zone. Simulations were then carried out assuming an annular cathode with an outer radius of 0.95 cm and an inner radius of 0.635 cm. The results of those simulations are shown in Fig 4.2.9-A4. It may be seen that the curve at the nozzle exit (at 51 cm, before the beam encounters the airflow in the nozzle) does indeed show remnants of the annular shape. For comparison in Figure 4.9-A4, the dashed thick curve shows the results with the uniform (non-annular) cathode. While there may not appear to be a large difference in the curves representing the annular and non-annular cathodes, such small differences as are displayed are expected to have a strong effect on the peak temperature of the airflow.

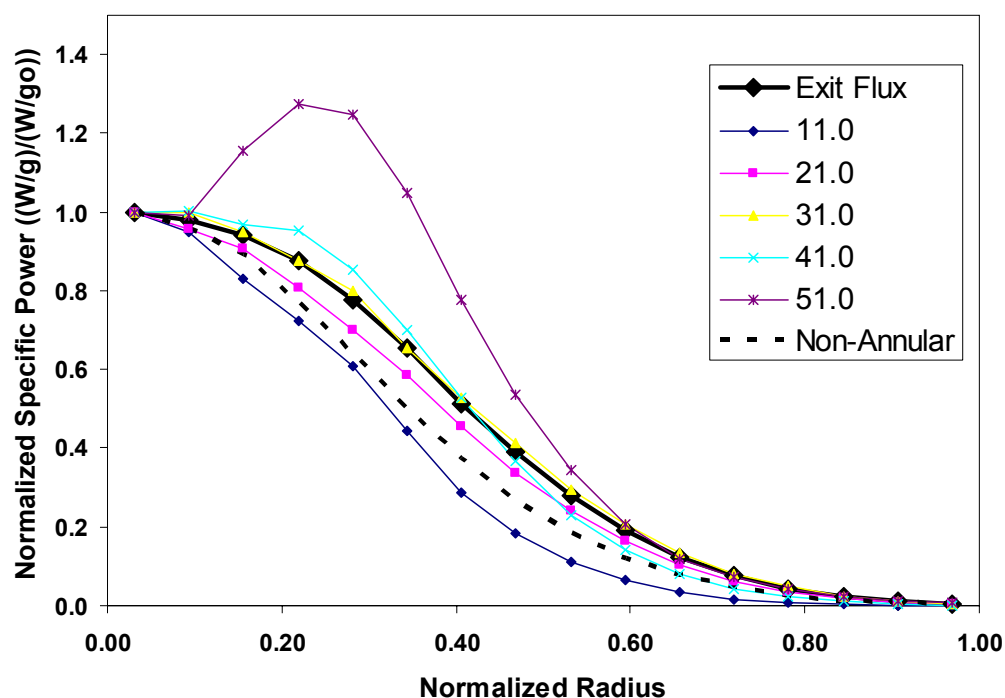


Figure 4.2.9-A4: Normalized power density (per unit volume) at various axial locations in the nozzle.

4.2.3 HAWK Magnets

The system design intent was to immerse the cathode in a 0.17-Tesla field and keep the beam on a continuous field line all the way to the nozzle. Figure 4.2.10-A4 shows the internal structure of the HAWK accelerator. HAWK is an electrostatic DC accelerator that is driven by a horizontal Van de Graaff charging system. The accelerator stack and charging system (horizontal series of aluminum rings and chain) was built by National Electrostatics Corporation (NEC, Madison, WI). The drive electronics (aluminum box to the right) and the rest of the system were built by Beta Corporation (of Titan, in San Diego, CA). The accelerator was designed to deliver a nominal 1 Amp e-beam at 1 MeV for about 1ms.

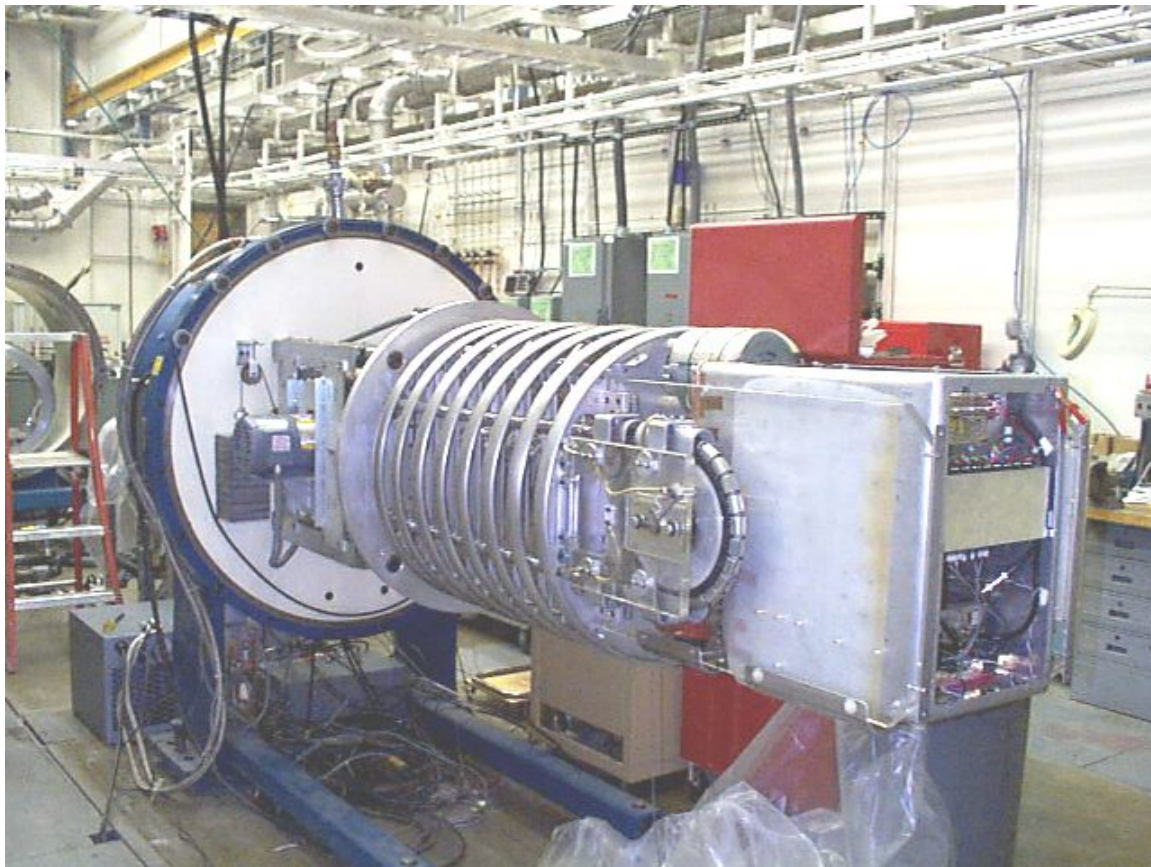


Figure 4.2.10-A4: The internal structure of the HAWK accelerator.

The difficulty with immersing the cathode in a magnetic field can be seen in the figure. The cathode is on the centerline on the left end of the aluminum electronics box. This entire system is enclosed in a steel tank flooded with 80 psi of SF_6 , and the cathode is raised to 1 MV potential (negative). Suspending and powering an internal solenoid magnet was not a feasible option, so it was decided to surround the entire HAWK accelerator and tank with a large solenoid magnet near the cathode. Figure 4.2.11-A4 shows the winding of one of the large

HAWK magnets around the HAWK tank. A separate support stand and motorized winder proved to be useful.



Figure 4.2.11-A4: Winding HAWK Magnet 3 around the HAWK tank.

Transport of the beam down the accelerator stack required a continuous magnetic field. Figure 4.2.12-A4 shows the region of HAWK between the low-voltage end of the accelerator and the front face. The electric motor and the magnetic steel supports near the beam transport tube were reasons for concern in positioning a magnet around this section of the HAWK. And an even greater concern was the 3-inch thick magnetic steel faceplate of HAWK (far left in the picture). One alternative was to insert a long solenoid inside the beam transport tube in conjunction with another magnet around the HAWK just to the right of this position. This was attempted; it was found, however, that the internal solenoid impeded the accelerator pump-down. Hence the magnet was removed and, instead, an external magnet was inserted inside a small gap in the faceplate.

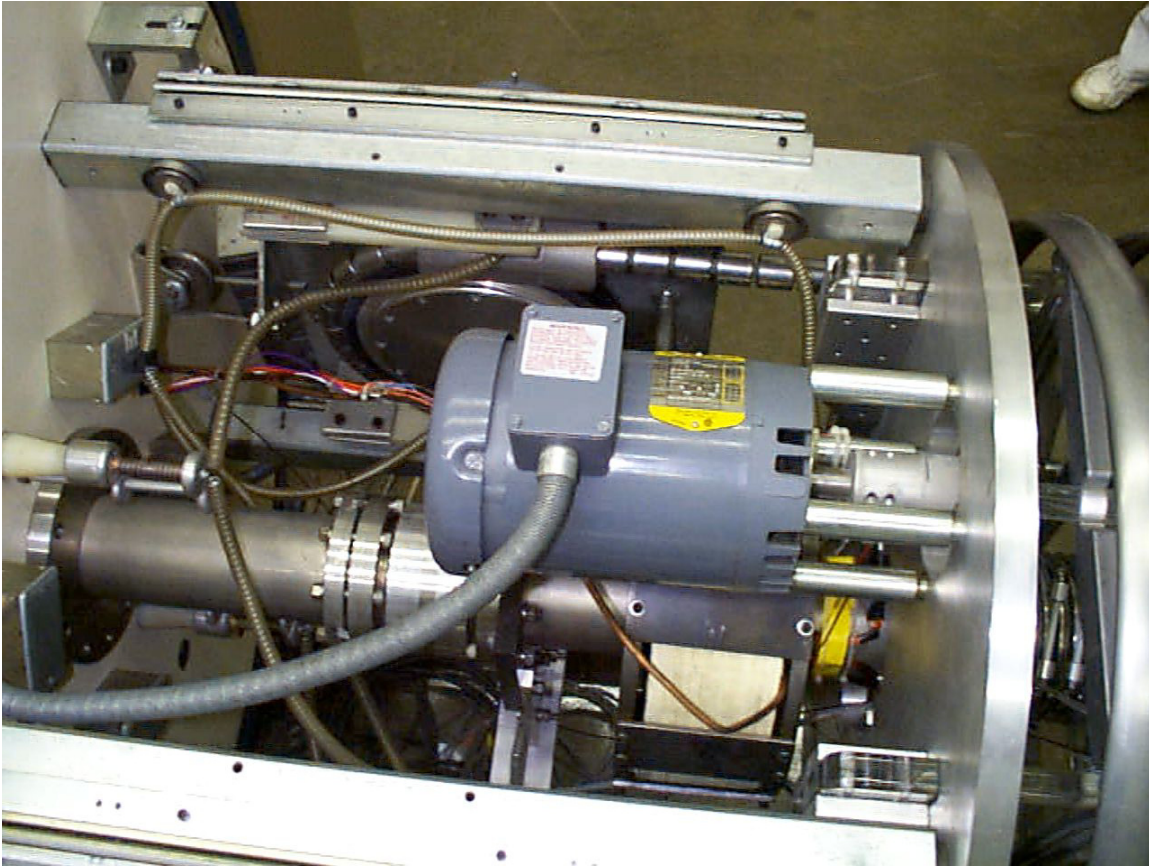


Figure 4.2.12-A4: Beam transport tube inside HAWK (below motor).

Figure 4.2.13-A4 shows the final configuration of magnets around the HAWK accelerator. Part of the differential pumping station is also shown (and will be described later).

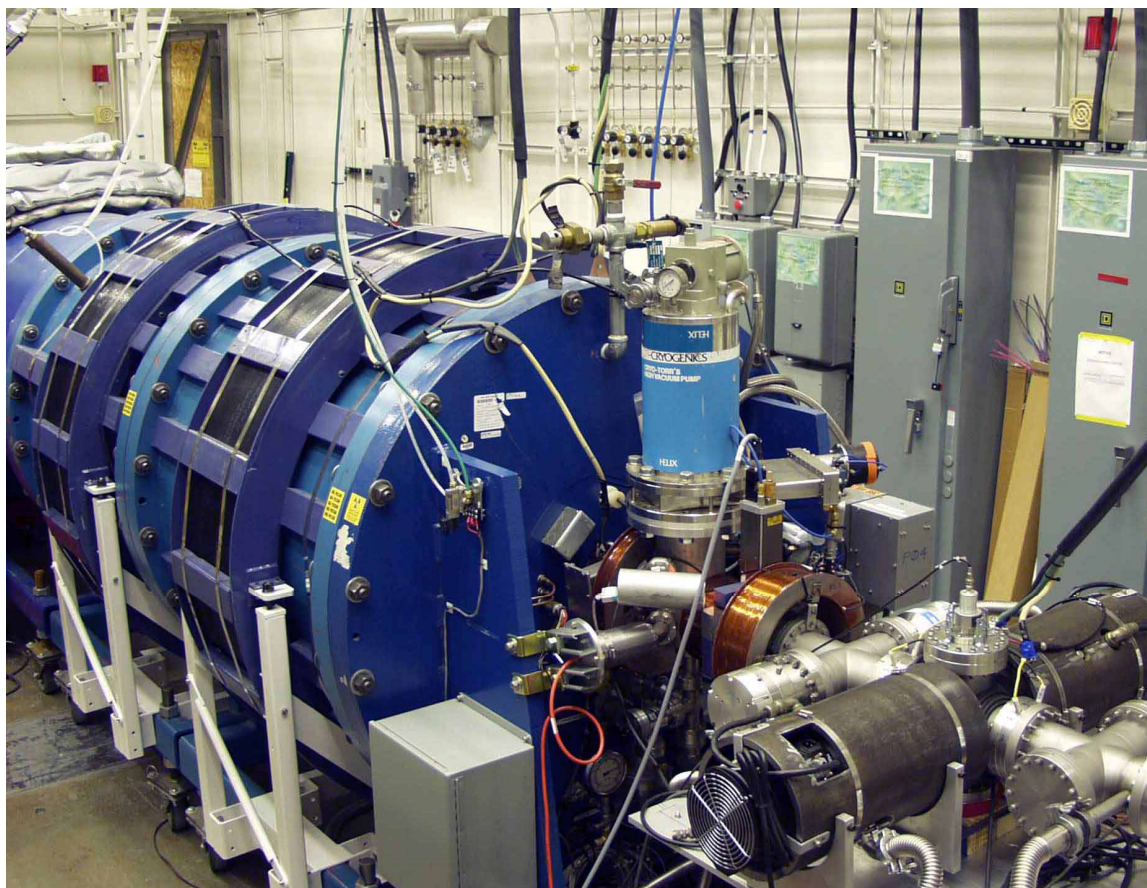


Figure 4.2.13-A4: HAWK accelerator with magnets around it.

4.2.4 High-Voltage Deck Electronics

The HAWK cathode was powered, triggered, and controlled by electronics situated on the high voltage deck within the accelerator (the aluminum box at the far right in Figure 4.10-A4). This deck operated at a large negative potential during the beam shot. This deck was also totally immersed in a 0.17 Tesla magnetic field. When operating, the HAWK magnets were pulsed for only about 1 second in order to limit the draw on the lab circuits, as well as limit their temperature increase. During the pulse, the cores of the various transformers on the HV deck experienced a force and had a slight change in electrical performance. During initial tests of the system it was determined that all transformers as well as the deck power supplies had to be secured in an improved fashion. In addition, one transformer had to be shielded from the field in order to recover its field-free performance.

The HAWK cathode current was switched by a tetrode, a vacuum tube with radially flowing electrons. The output of this tube was reduced in the presence of a strong magnetic field. Initially, it was thought that the tube would still deliver a sufficient amount of current. During the 1 MW experiment, however, it proved necessary to shield the tube with iron and move it into a zone of lower field strength. Figures 4.2.14-A4 shows the tube internal grids and the final shielded position of the tetrode.

It is not certain that all the difficulties in the electronics caused by the applied magnetic field were mitigated. Some of the HAWK machine breakdowns may have been due to this field. The accelerator for the next experiment is being designed so that all of the electronics are located remotely from the magnetic field. Only the cathode will be located within the field, and the voltage for that cathode will be delivered along non-magnetic conduits.

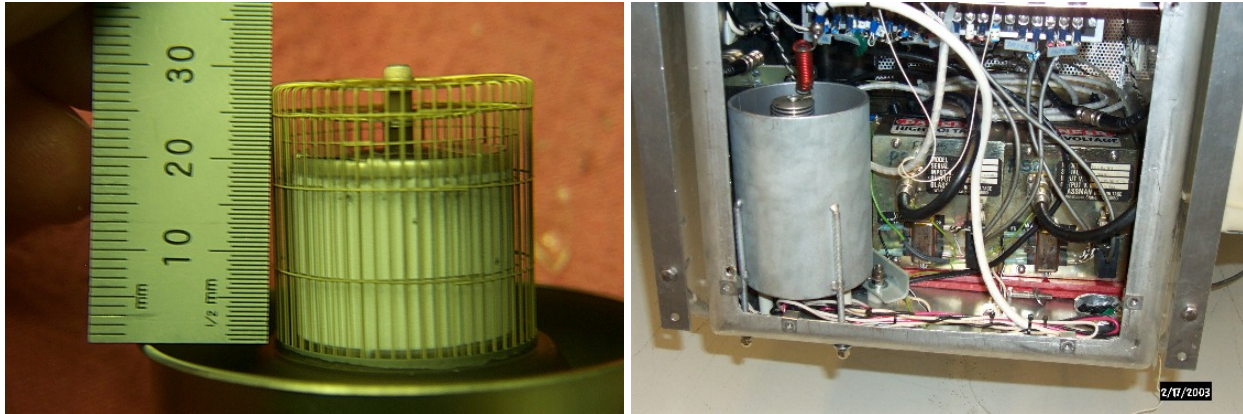


Figure 4.2.14-A4: Internal structures of the cathode tetrode and HV deck after it was moved and shielded.

4.3 Upgrade to 5 ms Duration

To enable the HAWK to produce a longer-duration beam at high powers, three major changes had to be made. First, the large capacitor bank that drove the beam had to be expanded. Second, the small capacitor on the high voltage deck that drove the cathode had to be upgraded. Third, the beryllium foil that separated the 10^{-8} Torr vacuum of the accelerator from room air had to be replaced with something that could tolerate higher powers for longer durations.

4.3.1 Large Capacitor Bank Upgrade

To accommodate the larger total energy requirements, it was decided to increase the number of stages of the HAWK from 10 to 13 stages with two large capacitors per stage, each 27 nF and each rated for 100 kV. This design yielded a total stack capacitance of $26 \times 27 / 13 = 54$ nF. It should be noted that when this arrangement was charged to an initial stack voltage of 900 kV, each capacitor would be charged to only 69.2 kV (69% of rated) and the stored energy in the stack would be $0.5 \times 0.9 \times 0.9 \times 54 = 21.9$ kJ. Table 4.3.1-A4 demonstrates that this arrangement is sufficient for 5.9 ms of beam operation with 1 MW deposited into the nozzle air assuming 25% energy loss from the capacitors to the nozzle air and 20% droop in the beam voltage (900 kV to 720 kV).

Table 4.3.1-A4: HAWK capacitor requirements for the 1-MW experiment

Capacitors in parallel per stage	2
Number of stages in series	13
Capacitance per capacitor	27 nF
Rated voltage per capacitor	100 kV
Total capacitance of stack	54 nF
Initial voltage on capacitor stack	900 kV
Initial voltage per capacitor	69.2 kV
Remaining voltage at beam cutoff (20% droop)	720 kV
Total energy delivered to beam	7.87 kJ
Fraction of beam energy assumed deposited in nozzle air	75%
Beam duration with 1 MW deposited in nozzle air	5.9 ms

To accommodate the additional stages, the cylindrical end-section of the HAWK tank was extended and the support for the capacitor stack was modified. Figure 4.3.1-A4 shows the extended tank with the new capacitors. As the experiment progressed, it was decided to implement a means to disconnect externally this bank from the HV deck (without opening the SF₆ tank) in order to improve the accelerator high-voltage conditioning rate. This required the removal of two stages; hence, only 11 stages were employed during the 1 MW experiment. Fortunately, the beam transport proved to be greater than 75%, and much of the data acquired was taken at less than 1 MW, so the upgraded HAWK was able to achieve up to 7 ms of e-beam injection for some of the data shots.

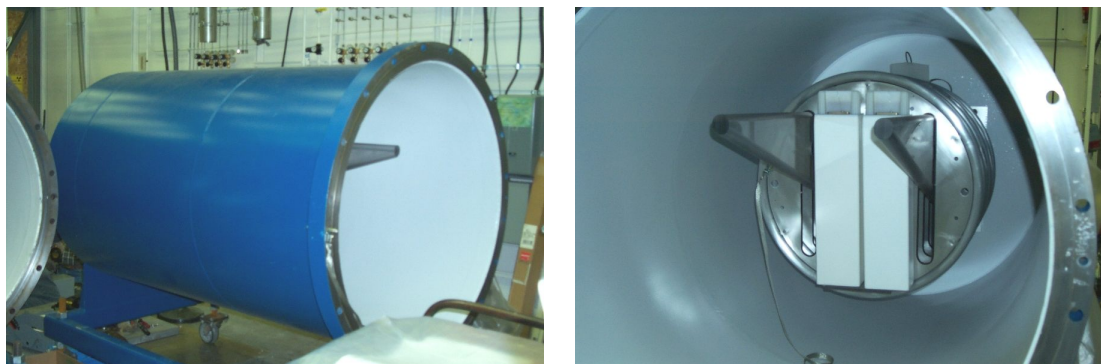


Figure 4.3.1-A4: Extended HAWK capacitor tank and new capacitors (4 out of 13 stages installed).

4.3.2 Cathode Capacitor Upgrade

The cathode voltage was up to 50 kV more negative than the HV deck, which was tied directly to the large capacitor bank. This voltage was maintained during a shot by a capacitor on the HV deck that was charged by a deck power supply (which in turn was powered by an aircraft generator sitting on the HV deck and turned by a long Lucite rod). To accommodate the longer beam duration, this capacitor had to be increased. For the next experiment, and for the Pilot Scale Facility, it is recommended that the main HV supply (capacitor bank or transformer) be

tied directly to the cathode, and that the extraction grid be biased relative to it. Since the grid does not intercept the beam current, the suggested arrangement would eliminate the need to supply large amounts of energy to it during a long shot.

4.3.3 Differential Pumping System

The previous energy-addition experiments relied on a thin beryllium foil to separate the 10^{-8} Torr vacuum of the accelerator from the room air. For short, low-power beams, this scheme worked reasonably well. For longer duration beams, however, any foil would melt during the beam shot. Hence an alternative window was needed. The solution to the window problem was a differential pumping system. In this scheme, the interior of the accelerator was exposed to the laboratory air through a small opening as the beam exited. There were, however, located at the accelerator exit, a series of pumps and apertures designed to remove the 1 atm air streaming into the system. What made this application particularly challenging was the need to maintain a continuous high-strength magnetic field to keep the beam confined, while simultaneously leaving large enough gaps between the magnets to enable adequate air removal between the stages.

Figure 4.3.2-A4 shows the initial proposed configuration of the basic system, and Figure 4.3.3-A4 shows the final product.

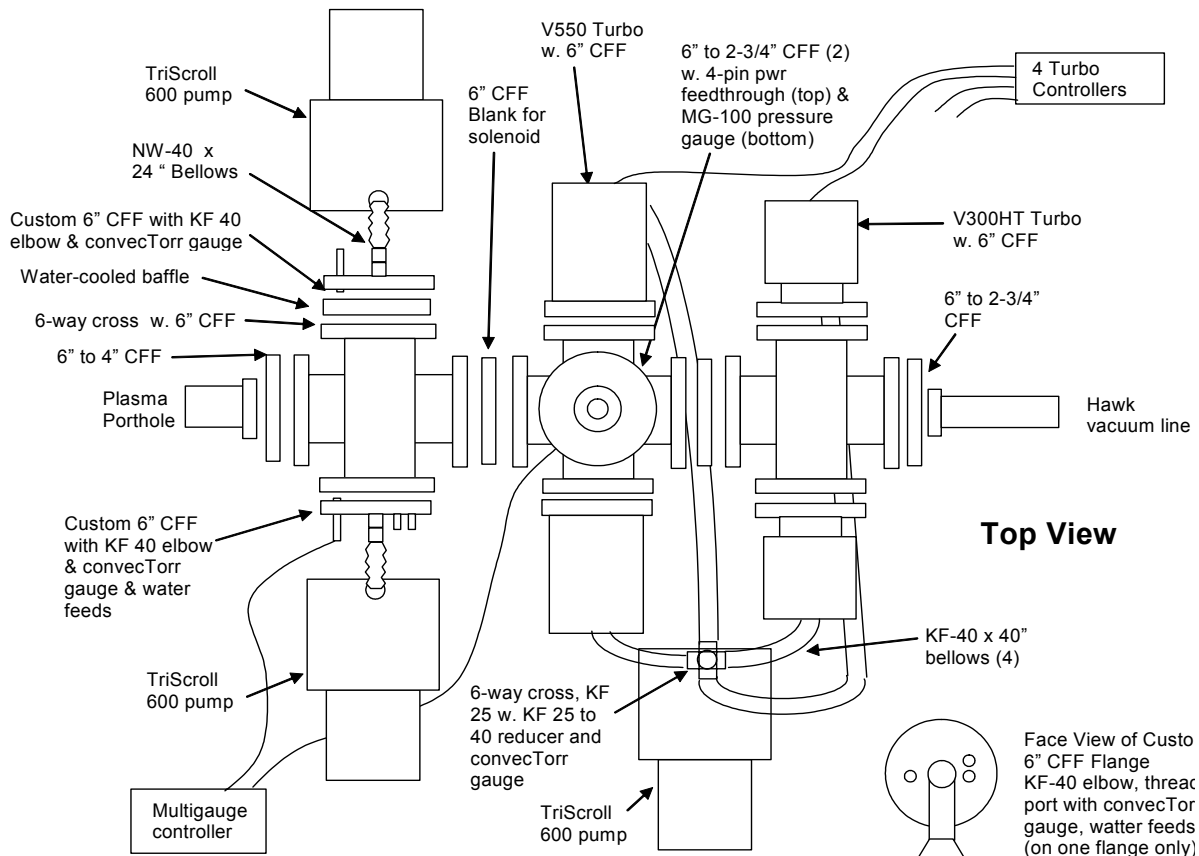


Figure 4.3.2-A4: Initial proposed configuration of the differential pumping system.

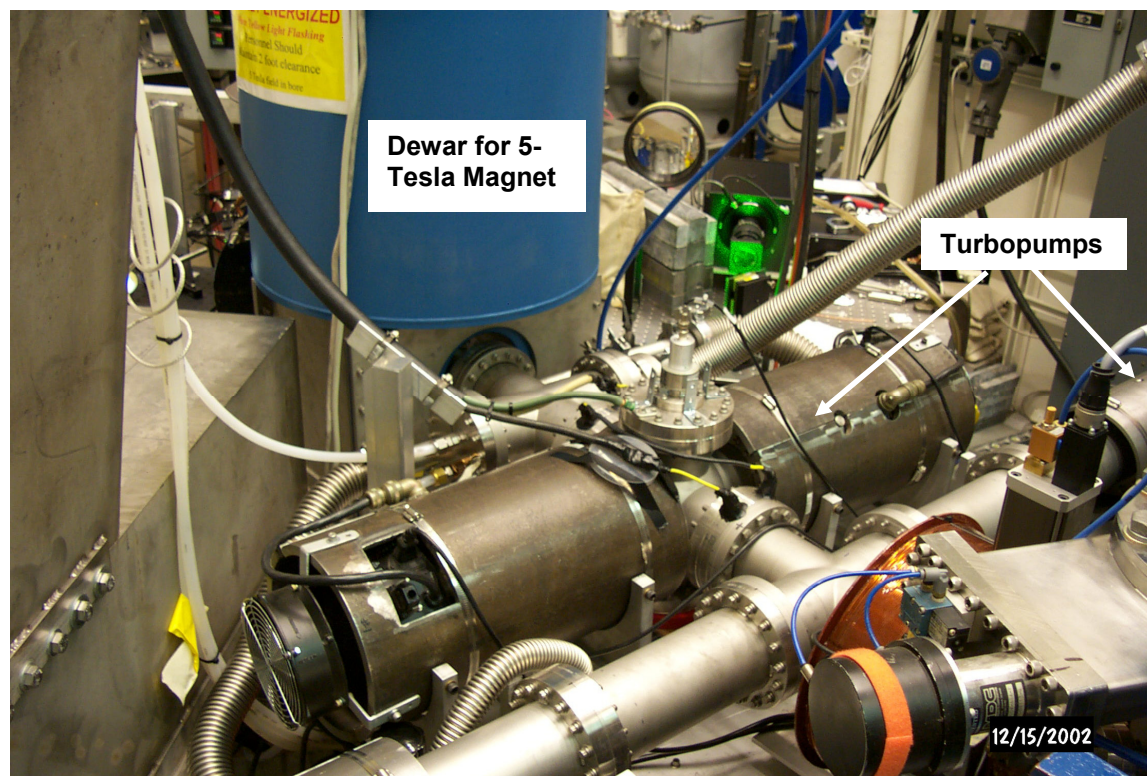


Figure 4.3.3-A4: Final configuration of the differential pumping system.

The final differential pumping system employed two large turbo-pumps and two small turbo-pumps. Because of eddy currents generated in the pump fan blades, these pumps had to be protected from the 5-Tesla superconducting magnet field as well as the pulsed field generated during beam shots. This protection was accomplished by locating the pumps remotely and by shielding them with iron. Long apertures designed to restrict the back-flow of air were positioned between these pump sets. These apertures had to be narrow so as to limit the airflow. That meant that the local magnetic field had to be strong so as to reduce the radius of the e-beam hence allowing it to pass through the narrow apertures. Because of power limitations in the lab, these magnets were constructed as small in diameter as possible and subsequently placed inside the beam drift tube near the 4-inch crosses shown in Fig 4.3.3-A4. Figure 4.3.4-A4 shows a diagram of these magnets, which were mounted on a flange that was inserted between the 4-inch crosses. It should be noted that there was also a trade-off involving the axial locations of these magnets: larger gaps between the magnets allowed better air removal by the pumps, but also allowed greater beam expansion because the field strength decreased between the magnets.

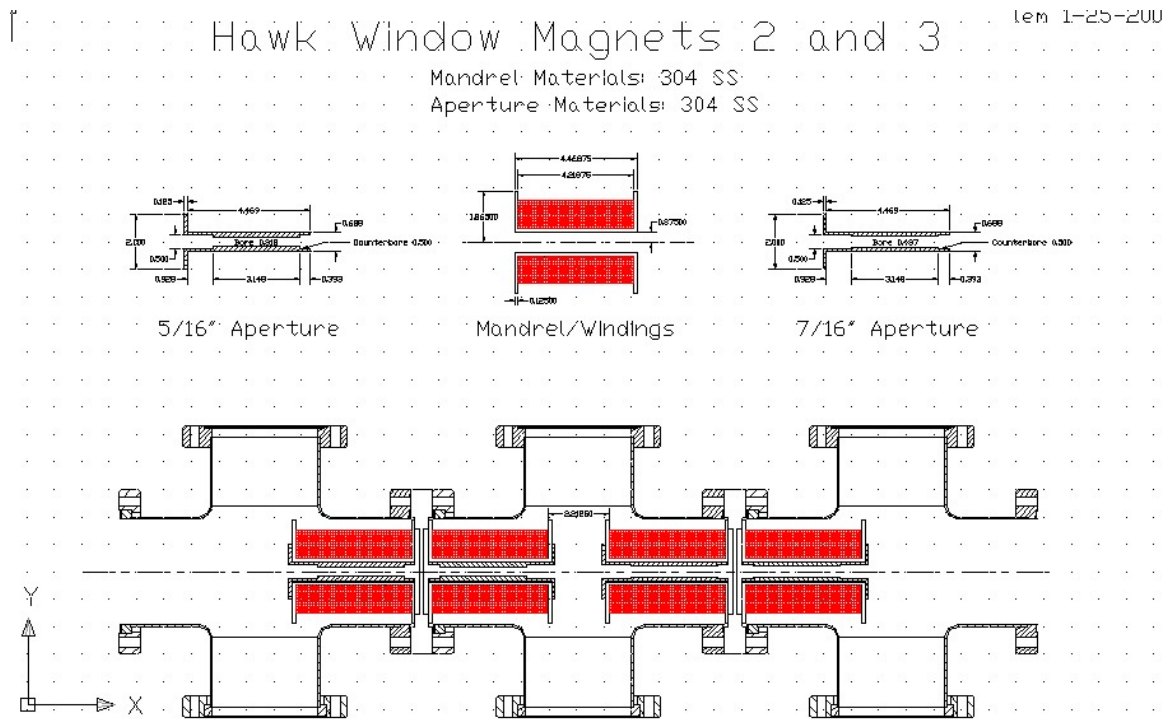


Figure 4.3.4-A4: Diagram of the magnets in the differential pumping system.

As a preliminary test of the differential pumping system, one end of the assembly shown in Figure 4.3.4-A4 was sealed with a plate and the air was evacuated from the other end. The pressures at various locations were then measured as the end plate seal was opened slightly and air was introduced into the system. Figure 4.3.5-A4 shows the pressures measured under various pressure conditions. Reductions in pressure by factors of 200 and 280, respectively, were measured between the successive stages of the system. Hence, a total pressure reduction factor of 56,000 was demonstrated for the differential pumping system. This reduction factor suggested that if the first stage, which would be open to air, could reduce the pressure of the first chamber below about 100 milliTorr, it would be possible to reach pressures suitable for the accelerator with the additional pumping of the cryo-pump on the accelerator.

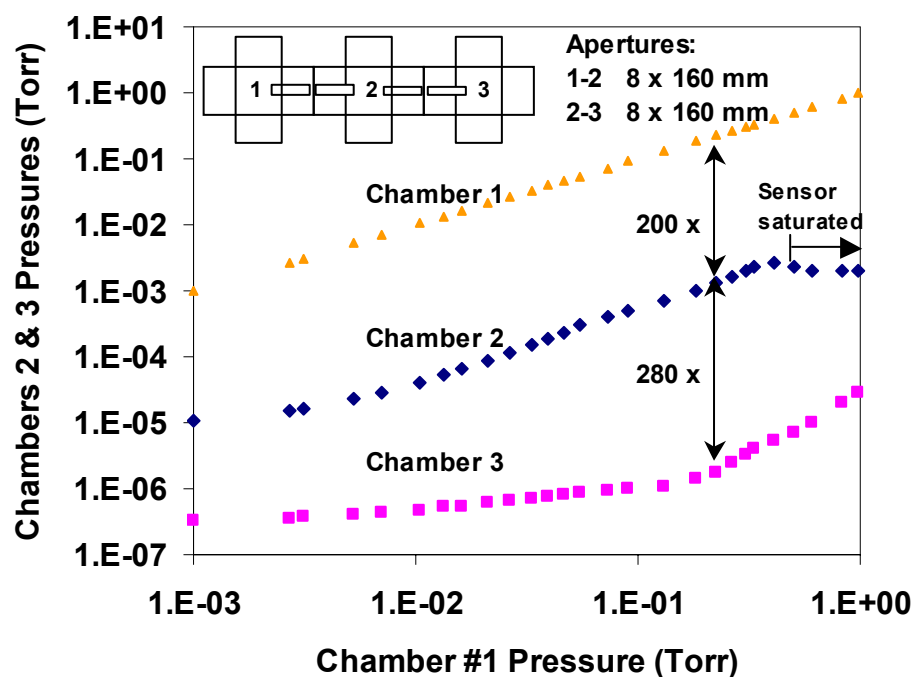


Figure 4.3.5-A4: Preliminary testing of the differential pumping system with both ends capped off and one end opened slightly (loosened bolt).

The differential pumping system was subsequently attached to the HAWK beam line. A fast-closing valve was inserted between it and the HAWK to ensure that if the system failed, the accelerator vacuum would be protected. Various magnets were also installed to transport the beam across the HAWK cryo-pump and the fast closing valve. These magnets are shown in Figure 4.3.6-A4. The fast-closing valve sensor was tested in the presence of a magnetic field and was found to be susceptible. The unit was subsequently sent out for repairs and designs were made to shield it magnetically.

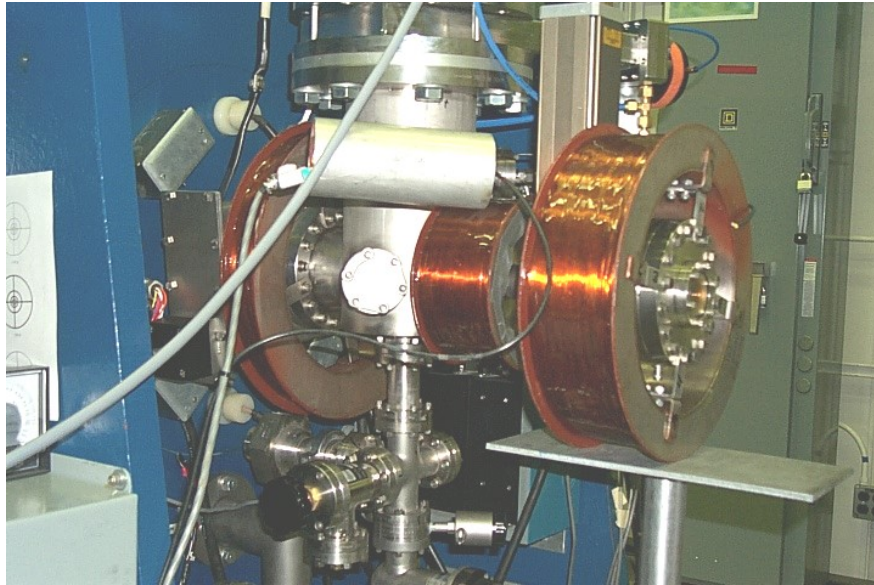


Figure 4.3.6-A4: Cryo-pump chamber and fast valve magnets.

To create another stage of differential pumping, a 2.54 cm diameter, 17.8 cm long aperture was added between the last turbo pump and the cryo-pump. The pumping system was then attached to the HAWK at the fast-closing valve. The pressure at the cryo-pump chamber (chamber 4) was then measured as a function of chamber 1 pressure while slowly bleeding in air using a blank-off at the end of the pumping system. Figure 4.3.7-A4 shows the results. In order to fire the HAWK, the cryo-pump chamber was constrained to operate below about 3×10^{-7} Torr. Figure 4.3.7-A4 demonstrates that with an adequate first stage operating, this low-pressure condition might be met. To succeed, the differential pumping system would have to yield a total pressure drop of a factor of 2×10^9 from laboratory air through a total of 5 apertures arranged in series and 5 pumping stations.

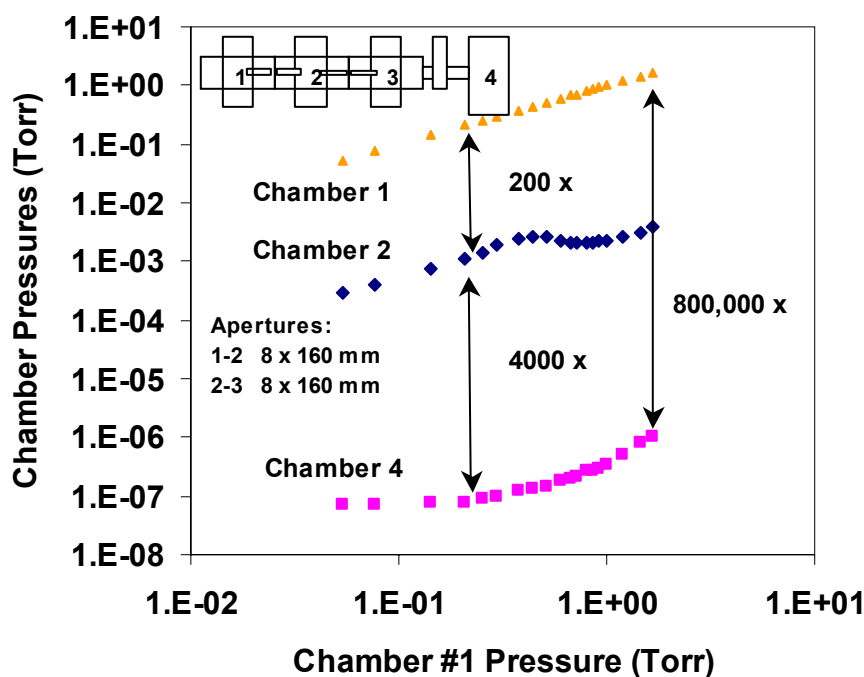


Figure 4.3.7-A4: Pressures in the cryo-pump chamber (chamber 4) and chamber 2 vs chamber 1 in the differential pumping system.

The remaining challenge was, therefore, to reduce the operating pressure in the first stage of the pumping system below 1 Torr. An important step toward achieving that goal was to make the beam as small as possible in the first aperture. The reduction of the beam radius was accomplished by using a 5-Tesla superconducting magnet at the accelerator exit. Figure 4.3.8-A4 shows the magnet assembly. The blue dewar held the liquid helium within a liquid nitrogen jacket. The magnet was located below the dewar and had a 6-inch access hole through the magnet bore. The strength of the magnet reduced the beam diameter to only 4 mm at this location thus easing the differential pumping requirements for the first stage. The size of the magnet allowed field lines to extend outward from the accelerator so that they could be used to bend the emitted e-beam into the nozzle.

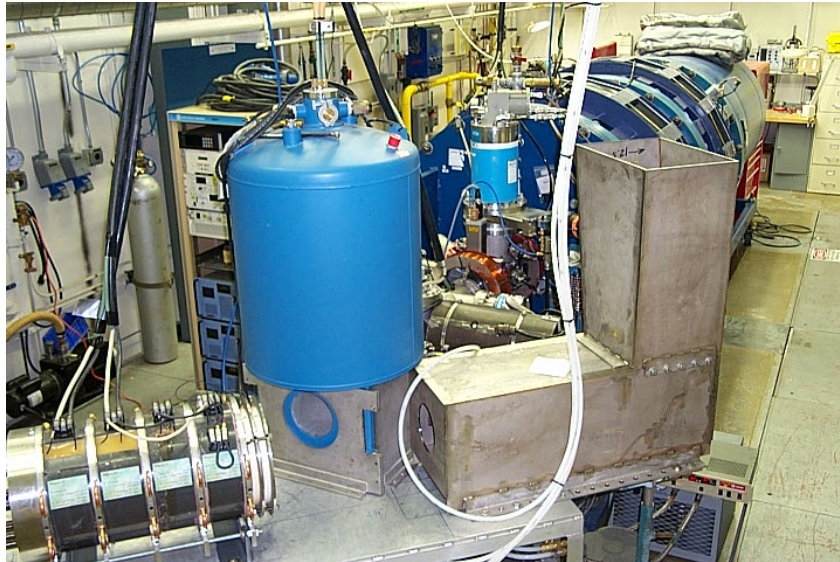


Figure 4.3.8-A4: Five-Tesla superconducting magnet.

The original intent for the first stage of the differential pumping system was to use a “plasma porthole”. A plasma porthole is a device invented by Ady Herscovitch (Brookhaven National Laboratory) that has a stack of insulated and cooled copper plates with an axial hole along the centerline. A voltage is applied across the plates and a sustained arc is created. The high temperature of the arc both rarifies the air and increases its viscosity. The net effect is a great reduction in the incoming airflow. Figure 4.3.9-A4 shows the plasma porthole cutaway, pieces, assembled, and in operation on the HAWK accelerator. All of the black tubes are for water-cooling.

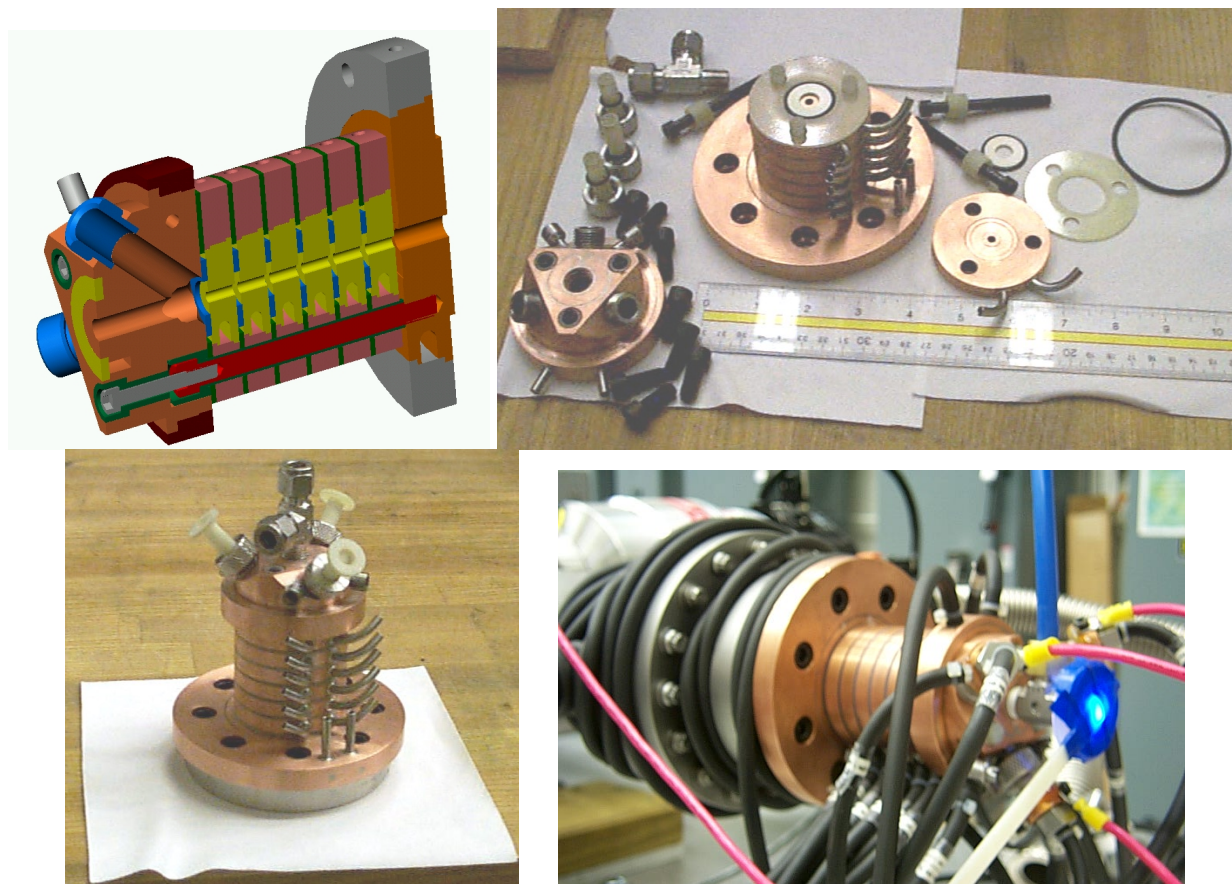


Figure 4.3.9-A4: Plasma porthole cutaway, pieces, assembled, and in operation.

During preliminary testing, the brazing on the copper parts melted. Subsequently, the parts were reassembled with a higher temperature braze (590°C instead of 265°C). Although the porthole operated successfully into 1-atm air, the power needed was fairly large and excessive heating became a concern. Following a suggestion by Dr. Hershcovitch, a venturi was installed to reduce the power requirements (shown in Figure 4.3.9-A4 as the small silver block at the end of the copper porthole and blue air tube). With the venturi set at a 40 psi driving pressure, the arc ignited with a single electrode (out of the three available), at an applied voltage of 180 V, and a driving current of 30 A. The voltage then dropped spontaneously to 70 V, and the current was reduced to as low as 15 A. With 16 A, representing a total of 1.1 kW, the porthole was operated stably for 30 minutes before being turned off (Figure 4.3.10-A4). Table 4.3.1-A4 shows some of the porthole operational parameters.

Table 4.3.1-A4: Plasma porthole operating conditions demonstrated with about 150 mTorr of argon at the porthole inlet (inlet covered by a cap).

Applied Voltage (V)	Number of Cathodes	Total Current (A)	Resulting Voltage (V)	Power (kW)	Duration (s)
150	3	75	110	8.25	30
150	3	45	80	3.6	27
150	3	30	?	?	17
150	2	30	?	?	15
150	1	15	65	0.98	90

The accelerator was then operated for 50 microseconds with 900 kV, 0.25 Amp, and an "open window" (i.e, the differential pumping system with plasma porthole operational and open to laboratory air). During this test, the accelerator showed no difficulties. The HAWK magnets were on, but the differential pumping system and superconducting magnets were not employed, so no beam was extracted through the porthole at that time.

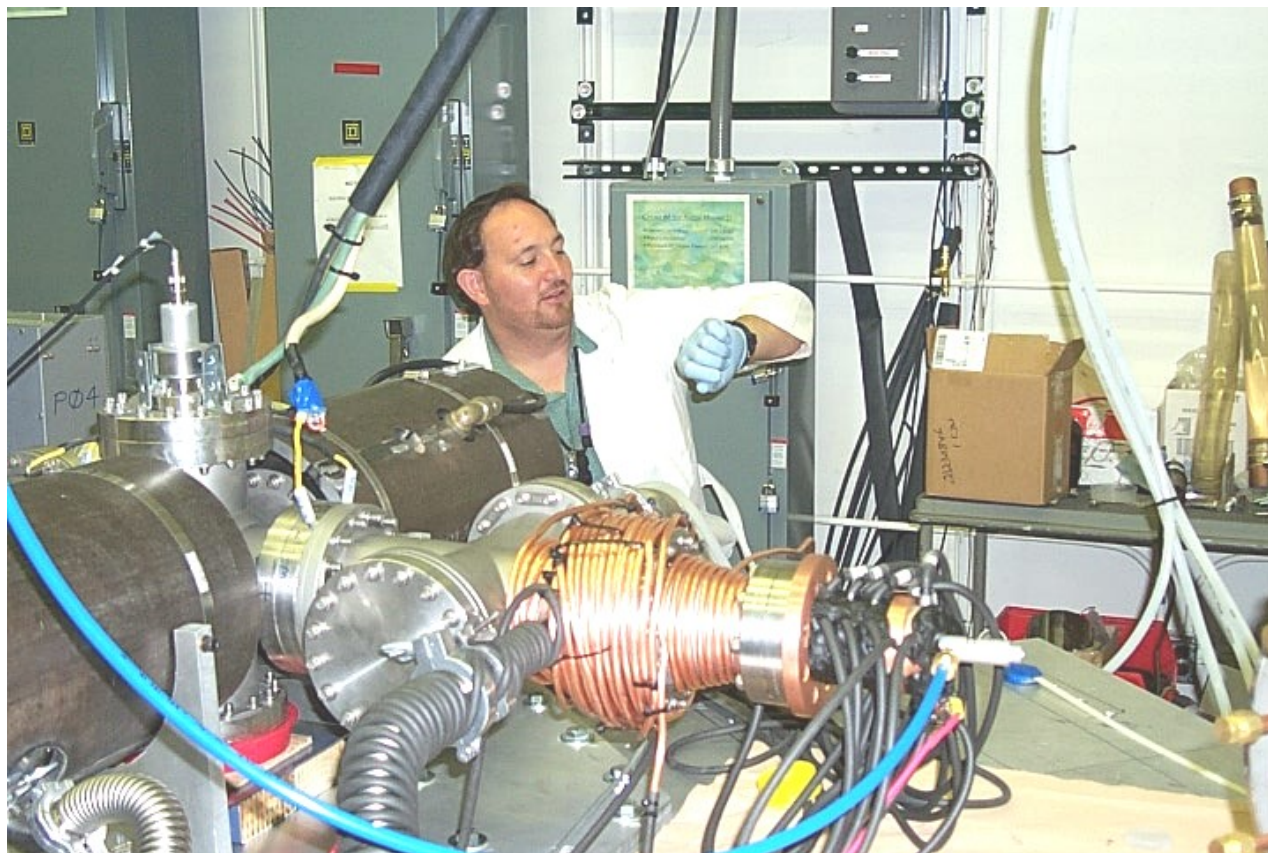


Figure 4.3.10-A4: Plasma porthole operation with venturi, 30 minute run.

The operation of the plasma porthole was then tested in the presence of the 5-Tesla magnetic field. It was determined that the porthole would operate stably if the arc electrode tip were on the aperture centerline. Under these conditions, the operational voltage with 5 Tesla increased from 70 V to 100 V, but the allowable current decreased from 15 A to 11 A. The total arc power was about the same. When the electrode tip was moved to the edge of the arc aperture, the arc would not ignite if the field strength were above about 0.02 Tesla. Even when the arc was established with no magnetic field and the field increased slowly, it extinguished at about 0.02 Tesla. This problem severely limited the utility of the plasma porthole for beam extraction because the beam would destroy the tip during a long shot.

The porthole was then disassembled to allow for beam alignment by using a larger aperture covered by a beryllium foil. It was discovered, at that time, that the first stainless steel aperture past the porthole (toward the accelerator) had melted. (See Figure 4.3.11-A4.) The damage was likely caused by some of the previously completed tests that had consumed as much as 1.6 kW for a few minutes. It was thus apparent that cooling of all components exposed to the arc-heated air stream was needed. Fortunately, the differential pumping system internal magnets were not damaged.



Figure 4.3.11-A4: Internal aperture melted by the air stream coming from the plasma porthole.

Because of the difficulties encountered with the plasma porthole, it was decided to replace it with a fast opening (and closing) valve and to rely on the rest of the differential pumping system to protect the accelerator from the small puff of air introduced when the valve was open. The fast opening valve was to be a piece of acetate or Mylar over a 4-mm diameter hole and would be replaced after each shot. The closing valve was to be an air pinch valve actuated by air pressure and made entirely of plastic (since it would be inside the 5-Tesla magnet opening). The air pinch valve was subsequently installed at the end of the pumping system (see Figure 4.3.12-A4)

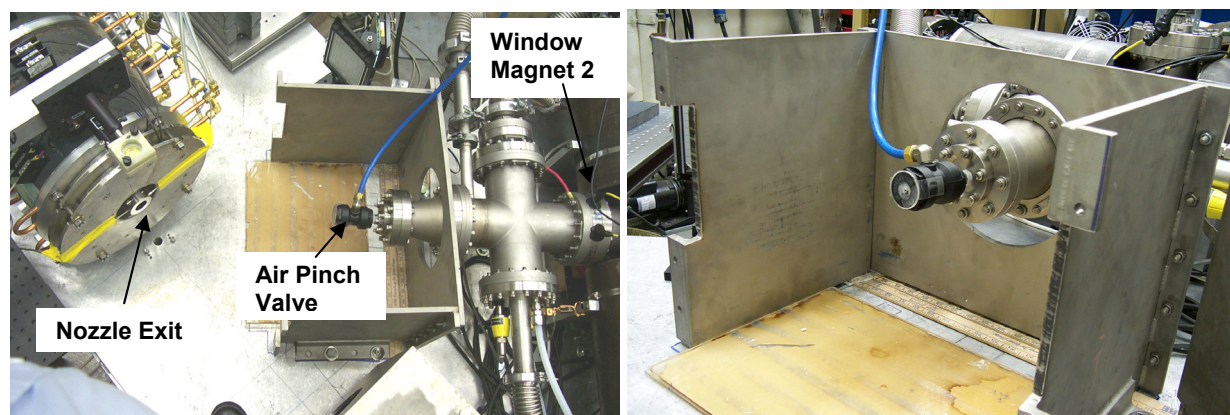


Figure 4.3.12-A4: Air Pinch Valve and 4-mm aperture at the end of pumping system and inside the holder for the 5-Tesla magnet.

Figure 4.3.13-A4 shows an example of a hole that the beam burned in a piece of acetate (standard viewgraph transparency) in 0.15 ms at 100 mA. A 3-mm thick piece of plastic was glued with epoxy to the end of the air pinch valve. The beam was used to mark the plastic at the end of the air pinch valve. The spot resulting from the beam was drilled out (5 mm diameter). The hole was then covered with a thin acetate layer held in place by scotch tape (which worked well for the few seconds that the air pinch valve was open). The beam was then extracted through the hole.

Hence, with the installation of the beam extraction scheme described above, the procedure for firing the accelerator became: 1) place a fresh piece of acetate over the opening of the 5-mm hole in the 3-mm thick plastic at the end of the air pinch valve within the bore of the 5-Tesla magnet, 2) turn on all the pumps in the differential pumping system, 3) arm the fast-closing valve trigger, 4) evacuate the HAWK cell, 5) charge the accelerator, 6) open the air pinch valve, 7) two seconds later fire the HAWK magnets, 8) 1.1 seconds after initializing the magnets, fire the beam 9) when required, the fast closing valve closed in response to a pressure rise after the beam burned a hole in the acetate (and well after the beam is finished), and 10) time the air pinch valve to close about a second after the beam firing. Using the scheme described above, the system could pump down and be ready for another shot after about 30 minutes.

Ideally, one would acquire larger pumps and use larger pumping orifices to eliminate the need for the acetate window. Within the time and budget constraints of the 1 MW program, however, the extraction system described above was the best that could be achieved.

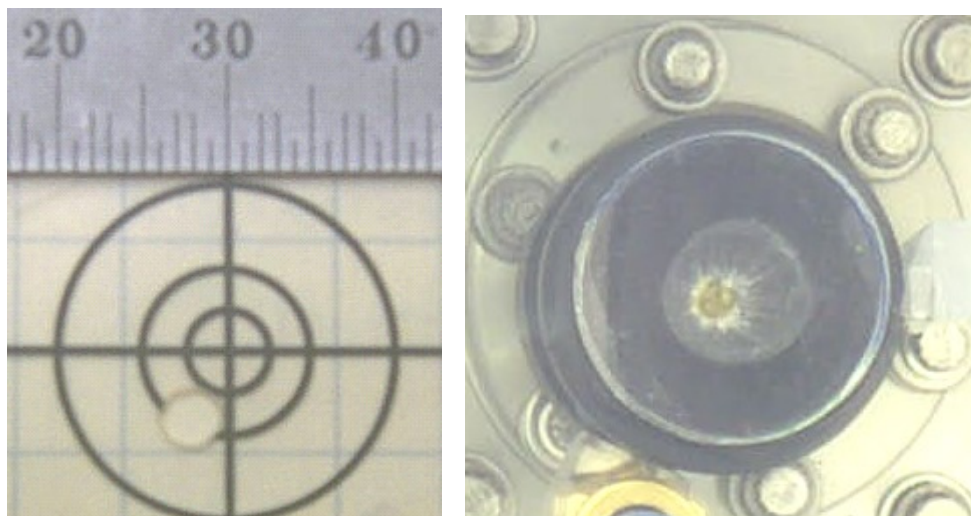


Figure 4.3.13-A4: Beam burn-through of an acetate window (0.15 ms, 100 mA) (left) and 3-mm thick plastic end cap on Air Pinch Valve with a 4-mm burn pattern in it ready for drilling (right).

The approach described above allowed for the extraction a 1 MW beam for up to 5 ms from the accelerator into open air and into the blowdown nozzle.

4.4 Better Beam Uniformity: Annular Cathode

As noted previously, use of an annular cathode allows the beam profile to be flatter in the center after scattering in air. Figure 4.4.1-A4 shows the annular cathode in its holder. The inner and outer radii are 0.635 cm and 0.95 cm, respectively. The inside of the cathode is non-activated tungsten. The cathode was activated for beam extraction simply by heating. Figure 4.4.1-A4 also shows two examples of the extraction “grid” that was placed over the cathode holder during beam operation. The grid was actually just an empty hole that established a retarding voltage until the beam was triggered by an abrupt reduction in the grid voltage. Figure 4.4.2-A4 shows the glowing hot cathode. This photo was taken in-place in the accelerator looking down the beam tube through a glass window.

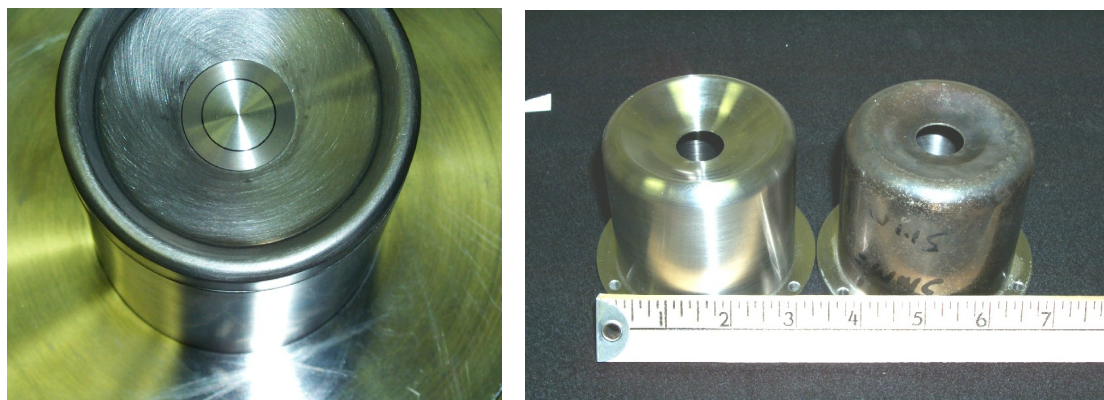


Figure 4.4.1-A4: Annular cathode in holder and two extraction “grids,” new and used.

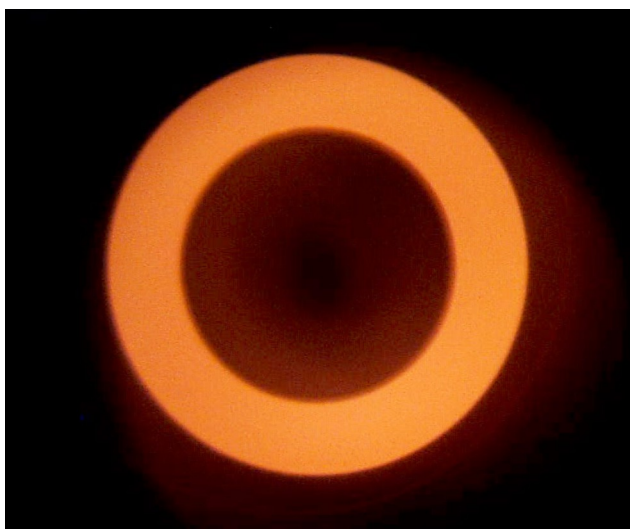


Figure 4.4.2-A4: Heated cathode in the accelerator.

Because of the reduced emission area of the annular cathode, it was necessary to reduce the spacing between the cathode and the extraction grid so as to extract more current per square centimeter. In addition, the hole in the grid was enlarged to reduce the chance of beam scraping (initial photos of the heated cathode showed an imperfect annulus, indicating that the grid was partly obstructing some of the annulus).

Normally, changing the gap diameter or spacing in an accelerator cathode is a delicate process because the beam electrons will diverge or converge depending sensitively on both the geometry and the applied voltages. In order to demonstrate the sensitivity of the HAWK injector to changes in its configuration, simulations of the cathode, grid and anode were performed using the TRICOMP code after the grid diameter was enlarged to 2.54 cm. Figure 4.4.3-A4 below shows the predicted electric field equipotentials relative to the injector cathode, grid, and anode. It also shows the trajectories for some test electrons. The four cases shown are without an applied magnetic field. The figures show radius in the vertical direction starting at the axial centerline, and z in the horizontal direction. The grid is basically a plate with an open circular hole, and the anode is a block of metal with an open circular hole. The cathode is annular, so one should ignore the electrons that start on the axis. The electrons were initially launched at 45-degrees with energies of 10 eV. The four cases shown (from top to bottom) are with the cathode at zero voltage, and the grid and anode at the following combination of voltages: (grid kV, anode kV) = (2.3, 5.5), (1.3, 5.5), (1.3, 0.0), and (1.3, -1.3). There is no voltage applied to the rest of the acceleration column.

For the first case shown, the electrons pass nicely through the grid hole and the anode hole and go into the acceleration column downstream. But the field lines bulge a bit out of the grid hole. The second case has a lower grid voltage (relative to the cathode voltage) and the field lines do not bulge as much. As a consequence, the electrons do not diverge as much as they enter the column. Nonetheless, the electrons that pass into the column will hit insulated rings located in the column and quickly build up a space charge that will retard the subsequent electrons. This will cause the electrons to hit the rings earlier and earlier until, eventually, they

hit the anode. Since the anode also is insulated, it too will build up a space charge. The last two figures show the effect as the anode voltage is reduced to zero and then charged with a negative potential. The electrons are stopped and redirected to the grid. Since the grid is grounded in the HAWK, it will not build up a charge as electrons hit it. So the remainder of the beam can continue to flow to the anode.

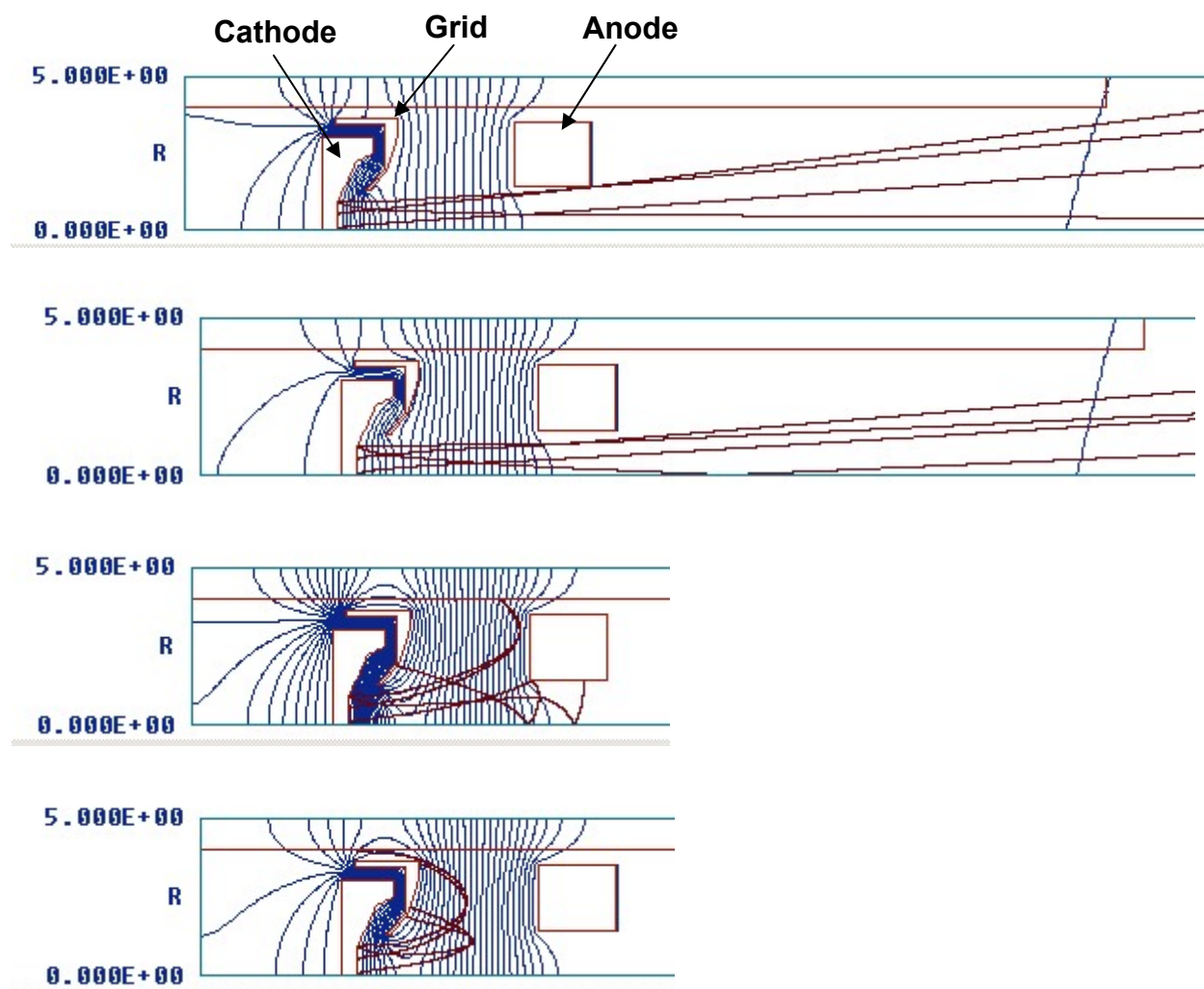


Figure 4.4.3-A4: Trajectories of 4 sample electrons from cathode in HAWK injector for various voltage combinations on the grid and anode: (2.3, 5.5), (1.3, 5.5), (1.3, 0.0), and (1.3, -1.3) for (injector, grid) in kV.

As demonstrated in the example given above, the maximum amount of current that could be extracted from the redesigned HAWK injector would be expected to depend strongly on the configuration and applied voltages of the cathode, grid and anode *in the absence of an applied magnetic field*. The projected injector performance was completely different, however, when the effects of an applied magnetic field were included in the simulation. Figure 4.4.4-A4 shows the beam trajectories with an applied magnetic field of 0.2 Tesla and a grid and anode voltage of 1.3 kV and 5.5 kV. The beam electrons follow the field lines with high precision and do not hit the

anode. The lesson learned during the modeling work described above is that the design of an injector is much simpler when the injector is immersed in an applied axial magnetic field.

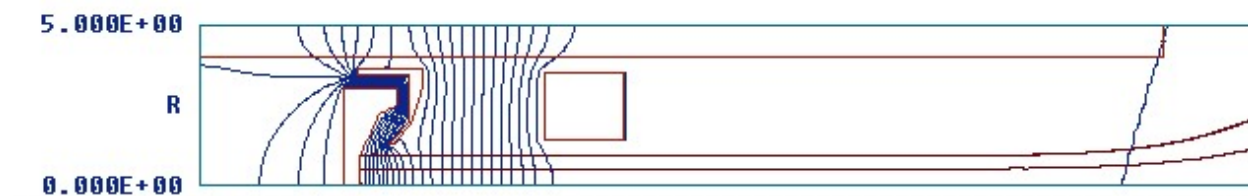


Figure 4.4.4-A4: Electron trajectories with an applied magnetic field.

To test the efficacy of the annular cathode in the modified injector geometry, an e-beam was generated with all applied magnets activated. The low-power beam was extracted through a 10-mil thick beryllium foil located just beyond the fast closing valve. The emitted beam was allowed to hit a thin acetate target. Figure 4.4.5-A4 shows the result of that test. The outer black ring on the acetate is 20 mm in diameter. The next ring is 10 mm in diameter. This is very close to the predicted size of the beam for the location shown. The figure also shows the scintillator in lighted conditions, and the annular cathode, both at about the same scale as the beam image. It should be noted that the beam is essentially a clean annulus and only starts to degrade as it passes through material. The last image in Figure 4.4.5-A4 shows the beam hitting the acetate located 8 mm from the Be foil. It is apparent that beam propagation after scattering in the foil has started to fill in the annulus. It is this effect that could lead to a more uniform beam in the nozzle (assuming a differentially-pumped open window were employed instead of a Be foil).

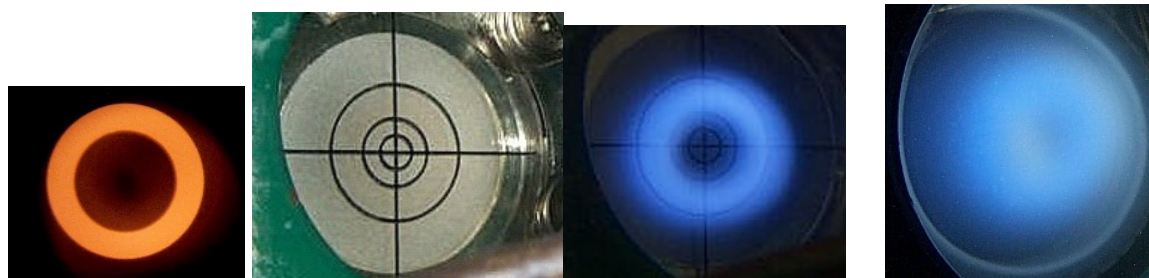


Figure 4.4.5-A4: Heated annular cathode, scintillator without beam, annular beam imaged on scintillator close to Be foil, and scintillator 8 mm from Be foil), all just beyond the fast closing valve.

The scintillator was removed from the exit plane and the beam current was measured on another shot. The beam current emitted from the cathode was measured to be 270 mA while the beam current exiting the Be foil was 245 mA. This result represented 90% beam transport through the accelerator on a strong magnetic field (See Figure 4.4.6-A4.). The transport fraction may even have been higher because some beam was backscattered in the Be foil.

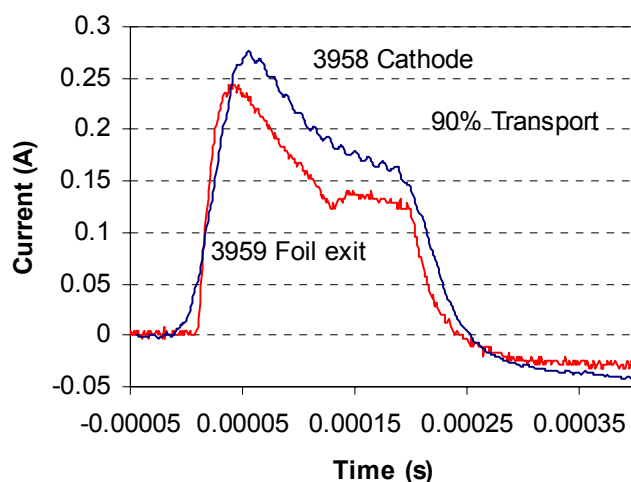


Figure 4.4.6-A4: Beam current at cathode and after Be foil. The pulses declined because the cathode bank is not connected for this test.

The beam propagation through the apertures of window magnets 2 and 3 in the differential pumping system was also tested. The beam location was adjusted by tilting the cryo-pump magnet upward slightly. Figure 4.4.7-A4 shows the resulting beam after passing through the two sets of apertures. The inner circle shown is 5 mm in diameter and the outer is 10 mm in diameter. For this shot the field strength of the magnet surrounding the cathode was adjusted to make the beam slightly smaller so as to compensate for some beam growth due to scattering off sharp changes in fields during transport. This was accomplished by firing the beam only 0.4 s into the magnet pulse when the field was not quite fully established.



Figure 4.4.7-A4: Beam after passing through the cryo-pump aperture and two window magnet apertures.

Beam extraction was then attempted through the center of the 5-Tesla magnet. This was done with a large aperture and a 10-mil Be foil inside the 5-Tesla magnet. A 120 mA, 700-kV, 150-microsec beam was extracted into air through the foil. Figure 4.4.8-A4 shows an imprint of the annular beam at the Be foil burned into acetate. The beam diameter is 3 mm, in agreement with code predictions.

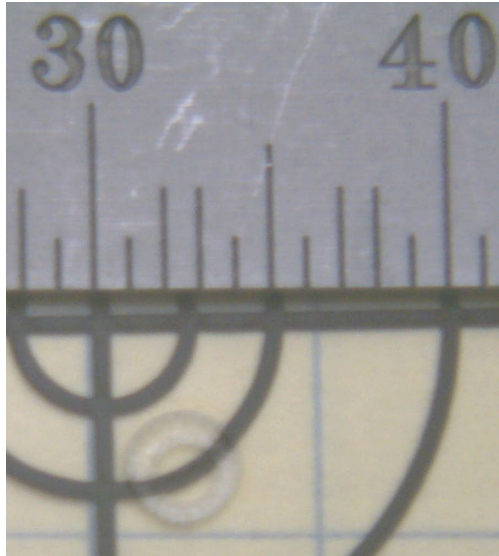


Figure 4.4.8-A4: Annular beam imprinted on plastic target after passing through the cryo-pump aperture and two window magnet apertures.

4.5 Bending Angle of 45 Deg

The beam had to be bent about 45 deg in order to be inserted into the nozzle without disturbing the airflow. The general configuration of this bending is shown in Figure 4.2.4-A4. Initially, no bending magnets were used between the nozzle exit and the 5-Tesla magnet; rather, the unadjusted bend in the magnetic field was used to guide the beam. A 3-D magnet code called MAZE was used to map the field around the bend. Figure 4.5.1-A4 shows the field. The beam will follow the center field line into the nozzle exit. It also will expand as it passes the weak section of the field between the magnets and then contract as it enters the nozzle.

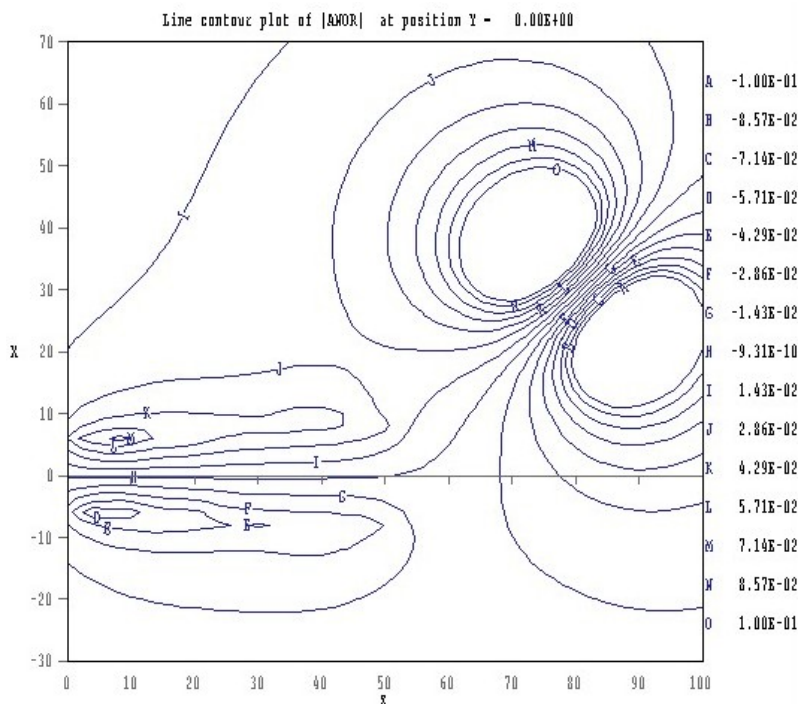


Figure 4.5.1-A4: Field plot from 5-Tesla magnet (upper right) to nozzle (lower left).

To test the propagation of the e-beam from the accelerator to the nozzle, the beam was extracted into air through a 5-mil thick Be foil at the midpoint of the 5-Tesla field. It passed around the bend and impacted an acetate scintillator centered at the exit of the nozzle. After several iterations involving the moving and tilting of the 5-Tesla magnet, the beam was centered on the nozzle exit. This alignment, however, resulted in the beam being off-centered at the Be foil. Figure 4.5.2-A4 shows the beam centered on a target at the exit of the nozzle. Figure 4.5.3-A4 shows the beam intensity along a horizontal cut just above the beam center. It is fairly flat because the beam filled in the center of the annulus as it scattered in the air. The drops in intensity evident in the figure are due to the target rings. For longer duration beams it can be anticipated that the beam would heat and thin the air and that, therefore, the beam profile would be more annular near the nozzle exit. The beam current was measured at the nozzle magnet surface for a non-centered case. It was 75% of the cathode current, after being extracted through a 5-Tesla field.

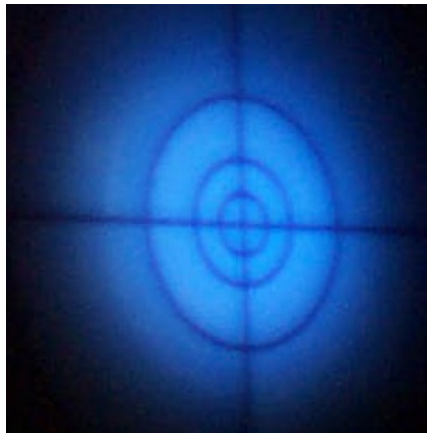


Figure 4.5.2-A4: Beam hitting nozzle exit at just above the midpoint.

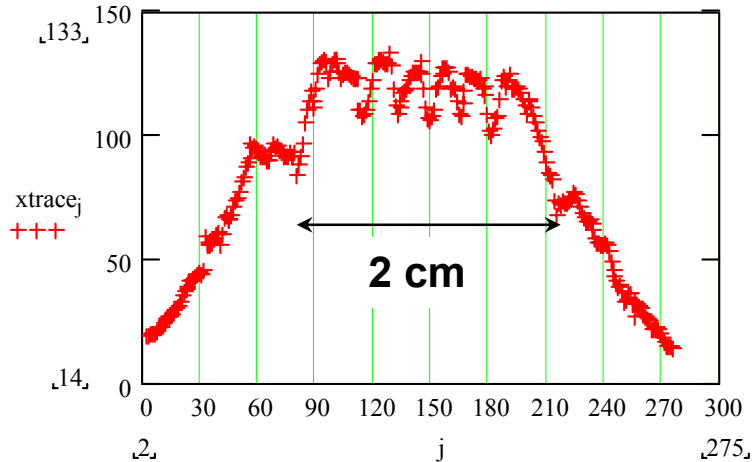


Figure 4.5.3-A4: Beam intensity vs. position horizontal cut. Dips are target rings.

After centering the beam at the nozzle exit, the acetate was replaced by a graphite beam stop that was grounded through a 50-Ohm resistor to serve as a beam current diagnostic. The beam intensity and duration were then increased.

Figure 4.5.4-A4 shows a 200-kW, 650-kV, 0.3-A, 0.15-ms beam (29 J) extracted through an air pinch valve and bent around a 45-degree bend into the nozzle. Figure 4.5.5-A4 shows a 550-kV, 0.8-A, 1-ms beam (440 J). The beam lit up the graphite target and apparently caused some of the graphite blow-off dust to burn. Note also the flare inside the 5-Tesla magnet (right) from the acetate window burning through. The camera for this setup was a Kodak DC240 digital camera. It had the ability to be fired remotely by computer for durations as long as 10 seconds, as well as setting the focus and zoom remotely. This was useful since it allowed taking several shots remotely without having to discharge the accelerator and enter the HAWK cell. These were all open-shutter shots in a dark room.

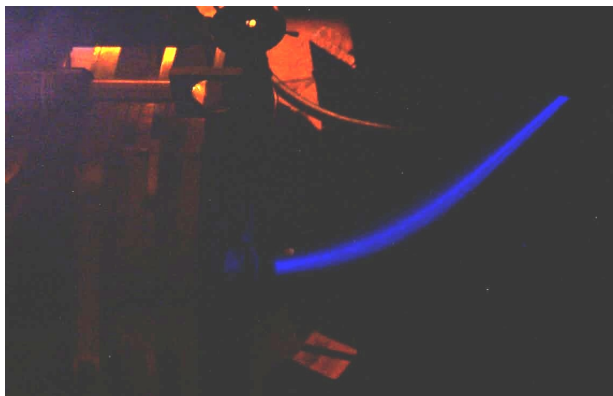


Figure 4.5.4-A4: 650 kV, 0.3 A, 0.15 ms, 29 J

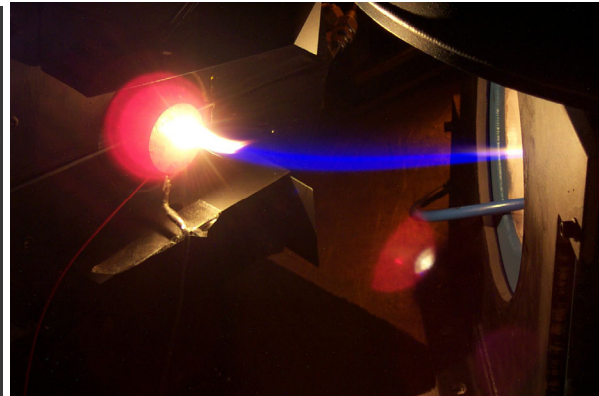


Figure 4.5.5-A4: 550 kV, 0.8 A, 1 ms, 440 J

It was later determined that an intermediate beam bending magnet was needed to direct the beam straight down the nozzle (that is, centered at both the exit and near the throat). Figure 4.5.6-A4 shows the intermediate magnets added. Figures 4.5.7-A4 through 4.5.9-A4 show

progressively more energy in the beam (higher powers and durations). The last two required neutral density filters on the camera to prevent overexposure. Carbon blow-off dust may be noted in these images. It may also be seen that some of the dust may be charged since it tends to follow the field lines back through the 5-Tesla magnet. Specks may also be observed in the camera's CCD that are caused by x rays from the beam. These photos also dramatically point out the need to carefully coordinate the beam and nozzle blowdown. Without thick, flowing blow-down air in the nozzle, the beam would immediately damage the nozzle walls.



Figure 4.5.6-A4: Bending magnet in gap.

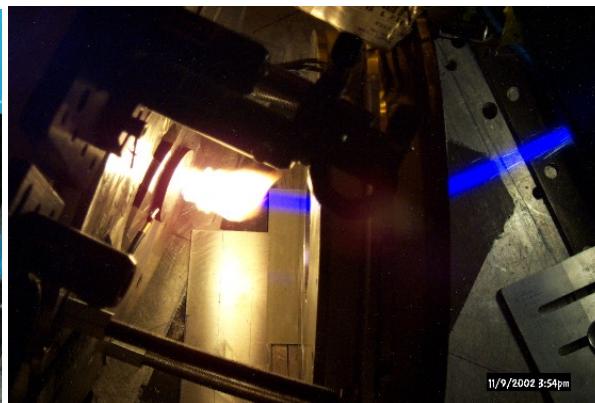


Figure 4.5.7-A4: 600 kV, 1.3 A, 0.5 ms, 390 J.

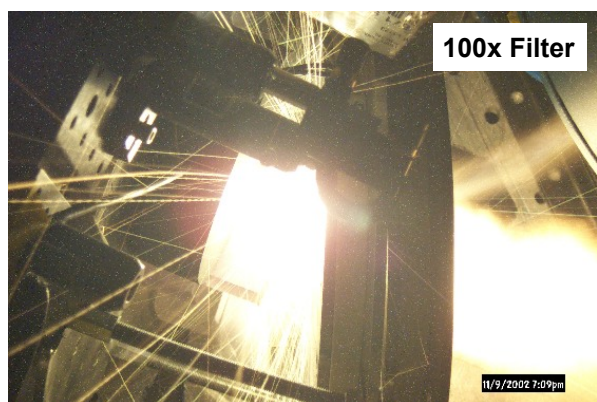


Figure 4.5.8-A4: 650 kV, 1.0 A, 3.0 ms, 1950 J.

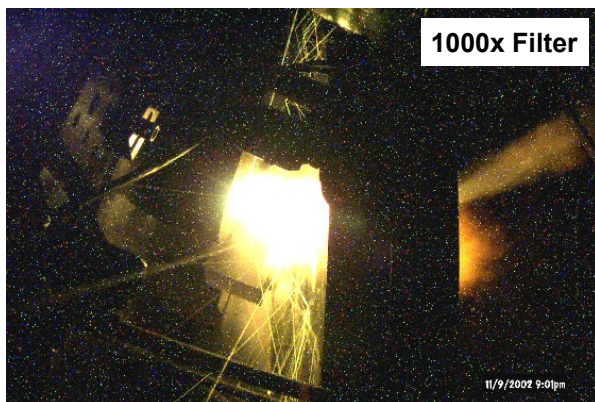


Figure 4.5.9-A4: 700 kV, 1 A, 3 ms, 2100 J.

At the higher energy levels, the beam left an impression in the graphite beam stop. Figure 4.5.10-A4 shows three samples; the beam stop was moved between shots. The beam is still annular at the nozzle exit. This is in contrast to the image on acetate shown previously with a very brief beam (Figure 4.5.2-A4). The longer duration beam apparently bores a hole in the air by heating it and thus reducing the scattering as it traverses to the nozzle exit. This effect should also be at work during blowdown except for the small portion of the path in which the beam is entering the flow field. The beam profile was not seen to be precisely reproducible. The reason for this is not known, but perhaps the beam was scraping the bottom of one of the apertures. Also shown in Figure 4.5.10-A4 are the results from another series of ten shots taken to demonstrate a broader sampling.

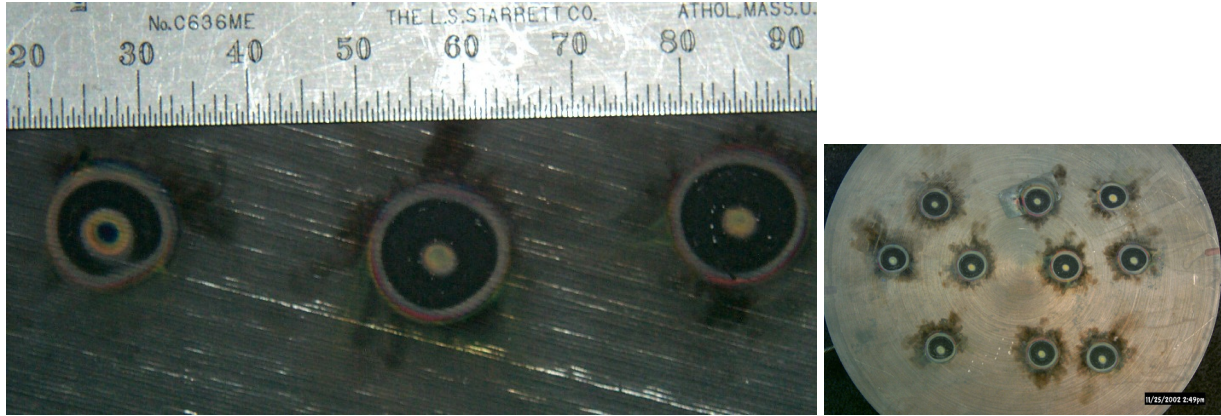


Figure 4.5.10-A4: Beam imprints left on graphite beam stop at nozzle exit.

The beam current incident on the carbon probe was measured through a 50-Ohm resistor to ground. Figure 4.5.11-A4 shows the cathode current and the beam current at the nozzle exit for four shots superimposed. The shots were very reproducible at the cathode. The scatter at the graphite probe may be due to the large amount of plasma a blow-off of the graphite during the shot, or to the beam scraping an aperture in the differential pumping system. The voltage of the beam at 1 ms has to be determined by calculation. The accelerator voltage drops by about 75 kV during the 3-ms long shot. After 1 ms, therefore, it drops around 25 kV. Hence the beam voltage at 1 ms is estimated to be $700 \text{ kV} + 12 \text{ kV}$ (drive voltage) $- 25 \text{ kV}$ (droop) $- 50 \text{ kOhm} \times 1.2 \text{ A} = 627 \text{ kV}$. (There was a 50-kOhm resistor between the HAWK bank and the cathode. This resistance was reduced to 11 kOhms before the main blow-down data was taken.) The beam power at the nozzle exit was, therefore, $627 \text{ kV} \times 1.2 \text{ A} = 752 \text{ kW}$. About 80 percent of the cathode current reached the nozzle exit. This is fairly consistent throughout the pulse. This may actually be about 85 percent if the backscattered electrons do not return to the graphite probe. The cathode current rise after 3 ms is an artifact of unfolding the Pearson probe data; the probe was later replaced with one that had less droop at this time scale.

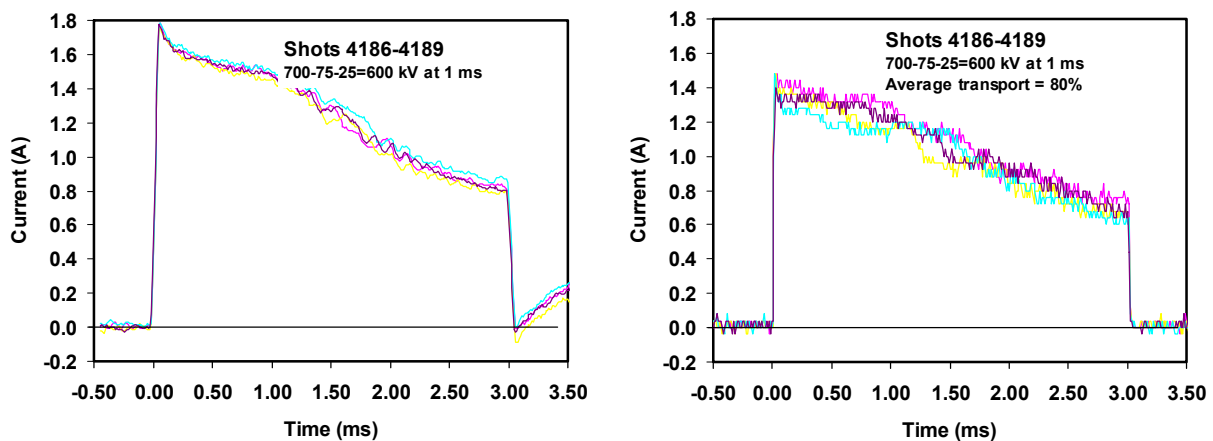


Figure 4.5.11-A4: Cathode current (left) and beam current at nozzle exit (right), 4 shots.

4.6 Beam Alignment into Nozzle

The beam next needed to be aligned accurately with the nozzle. The diagnostics used for this consisted of small acetate targets placed at various distances from the throat within the nozzle. Figure 4.6.1-A4 below shows a typical setup. Three mirrors were used to record simultaneously the beam exit inside the 5-Tesla magnet, the exit of the nozzle, and the acetate deep inside the nozzle. The figure shows the setup in room light, and it shows the beam images above. For this shot, the beam is a too far to the left in the nozzle. The paper clip seen in the photo is to indicate when the 5-Tesla magnet is on.

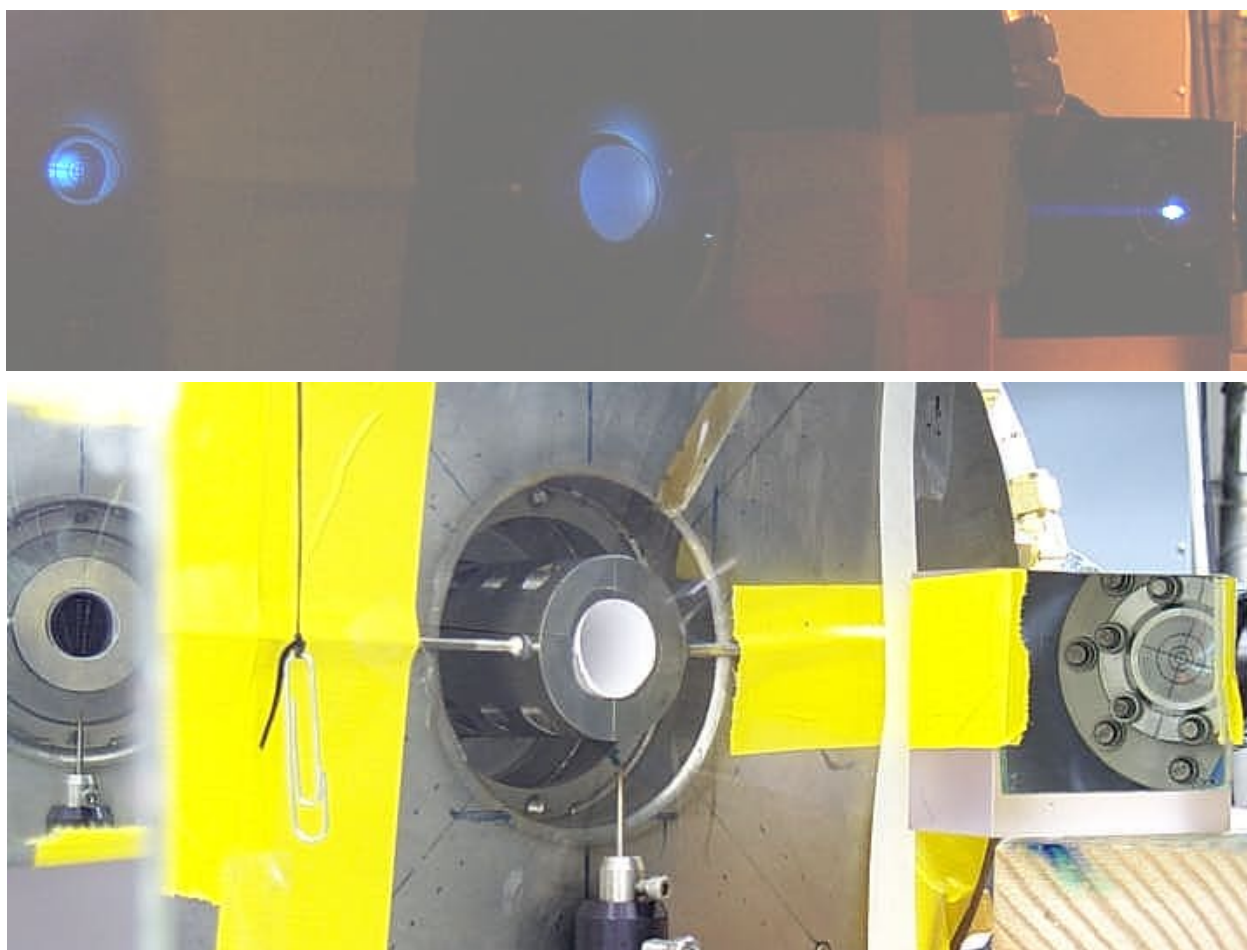


Figure 4.6.1-A4: Technique for diagnosing beam location. Lower image is via three mirrors in lab light; upper image is during the beam shot.

Initially, the superconducting magnet had been aimed directly at the exit of the nozzle based on early modeling. Experimental results, however, showed that the beam was canted going through the nozzle. As a consequence of that misalignment, the beam either hit the nozzle exit or was off to the far side near the throat. More detailed modeling using the MAZE 3D code

showed that the field line that went through the center of the differential pumping window magnets ended up on the far side of the nozzle centerline by a few mm (see Figure 4.6.2-A4). It was important to extend the calculation out to these magnets since that is the dominant constraint; the beam does not necessarily go through the center of the 5-Tesla magnet.

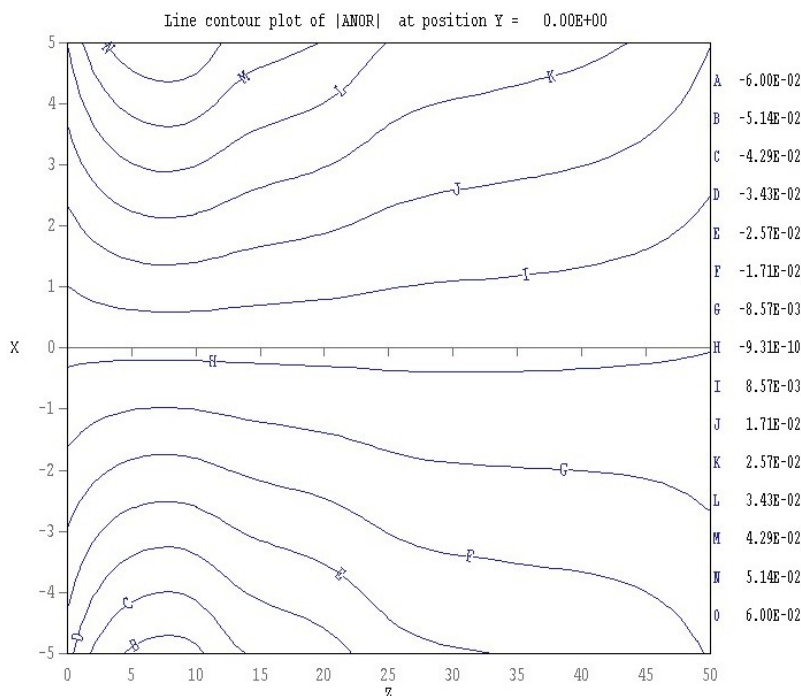


Figure 4.6.2-A4: Field lines in nozzle; “H” go through the center of the window magnets.

To remedy this, the nozzle and nozzle magnets were moved a negative 10 cm along the z axis (nozzle axis). In addition, two more thin steering magnets (mentioned above and shown earlier) were placed between the nozzle exit and the superconducting magnet. A 5-cm gap was maintained for airflow diagnostics. Finally, the turning magnets and the last two nozzle magnets were translated horizontally to fine-tune the beam position. After a few days of effort with this new configuration, the beam alignment was noticeably improved.

Several photographs were taken of the beam striking the thin acetate target inside the nozzle. The same camera setup was used for each of the shots shown below. The distance from the throat is listed below each beam photo in Figure 4.6.3-A4; $z = 0$ is the throat, $z = 52$ is the nozzle exit. The last photo has a scintillator at both $z = 22$ cm and $z = 52$ cm. The radii of the rings on the scintillator are 0.25 cm, 0.5 cm, and 1.0 cm. The beam diameter at $z = 12, 22, 32, 42$, and 52 cm is estimated to be 1.0, 1.6, 1.8, 1.7, 2.2 cm, respectively. The nozzle diameters at these locations are 1.8, 2.1, 2.2, 2.4, 2.6 cm, respectively. In this diagram, the beam is seen to be centered vertically within about 1 mm for the entire nozzle length. The horizontal positions of the beam at $z = 12, 22, 32, 42$, and 52 cm are estimated to be $-0.2, -0.2, -0.2, -0.2$, and $+0.3$ cm, respectively, where positive is in to the right as the beam propagates down the nozzle.

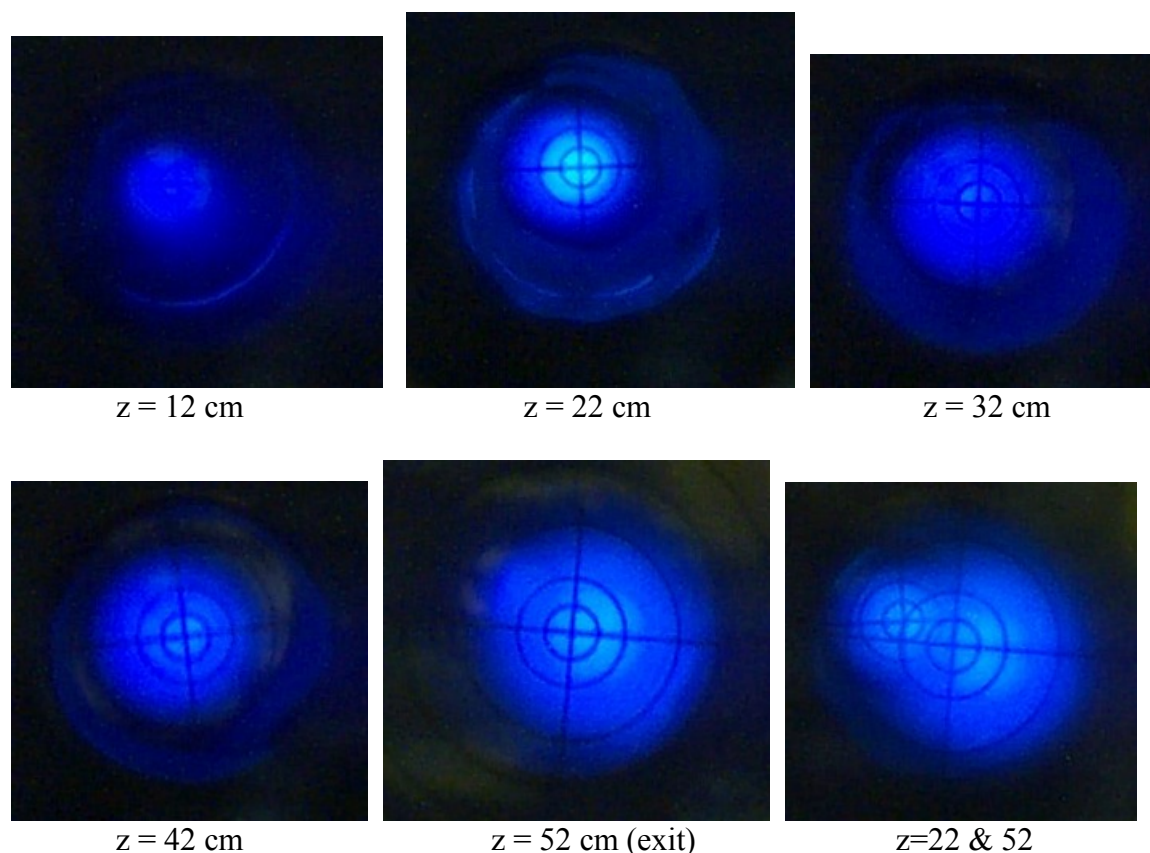


Figure 4.6.3-A4: Beam Shot Photos at Various Nozzle Locations.

During these alignment tests, the beam voltage was 600 kV but the same behavior is expected for voltages ranging from 500 kV to 700 kV. The superconducting magnet field strength was 4.5 T because it gave better alignment than 5.0 T. The beam intensity, moreover, appears fairly uniform radially for most cases.

4.7 Beam States during Blowdown and Data Acquisition

Data acquisition for a blowdown with e-beam injection was first accomplished with the Princeton team on December 15, 2002. A total of nine beam-heated blowdown shots were obtained with pressure data taken at five locations in the nozzle. The Mach number of the airflow at the nozzle exit was also measured using shadowgraphs during this initial data-taking phase. The nominal peak power level for this initial series was 714 kW at the accelerator exit (1-ms average) with an estimated 625 kW deposited into the air within the nozzle; the beam voltage was 600 kV and the duration was 1.5 ms. The longest shot was 6 ms but was accomplished with a lower power level. Steady state in the pressure sensors was obtained in about 1 ms. Table 4.7.1-A4 summarizes the shot parameters, and Figure 4.7.1-A4 shows the current at the cathode for the shots. The current entering the nozzle was estimated to be 80% of the current at the cathode. These initial blowdown data are not included in the primary (March) data set because the nozzle current-to-ground measurement was not functioning during the initial round of data collection. The exclusion of this initial data set is unfortunate because it was during this time

frame that the extracted beam current was seen to be most stable as determined by allowing the beam to impact the graphite probe. As the experiments progressed from this initial phase, the stability of the extracted current declined as an extensive series of maintenance tasks were performed on the HAWK. The first of these tasks was necessitated by an internal high voltage failure during the experimental run of December 15, 2002.

Table 4.7.1-A4: Summary of early (Dec 15, 2002) e-beam heated blowdown shots

Shot	4206	4207	4208	4209	4210	4211	4212	4213	4214
Date	12/15	12/15	12/15	12/15	12/16	12/16	12/16	12/16	12/17
Total duration (ms)	0.8	1	1	2	2	6	3	3	1.5
Accel (kV) at start	400	400	400	400	400	400	400	500	600
Injector (kV)	6.4	8	8	8	8	8	12	12	12
kV at Nozzle (1-ms ave)	397	392	387	387	382	388	381	484	586
Amps at Nozzle (1-ms ave)	0.41	0.53	0.92	0.92	0.65	0.85	1.50	1.26	1.23
kW at Nozzle (1-ms ave)	129	166	284	285	200	265	458	609	721

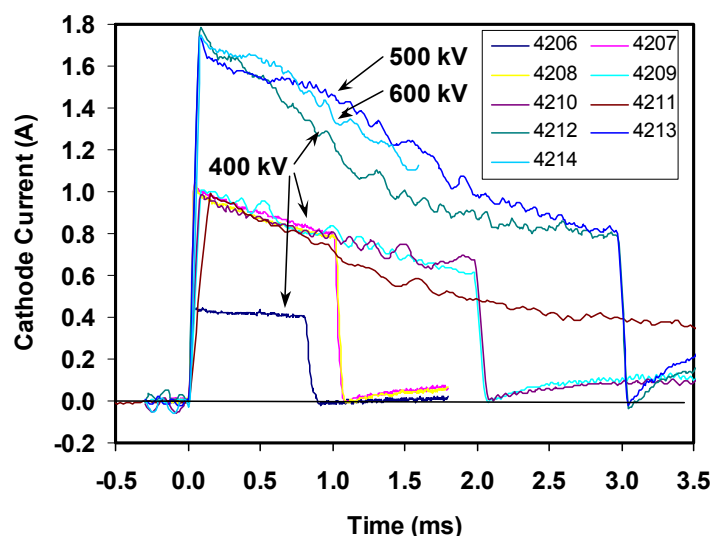


Figure 4.7.1-A4: Cathode current for the early (Dec 15, 2002) e-beam heated blowdown shots.

The HAWK accelerator was disassembled after the Dec 15 failure and extensive damage to components on the high voltage deck were diagnosed and repaired. The damage included failed integrated circuits and electronic components on the gun-filament and trigger boards. In addition, collateral damage to a 600-volt supply circuit was repaired. The circuit supplied the voltage to the trigger board and the suppression/acceleration voltage to one stage of the tetrode. After troubleshooting and replacing the failed components, current extraction from the cathode was tested with a 7 kV potential from the cathode to the grid to obtain approximately 1.7 Amps. The HAWK high voltage deck was reassembled to begin long pulse tests of the cathode current under magnetic field conditions.

The original current monitor on the cathode line on the HV deck was a Pearson 2100 with 80% droop per millisecond. During the January 2003 repair process, it was replaced with a

Pearson 110. The replacement was made because, even though the new unit had a lower voltage response it was better suited for multi-millisecond pulses because it had only 0.8% droop per millisecond.

While the accelerator was opened, several tests were performed to determine whether the current sag during the multi-millisecond shots could be reduced. It was determined that the injector could be fired with voltage on the anode (“injector voltage”) and that a full current pulse would be obtained for some combinations of cathode (“drive”) voltage if the anode was shorted to the tank via the HAWK crowbar to provide a return current path for the beam current. Up to then, the system had been operating without voltage applied to the grid-anode gap because of pressure spikes observed in early testing stages. However, these spikes were reduced to an acceptable level by the time of this maintenance work. It is possible that the anode region had outgassed and been cleaned by the numerous beam shots.

This was also the time that the HV deck tetrode was moved to a location farther from the center of the HAWK magnet. It appeared to help in the current droop also, but there is some uncertainty about this. It was also noted that the HAWK seemed to be more tolerant of voltage breakdown since the move. There were, subsequently, about 5 major breakdowns (during conditioning, etc.) without loss of the HAWK electronics.

A beam was extracted through the differential pumping system and onto a graphite current collector using the new internal configuration. Figure 4.7.2-A4 shows some results of that extraction. Without an applied injector voltage, the beam current sags strongly with time. But with it, the current is fairly constant over 5 ms, but less total current is delivered in the first millisecond of operation. The reason for this is not known.

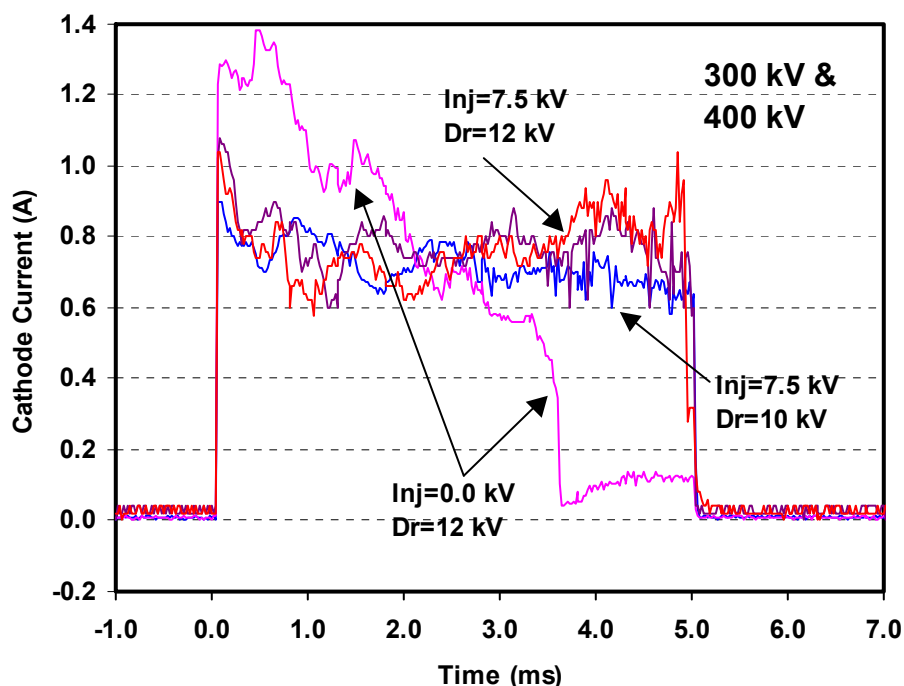


Figure 4.7.2-A4: Beam current at graphite collector located outside accelerator.

After completing the repair to the accelerator as outlined above, there was subsequently a problem with noise pickup that caused the accelerator to break down during the first shot. Fortunately, the HAWK HV-deck electronics survived this incident. The noise appeared to be caused by a 6-MHz current pulse on the wires leading to the nozzle magnets.

In response to the noise problem, a different firing protocol was developed and produced three successful beam-heated blowdown shots. Table 4.7.2-A4 summarizes the shot conditions. The current was not directly measured at the accelerator exit, but it is thought that there was little droop, based on Figure 4.7.2-A4 described above. With that assumption, the powers for these shots are estimated in the table. The power droop, moreover, appeared to be much less than in previous data shots (December). The Optran pressure transducer data supported this conclusion. For example, the Optran pressures in shot 4231 look quite stable for 2.0 ms and then slowly decline for the next millisecond (see Figure 4.7.3-A4). Hence there was, at this point in the experiment, empirical evidence that the repairs described above had been effective.

Table 4.7.2-A4: Summary of three sequential blowdown shots

Shot	4229	4230	4231
Duration	1 ms	1 ms	3 ms
Injector voltage	9.5 kV	9.5 kV	9.5 kV
Drive voltage	7.0 kV	7.0 kV	7.0 kV
Initial beam voltage	416 kV	526 kV	530 kV
Final beam voltage	About 382 kV	492 kV	444 kV
Estimated beam current	0.8 A	0.8 A	0.8 A
Initial power at nozzle	333 kW	421 kW	424 kW
Final power at nozzle	306 kW	394 kW	355 kW

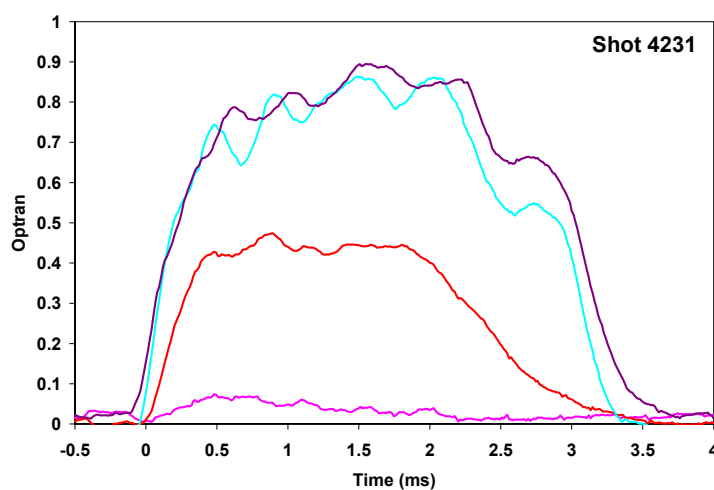


Figure 4.7.3-A4: Optran data (arbitrary units) for shot 4231.

To complete the repairs from the previous trigger problems that caused damage to the high voltage deck electronics, the HAWK accelerator was next conditioned to 737 kV, with the

high voltage capacitor bank attached. Several accelerator shots were then fired. The shots focused on beam transport and testing exit current monitors that could be utilized concurrently with the cathode current monitor. It was anticipated that the monitor might help to determine accurately the percentage of the cathode current delivered to the nozzle air on a shot-to-shot basis. Figure 4.7.4-A4 shows two of the monitors that were tested. Unfortunately, the monitors that were tested all vibrated in the presence of the 5-Tesla field during blowdown, giving erroneous signals that were difficult to interpret. However, the Princeton team was eventually able to obtain measurements of current going into the nozzle wall by using a current viewing resistor from the electrically floating nozzle to ground.

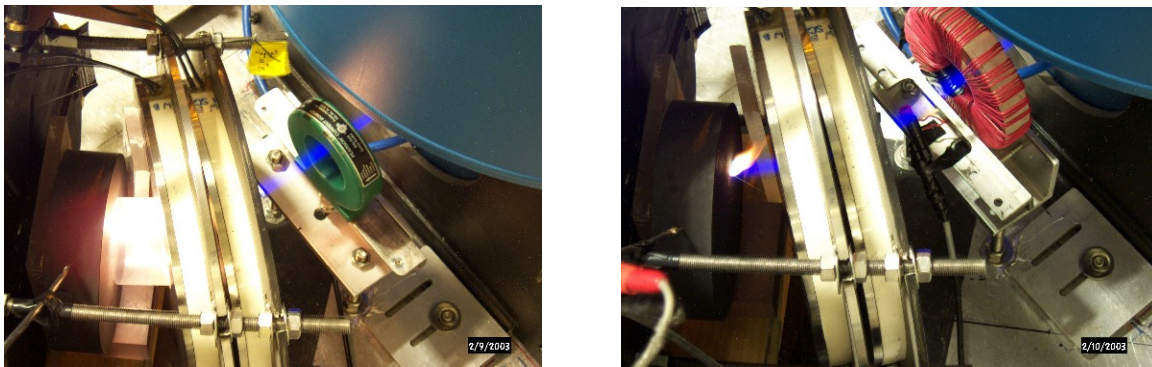


Figure 4.7.4-A4: Beam Exit Current Monitors.

At this late stage in the experiment (Feb 2003) the cause for much of the breakdown difficulties was discovered. The accelerator began breaking down intermittently during shots with an elevated charge current. This eventually led to a filament heater control failure caused by a high voltage breakdown. The HAWK accelerator was disassembled and components on the high voltage deck were diagnosed and repaired. In addition, severe tracking of the Lexan capacitor bank support between stages 4 and 5 was discovered along with lead shavings throughout the accelerator cavity. Leaking bearing grease from the HV deck motor drive allowed the filings to adhere to the tank wall and the Lexan support. The intermittent breakdowns and elevated charge currents observed when charging the accelerator were due to the surface flashing of the Lexan insulator support. The lead attached to the Lexan support degraded the voltage hold-off rating of the insulator. The lead shavings were the result of movement of the anchor plate when HAWK magnets 2 and 3 were fired. This movement broke a fastener that secured one of the lead weights that tension the charging chains. Repeated firing of the magnets shaved lead from the lead weight assemblies by allowing them to swing into bolts on the anchor plate assembly. Aluminum plates were installed on the anchor plate assembly to prevent it from sliding forward when the magnets were fired, but this caused the charging chains to sag when rotating and short out the charging process. Hence the lead weights that tension the charging chain were reinstalled but Lucite shields were installed between the weights and the ground plate frame to minimize their movement during magnet shots and mitigate shaving lead that could coat the accelerator. The machine was then reassembled and reconditioned to 979 kV without that HV capacitor bank attached and to 875 kV with the HV bank attached.

Upon trying to fire a shot, it was discovered that the cathode heater was completely non-functional. The accelerator was again disassembled and a blown fuse and a blown integrated circuit on the gun-filament board were repaired. The machine was reassembled and conditioned to 620 kV without the HV capacitor bank attached. Beam shots were then fired to verify proper beam transport but data obtained indicated that only half of the annular beam was being delivered to the nozzle exit. Low current, short duration and high current, long duration shots dumped into a graphite probe indicated that the beam loss was most likely due to the beam scraping an aperture in the differential pumping system. Three sections of the system were opened and inspected to determine the point at which the beam was scraping. The point identified was on an aperture that suggested that the fast valve magnet was misaligned. The molten metal fragments were cleaned, the system was reassembled and low current, short duration beam shots were fired to realign the beam through the pinch valve and into the nozzle.

It was after this sequence of events that the primary March data set was taken. During this data set it was noted that the beam current appeared to be unstable. It was suspected that this might be due to the beam scraping the wall of the differential pumping system apertures. Misalignment might have occurred during the numerous repair activities described above.

4.8 Beam Conditions for the Primary Data Set (March 2003)

The primary data was taken during March 2003. Table 4.8.1-A4 summarizes the beam conditions for those shots. There were over 70 shots taken that could be analyzed. The current deposited in the nozzle was monitored for these shots using the Princeton current to ground diagnostic. This current is not necessarily caused directly by beam electrons, but is more likely secondary electrons pushed to the wall by the beam charge. It is believed to be a fairly accurate measure of the beam current entering the nozzle, because charge must be conserved. The nozzle current, as it was called, was fairly unstable for many of the shots. Some of these shots, however, reached a steady state in current for about 1- 3 ms. Hence a set of shots where the nozzle current was relatively stable for over 2.5 ms is listed in Table 4.8.2-A4. Plots of the parameter space for the total campaign and the 2.5-ms-stable shots are shown in Figure 4.8.1-A4.

It should be noted that the primary data set, taken during March, was taken when the extracted current - as measured with the carbon probe - was much less stable than it was in November 2002 or February 2003.

Table 4.8.1-A4: Summary of beam conditions for the blowdown shots of March 2003

	Date	Approx Time	Princeton Shot No.	Hawk Shot No.	Plenum Pressure (psi)	Plenum Temp (K)	Beam Voltage at Nozzle Exit at 1.5 ms (kV)	Beam Voltage at Nozzle Exit at 1.5 ms (kV)	Beam Current at Nozzle Exit at Start (kV)	Beam Current at Nozzle Exit at 1.5 ms (kV)	1.5-ms Ave Power into Nozzle (kW)	Total shot Duration (ms)	Operational Pressure Sensors	Nozzle Current	Beam Exit Photodiode	Shadowgraph	Rayleigh	NO Absorption	Spark Vel	+/- 12% for >2.5 ms?
1	3/1/03	15:52	676	4286	2375	~605	503	431	1.20	1.10	537	2.0	Y	N	N			N		
2	3/1/03	16:41	677	4287	2375	~605	507	448	1.50	1.30	669	2.0	Y	N	N			N		
3	3/1/03	17:41	678	4288	2480	~605	505	456	1.42	1.32	658	5.0	Y	Y	N			N		Y
4	3/1/03	18:22	679	4289	2380	~605			?				Y	Y	N			N		
5	3/1/03	18:46	680	4290	2480	~605	505	456	1.40	1.23	632	5.0	Y	Y	N			N		
6	3/1/03	19:17	681	4291	2700	~605	507	462	1.00	1.00	485	6.5	Y	Y	N			N		
7	3/1/03	19:48	682	4292	2450	~605	507	462	1.55	1.40	715	6.5	Y	Y	N			N		
8	3/1/03	20:20		4293		~605	508	452	1.60	1.50	744	3.0	Y	Y	N			N		Y
9	3/2/03	10:54	683	4294	2450	~605	505	461	1.70	1.50	773	6.5	Y	Y	N	N	Y	N		Y
10	3/2/03	11:39	684	4295	2475	~605	510	465	1.45	1.33	678	6.5	Y	Y	N	N	Y	N		Y
11	3/2/03	12:18	685	4296	2550	~605	511	464	1.30	1.20	609	6.5	Y	Y	N	N	Y	N		
12	3/2/03	15:51	686	4297	2530	~605	608	549	1.60	1.40	868	2.0	Y	Y	N	N	Y	N		
13	3/2/03	16:29	687	4298	2550	~605	603	552	1.55	1.30	823	4.0	Y	Y	N			N		
14	3/2/03	20:06	688	4300	2600	~605	712	643	1.20	1.00	745	1.0	Y	Y	N	N	Y	N		
15	3/2/03	20:45	689	4301	2650	~605	757	689	0.3?	1.10		2.0	Y	Y	N	N	Y	N		
16	3/2/03	21:36	690	4302	2390	~605	708	645	1.70	0.40	710	4.0	Y	Y	N	N	Y	N		
17	3/4/03	16:27	691	4306	2490	~605	606	540	1.80	1.30	888	2.0	Y	Y	N	Y	N	N		
18	3/4/03	21:02	695	4307	2510	~605	605	545	1.50	0.70	633	3.0	Y	Y	N	Y	N	N		
19	3/4/03	21:52	696	4308	2160	~605	605	542	1.50	1.00	717	2.0	Y	Y	N	Y	N	N		
20	3/4/03	22:21	697	4309	2160	~605	607	546	1.50	1.00	721	2.0	Y	Y	N	Y	N	N		
21	3/6/03	19:04	698	4310	2000	~605	607	566	1.30	0.60	557	4.0	Y	Y	N	Y	N	N		
22	3/6/03	19:45	699	4311	2280	~605	608	565	1.20	0.80	587	4.0	Y	Y	N	Y	N	N		
23	3/6/03	20:16	700	4312	2600	~605	617	572	1.10	0.70	535	4.0	Y	Y	N	Y	N	N		
24	3/6/03	21:03	701	4313	1960	~605	612	571	1.10	0.40	444	4.0	Y	Y	N	Y	N	N		
25	3/6/03	21:36	702	4314	2000	~605	617	572	1.20	0.20	416	6.0	Y	Y	N	Y	N	N		
26	3/6/03	22:08	703	4315	2050	~605	617	575	0.75	0.70	432	6.0	Y	Y	N	Y	N	N		Y
27	3/6/03	22:46	704	4316	2150	~605	616	578	0.60	0.60	358	6.9	Y	Y	N	Y	N	N		
28	3/6/03	23:18	705	4317	2375	~605	617	606	0.20	0.20	122	6.9	Y	Y	N	Y	N	N		
29	3/9/03	19:57	706	4318	2500	~605	607	552	1.60	0.80	695	3.0	Y	Y	N	Y	N	N		
30	3/11/03	14:51	710	4319	2050	~605	610	565	1.10	0.79	555	1.2	Y	Y	N	Y	N	Y		
31	3/11/03	15:52	711	4320		~605	606	20				0.2	Breakd	Y	N	Y	N	Y		
32	3/11/03	18:43	712	4321	2050	~605	615	577	0.90	0.75	492	1.2		Y	N	Y	N	Y		

Table 4.8.1-A-4: Summary of beam conditions for the blowdown shots of March 2003 (continued)

	Date	Approx Time	Princeton Shot No.	Hawk Shot No.	Plenum Pressure (psi)	Plenum Temp (K)	Beam Voltage at Nozzle Exit (kV)	Beam Voltage at Nozzle Exit (kV)	Beam Current at Nozzle Exit (kV)	Beam Current at Nozzle Exit (kV)	Beam Current at Nozzle Exit (kV)	1.5-ms Ave Power into Nozzle (kW)	Total shot Duration (ms)	Operating Pressure Sensors	Nozzle Current	Beam Exit Photodiode	Shadowgraph	Rayleigh	NO Absorption	Spark Vel	+/- 12% for >2.5 ms?
33	3/11/03	20:12	713	4322	1900	~605	608	465	0.60	0.60	0.60	322	0.4	Breakdown	Y	N	Y	N	Y		
34	3/13/03	12:58	714	4325		~605	576	550	0.70	0.60	0.60	366	1.2	Y	Y	Y	Y	N	Y		
35	3/13/03	14:15	715	4326	1990	~605	571	543	0.74	0.72	0.72	407	1.2	Y	Y	Y	Y	N	Y		
36	3/13/03	15:03	716	4327	2025	~605	572	547	0.70	0.48	0.30	330	1.2	Y	Y	Y	Y	N	Y		
37	3/13/03	15:55	717	4328	1975	~605	570	548	0.60	0.24	0.24	235	1.2	Y	Y	Y	Y	N	Y		
38	3/13/03	16:48	718	4329	2175	~605	573	533	1.28	0.72	0.72	553	1.2	Y	Y	Y	Y	N	Y		
39	3/13/03	18:29	719	4330	2250	~605	572	550	1.40	1.00	1.00	673	0.5	Y	Y	Y	Y	N	Y		
40	3/13/03	19:57	720	4331	2175	~605	573	552	1.55	1.20	1.20	773	0.5	Y	Y	Y	Y	N	Y		
41	3/17/03	9:14	721	4351	2250	~605	511	462	1.74	1.25	1.25	727	1.2	Y	Y	Y	Y	N	Y		
42	3/17/03	10:27	722	4352	2250	~605								Y	Y	Y	Y	N	Y		
43	3/17/03	11:31	723	4353	2150	~605	564	537	1.45	1.50	1.50	812	0.5	Y	Y	Y	Y	N	Y		
44	3/17/03	12:14	724	4354	2150	~605	558	548	1.74	1.25	1.25	827	0.3	Y	Y	Y	Y	N	Y		
45	3/17/03	13:15	725	4355	2225	~605	560	527	1.74	1.25	1.25	813	0.3	Y	Y	Y	Y	N	Y		
46	3/17/03	13:57	726	4356	2175	~605								Y	Y	Y	Y	N	Y		
47	3/17/03	14:33	727	4357	2175	~605	564	527	1.39	1.10	1.10	679	0.8	Y	Y	Y	Y	N	Y		
48	3/17/03	15:39	728	4358	2175	~605	558	505	1.66	1.40	1.40	813	1.2	Y	Y	Y	Y	N	Y		
49	3/17/03	16:50	729	4359	2125	~605	559	506	1.60	1.20	1.20	746	1.2	Y	Y	Y	Y	N	Y		
50	3/17/03	17:50	730	4360	2100	~605	559	473	1.60	1.20	1.20	722	1.2	Y	Y	Y	Y	N	Y		
51	3/17/03	18:52	731	4361	2100	~605	565	504	1.25	1.25	1.25	668	4.0	Y	Y	Y	Y	N	Y		Y?
52	3/17/03	19:48	732	4362	2250	~605	566	519	1.00	1.00	1.00	543	6.9	Y	Y	Y	Y	N	Y		Y?
53	3/18/03	17:31	735	4363	2175	~605	593	568	0.60	0.60	0.60	348	3.0	Y	Y	Y	N	N	Y	Y	
54	3/18/03	18:37	737	4364	2300	~605	592	566	0.60	0.60	0.60	347	3.0	Y	Y	Y	N	N	Y	Y	Y
55	3/18/03	19:29	738	4365	2500	~605	592	563	0.60	0.60	0.60	347	3.0	Y	Y	Y	N	N	Y	Y	Y
56	3/18/03	20:39	739	4366	2350	~605	597	568	0.60	0.60	0.60	350	3.0	Y	Y	Y	N	N	Y	Y	Y
57	3/19/03	16:20	742	4367	2430	~605	595	568	0.72	0.53	0.53	363	3.0	Y	Y	Y	N	N	Y	Y	
58	3/19/03	17:00	743	4368	2110	~605	596	568	0.40	0.40	0.40	233	3.0	Y	Y	Y	N	N	Y	Y	
59	3/19/03	17:45	744	4369	2130	~605	593	656	0.65	0.50	0.50	359	3.0	Y	Y	Y	N	N	Y	Y	
60	3/19/03	18:43	745	4370	2150	~605	596	584	0.40	0.56	0.56	283	6.9	Y	Y	Y	N	N	Y	Y	
61	3/19/03	19:30	746	4371	2110	~605	603	576	0.60	0.60	0.60	354	6.9	Y	Y	Y	N	N	Y	Y	Y
62	3/26/03	17:45	747	4378	2140	~605	597	568	0.70	0.55	0.55	364	3.0	Y	Y	Y	N	N	Y	N	
63	3/26/03	19:30	748	4379	2110	~605	599	568	0.60	0.60	0.60	350	3.0	Y	Y	Y	N	N	Y	N	Y
64	3/28/03	14:14	749	4393	2150	~605	602	575	0.40	0.60	0.60	294	6.0	Y	Y	Y	N	Y	N	N	
65	3/28/03	16:02	751	4394	2200	~605	602	575	0.60	0.50	0.50	324	6.0	Y	Y	Y	N	Y	N	N	Y
66	3/28/03	19:40	752	4395	2150	~605	602	575	0.60	0.60	0.60	353	6.0	Y	Y	Y	N	Y	N	N	Y?
67	3/28/03	20:57	753	4396	2120	~605	602	575	0.60	0.60	0.60	353	6.0	Y	Y	Y	N	Y	N	N	Y
68	3/28/03	22:05	755	4397	2275	~605	601	574	0.50	0.50	0.50	294	6.0	Y	Y	Y	N	Y	N	N	Y?
69	3/29/03	15:08	756	4404	2140	~605	604	556	0.30	0.40	0.40	203	6.0	Y	Y	Y	N	Y	N	N	Y
70	3/29/03	15:42	757	4405	2275	~605	509	482	0.50	0.50	0.50	248	6.0	Y	Y	Y	N	N	Y	N	Y
71	3/29/03	16:20	758	4406	2275	~605	502	456	1.50	1.00	1.00	599	6.0	Y	Y	Y	N	N	N	N	Y
72	3/29/03	17:01	759	4407	2190	~605	556	510	1.30	1.10	1.10	640	6.0	Y	Y	Y	N	N	N	N	
73	3/29/03	17:43	760	4408	2060	~605	601	555	1.00	1.00	1.00	578	6.0	Y	Y	Y	N	N	N	N	

Table 4.8.2-A4: Summary of shots with relatively stable current in the nozzle for March 2003

	Date	Approx Time	Princeton Shot No.	Hawk Shot No.	Plenum Pressure (psi)	Plenum Temp (K)	Beam Voltage at Nozzle Exit Start (kV)	Beam Voltage at Nozzle Exit 1.5 ms (kV)	Beam Current at Nozzle Exit Start (kV)	Beam Current at Nozzle Exit 1.5 ms (kV)	1.5-ms Average Power into Nozzle (kW)	Total shot Duration (ms)	Operating Pressure Sensors	Nozzle Current	Beam Exit Photodiode	Shadowgraph	Rayleigh	NO Absorption	Spark Vel	+/- 12% for >2.5 ms?
1	3/1/03	17:41	678	4288	2480	~605	505	456	1.42	1.32	658	5.0	Y	Y	N			N		Y
2	3/2/03	10:54	683	4294	2450	~605	505	461	1.70	1.50	773	6.5	Y	Y	N	N	Y	N		Y
3	3/2/03	11:39	684	4295	2475	~605	510	465	1.45	1.33	678	6.5	Y	Y	N	N	Y	N		Y
4	3/6/03	22:08	703	4315	2050	~605	617	575	0.75	0.70	432	6.0	Y	Y	N	Y	N	N		Y
5	3/17/03	18:52	731	4361	2100	~605	565	504	1.25	1.25	668	4.0	Y	Y	Y	Y	N	Y		Y?
6	3/17/03	19:48	732	4362	2250	~605	566	519	1.00	1.00	543	6.9	Y	Y	Y	Y	N	Y		Y?
7	3/18/03	18:37	737	4364	2300	~605	592	566	0.60	0.60	347	3.0	Y	Y	Y	N	N	Y	Y	Y
8	3/18/03	19:29	738	4365	2500	~605	592	563	0.60	0.60	347	3.0	Y	Y	Y	N	N	Y	Y	Y
9	3/18/03	20:39	739	4366	2350	~605	597	568	0.60	0.60	350	3.0	Y	Y	Y	N	N	Y	Y	Y
10	3/19/03	19:30	746	4371	2110	~605	603	576	0.60	0.60	354	6.9	Y	Y	Y	N	N	Y	Y	Y
11	3/26/03	19:30	748	4379	2110	~605	599	568	0.60	0.60	350	3.0	Y	Y	Y	N	N	N		Y
12	3/28/03	16:02	751	4394	2200	~605	602	575	0.60	0.50	324	6.0	Y	Y	Y	N	Y	N	N	Y
13	3/28/03	19:40	752	4395	2150	~605	602	575	0.60	0.60	353	6.0	Y	Y	Y	N	Y	N	N	Y?
14	3/28/03	20:57	753	4396	2120	~605	602	575	0.60	0.60	353	6.0	Y	Y	Y	N	Y	N	N	Y
15	3/28/03	22:05	755	4397	2275	~605	601	574	0.50	0.50	294	6.0	Y	Y	Y	N	Y	N	N	Y?
16	3/29/03	15:08	756	4404	2140	~605	604	556	0.30	0.40	203	6.0	Y	Y	Y	N	Y	N	N	Y
17	3/29/03	15:42	757	4405	2275	~605	509	482	0.50	0.50	248	6.0	Y	Y	Y	N	N	N	N	Y
18	3/29/03	16:20	758	4406	2275	~605	502	456	1.50	1.00	599	6.0	Y	Y	Y	N	N	N	N	Y

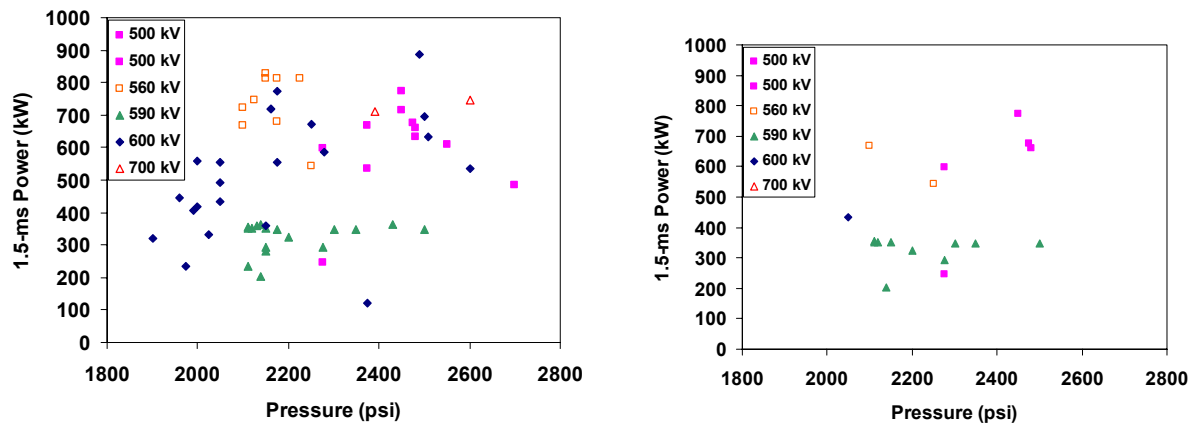


Figure 4.8.1-A4: Plot of beam conditions for the March blowdown set. The second figure displays the subset of shots that had reasonably constant current for the first 1 – 3 ms of injection.

The cause of the nozzle current fluctuations was investigated. A makeshift x-ray camera was constructed using a photomultiplier tube placed in a lead camera and covered with aluminum foil and black tape. The camera had a narrow window so the tube could only view the beam as it went around the 45° bend. Various tests were performed to assure that the camera was detecting x-rays produced by the beam in air. Figure 4.8.2-A4 shows the setup.



Figure 4.8.2-A4: Setup with PMT x-ray detector.

Figures 4.8.3-A4 and 4.8.4-A4 show the results for the beam impacting graphite and during blowdown. The correlation between the x-rays and the graphite current suggests that the x-ray detector is a good indication of beam current. The variations with graphite present suggests that the current oscillations are due to beam fluctuations before the beam exits the accelerator, possibly due to scrape off on apertures in the differential pumping system. The blowdown shot shows the same correlation between x-rays and nozzle current. This suggests that the nozzle current oscillations are not due to an inherent instability in the air, but rather are due to beam fluctuations before the beam exits the accelerator. Indeed, with such an unstable driving force, the fact that the nozzle air pressure does not respond with growing oscillations (as indicated by Optrand data) suggests that the beam-air interaction is intrinsically stable.

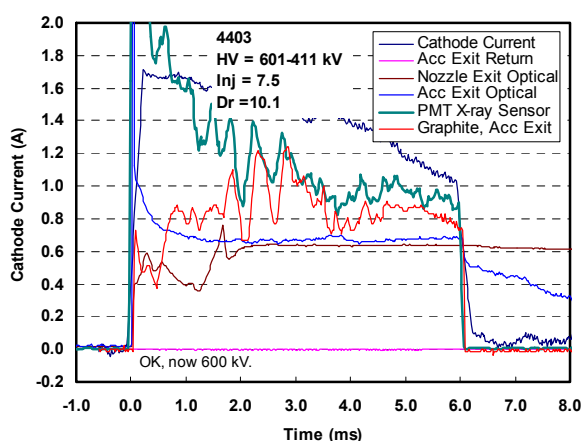


Figure 4.8.2-A4: Beam into graphite.

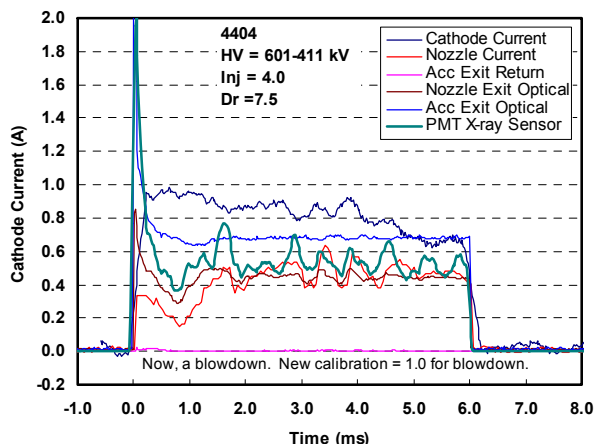


Figure 4.8.3-A4: Beam into blowdown.

The apertures in the differential pumping system were enlarged after the March campaign and one shot was taken. The results are shown in Figure 4.8.4-A4. It may be seen that the extracted beam looks more stable, but the current is low and the duration is short. Unfortunately, the experiment was terminated before a longer shot could be taken.

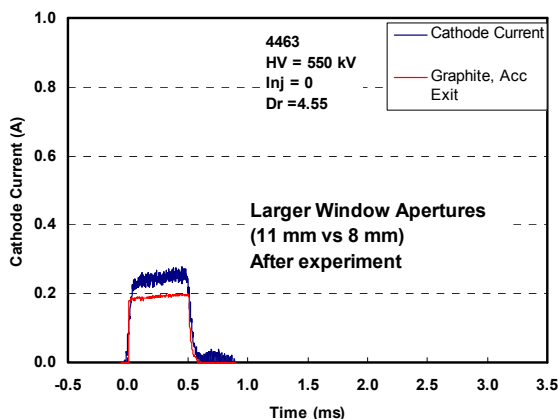


Figure 4.8.4-A4: Beam shot into graphite after enlarging the differential pumping system apertures.

4.9 Summary

Numerous modifications were made to the HAWK accelerator system:

- Addition of nine pulsed magnets and one superconducting magnet to guide the beam
- Modification of internal electronics to better tolerate the applied magnetic field
- Modifications to immobilize the internal hardware in the applied magnetic field
- Development of differential pumping, fast valve, and timing systems
- Addition of a 5-Tesla superconducting magnet to guide the beam around a 45° bend
- Increase in the size of the main capacitor bank so as to increase beam power and duration
- Addition of a “jet deflector” to cool the exiting nozzle air and deflect it upward
- Upgrade of the control electronics to enable easier operation

As a result of these modifications, the system was able to deliver up to 1 MW of beam for several milliseconds into the nozzle after a 45° bend through air. Unfortunately, scraping of the beam on aperture walls (or some other reason) caused the beam to be unstable for many of the blowdown shots. However, more than seventy useful blowdown shots were achieved.

APPENDIX A5: The Diagnostics Employed

Plenum Pressure and Temperature

The plenum pressure was routinely measured using a standard Omega PX303-5KA5V pressure transducer. The plenum temperature was measured by two independent thermocouples. The primary temperature measurement was supplied by a J type thermocouple employing an update period of 5 ms. A K type thermocouple having an update period of 0.5 sec was employed as a back-up. Examples of plenum pressure and temperature data are shown in Figs 1.2 of this report as well as Figs 1-A5 and 2-A5 below.

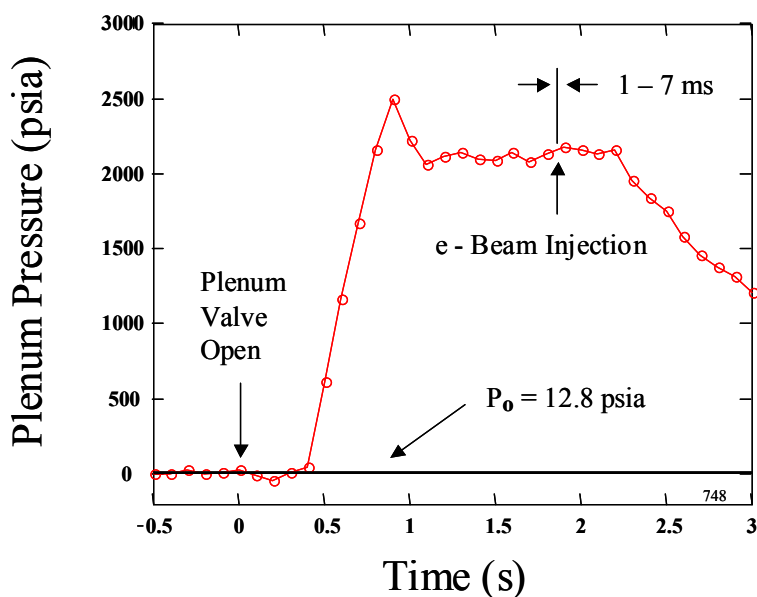


Figure 1-A5: A typical plenum pressure measurement taken at a 10-Hz data rate. Also shown is the timing and duration of e-beam injection.

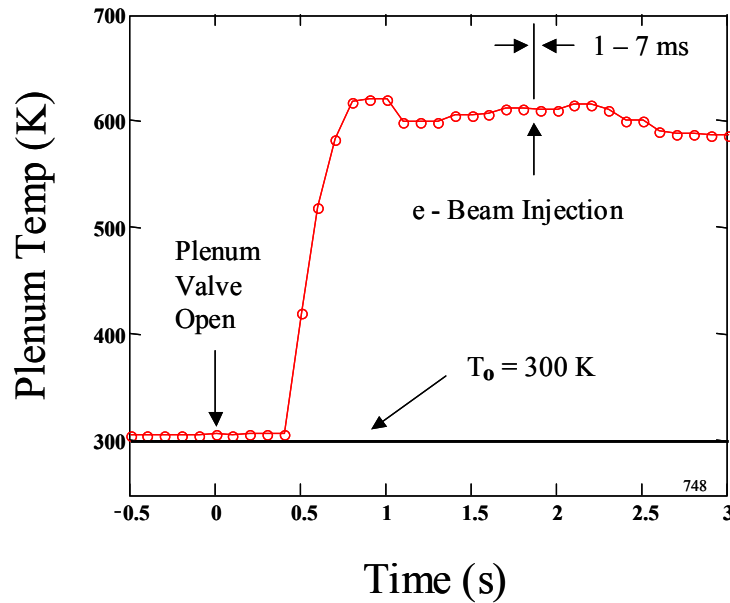


Figure 2-A5: A Typical plenum temperature measurement taken at a 10-Hz rate.

Nozzle Pressure: Fast and Slow Data

Nozzle pressure measurements using Optrand pressure-to-voltage transducers were taken on every blowdown with or without e-beam heating. These optically based transducers were introduced into the nozzle at five evenly spaced locations through small holes in the cooling plates separating the solenoid magnets (see Fig 2-A1 and Table 1-A1). The transducers were modified at the factory to accommodate the 1 MW experiments. Interference filters were introduced in front of the optical detectors internal to each unit. These filters effectively minimized X-ray scintillation noise generated in the transducers' internal fiber-optic cables when HAWK was fired. Pressure data were taken in both slow data rate (10 Hz) and fast data rate (75 kHz) modes. The slow data taken with these transducers allowed for a measurement of the slowly changing nozzle pressure in the absence of e-beam injection. The 15 ms-wide fast data window was routinely positioned so as to capture the transient change in the nozzle pressure resulting from e-beam injection. Examples of fast nozzle pressure measurements are shown in Figs 7.4, 7.6, 7.10 and 7.13 of this report.

A fundamental problem was encountered with the slow data from these transducers when the hot air from a blowdown was introduced into the nozzle. The baseline voltage of the measurement was found to drift downward as the measuring elements rose in temperature. This downward drift was observed to be as much as 40 percent of the increase in voltage produced by the high-pressure air. The thermal drift was largest for the transducer nearest the nozzle throat because that section of the nozzle experienced the largest temperature excursion during a blowdown (See Fig 3-A5 and 4-A5 below). Hence, the slow pressure data had to be corrected for

this drift. The fast data did not suffer from this problem because essentially no change in nozzle temperature occurred over the 15 ms duration of the fast data rate measurement.

A partially successful attempt to address the slow thermal drift problem was made by manufacturing a second generation of Optrand transducers monolithically out of stainless steel. This monolithic construction did reduce slightly the contribution to thermal drift previously observed in a first generation of transducers. The slow thermal drift thus appears to have been caused in part by differential expansion of dissimilar materials used in the construction of the original transducer heads.

A more significant reduction in the downward drift was accomplished, however, by mounting the transducers at the end of 30-cm-long tubes that were introduced into the nozzle sites designed to accommodate the transducers. Such remotely positioned sensors were thermally isolated from the hot air and hence exhibited much reduced drift. This tactic proved to be a viable way of measuring the steady state nozzle pressure in the absence of e-beam heating. This type of mounting could not, however, be used during e-beam injection because of the large delay between the turn-on of the e-beam at the response of the transducer 30 cm away. See Fig 3-A5 below.

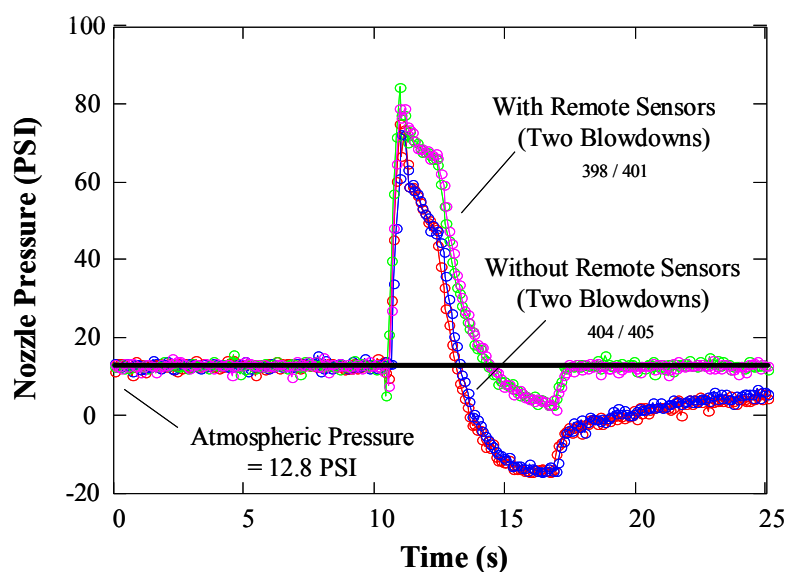


Figure 3-A5: Shown in this figure are four examples of nozzle pressure measurements taken during four identical blowdowns without e-beam heating. The measurements were taken with an Optrand transducer. In all cases, the same pressure tap (located near the center of the nozzle - channel 3, 31.5 cm from the throat) was employed. A severe downward drift due to the influx of hot air can be seen in the data taken with the transducers embedded in the nozzle. These cases are labeled “without remote sensors” above. A significant reduction in the downward drift can be seen in the cases labeled “with remote sensors”. These data were taken with the Optrand transducers mounted on 30 cm stalks.

Nozzle Temperature Measurements

Five J type thermocouples were embedded into the nozzle at locations diametrically opposite from the embedded Optrand transducers (see Fig 2-A1 and Table 1-A1). The temperature of the stainless nozzle was routinely recorded at a 10 Hz data rate during blowdowns. Typical data from these measurements is shown in Fig 4-A5. As expected the observed temperature excursion was clearly largest near the nozzle throat and smallest near the nozzle exit. The nozzle temperature measurements were generally used to characterize and compensate the thermal drift exhibited by the Optrand transducers.

Attempts were made to observe the temperature rise of the nozzle due to e-beam injection. No rise in nozzle temperature as a result of e-beam injection, however, was observed with either the slow or the fast sampling rate.

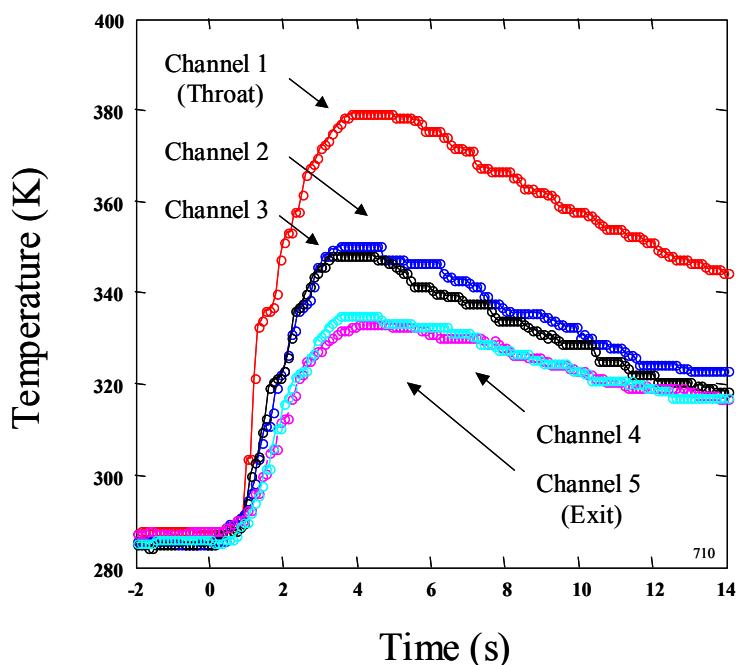


Figure 4-A5: Typical measured nozzle temperature increases measured at five locations due to a blowdown. The influx of hot air ended within 2.3 seconds after the opening at the high-pressure air valve.

PSI Fast Camera

A Princeton Scientific Instruments (PSI) Ultra Fast Framing Camera was used for several diagnostic measurements during the 1 MW experiments. The camera made use of a high-speed solid state imaging system. The PSI CCD image sensor for this camera consisted of two 80×160 pixel arrays fused together to form an active array of 160×161 pixels. Each pixel had an effective area of $115 \mu\text{m} \times 115 \mu\text{m}$. Hence the composite square array had dimensions of

18.5 mm \times 18.5 mm with a fill factor of 47 percent. This image sensor provided up to 28 images that could be exposed at user-selected burst rates of up to 1 million frames per second. Each pixel utilized a 14 bit A/D converter so that image data were mapped onto a 0 – 16,383 gray scale.

A thermo-electric cooler in the sealed enclosure of the camera head provided cooling of the image sensor. The CCD was operated at about -30 C to reduce dark current during the readout time. Both a mechanical and a Ferro-Electric liquid crystal shutter were opened prior to exposure, and closed during readout on command from the camera control chassis. The camera ran in a mode that captured images in an externally triggered fashion. Two TTL pulses from the Labmaster program were required to operate the camera: an arming pulse sent well before the camera was to be triggered and a trigger pulse. After receipt of the arming pulse but before receipt of the trigger from Labmaster, the camera ran with the shutter open in a continuous erase/expose mode. In this mode all frames in the storage area were continually over-written with new images while old images were dumped. When the trigger pulse was received, all overwriting was stopped. The result was that the most recent 28 frames were captured in the storage area. The shutters were then closed and readout took place as soon as the exposure was completed.

As explained in the section of this work describing the computer control of the experiments, adjusting the settings of a DD/PG controlled the delay between the firing of the HAWK and the start of the image-gathering process. The 28 images collected into the camera storage area were then read out in approximately 10 seconds and subsequently stored into tagged image format files (TIF files). The PSI camera and associated controller are shown in Fig 5-A5 below.



Figure 5-A5: The Princeton Scientific instruments camera and controller.

Shadowgraph: Mach Angle Measurements

Measurements of the flow Mach number with and without e-beam heating were accomplished using a standard shadowgraph system. A collimated beam of light was propagated across the region immediately in front of the nozzle exit. This beam was directed onto a reticle inscribed on diffuse reflectance glass. A sting was placed immediately in front of the nozzle at the bottom of the system field of view. Shadow images of the shock emanating from the string during the blowdown and projected onto the reticle were then recorded using the PSI camera.

The optical system employed a cw Verdi 5W (Coherent Inc.) laser operating at 532 nm. Passing the laser output through a spatial filter before it was directed toward the nozzle output ensured good mode quality. Using the PSI camera, the system required only a few hundred milliwatts, far less than the 5 W maximum output power of the laser. Examples of the resulting shadowgraphs are shown and discussed in Figs 7.1 and 7.2 of this report.

Spark Velocimetry Measurements

Two types of spark velocimetry measurements were undertaken—standard direct spark velocimetry and shadowgraph/spark velocimetry.

Direct Spark Velocimetry

Measurements of the flow velocity were made by using a high-power YAG laser (Spectra-Physics PIV 400, 350 mJ/p @ 532 nm) to cause air breakdown just in front of the nozzle during a blowdown. The translation of the resulting transient ball of plasma was followed downstream using the PSI camera. Hence a velocity could be measured both in the presence and in the absence of e-beam heating.

An optical barrier was erected immediately in front of the nozzle to prevent damage to the camera by the high intensity light generated during the initial breakdown. Images of the ball of plasma emerging from behind the barrier are shown in Fig 6-A5. The data were taken at a rate of 1 MHz, the maximum available framing rate of the PSI camera. Measurements of the change in position of the plasma ball are plotted against time for shots with and without e-beam heating in Fig 7.7 of this report. The slope of the resulting least squares fit to the data yields the flow velocity.

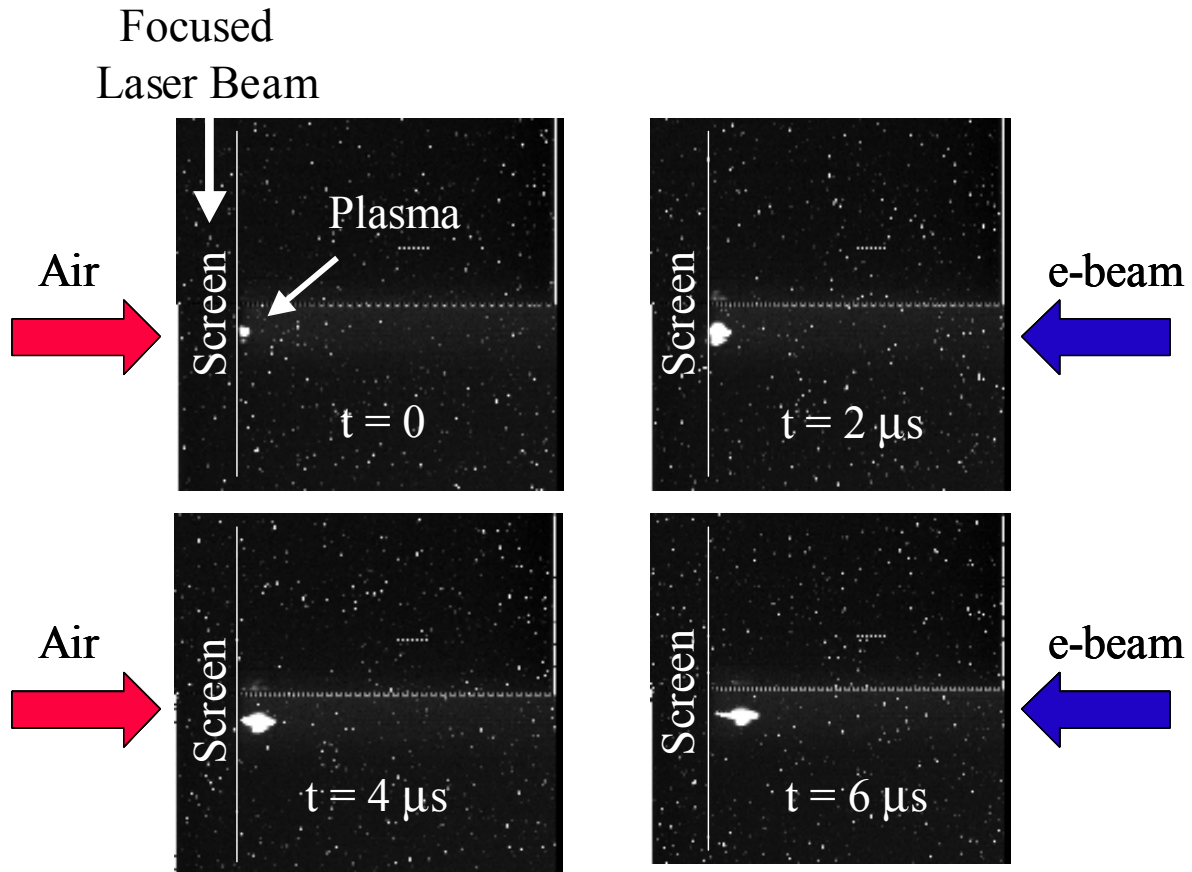


Figure 6-A5. Four frames from the direct spark velocimetry measurement for shot 746/4311 are shown in this figure. The first frame shows the location of the laser beam with respect to the screen that was erected to protect the PSI camera from the flash during air breakdown. A transient, laser-induced plasma can be seen to emerge from behind the screen and to translate downstream frame by frame.

Shadowgraph/Spark Velocimetry

A second type of spark velocimetry was employed. Instead of viewing the spark directly, the PSI camera was used to image the shadowgraph of the introduced spark. Because both the shadow of the spark and the shadow of the resulting sound wave were captured, this approach not only yielded the flow velocity, but also, the sound speed. This technique was successfully employed for unheated SMP blowdowns. During e-beam injection, however, no shadow of the inserted spark could be observed. This was likely due to the low central density brought about by e-beam heating. Examples of the shadowgraph / spark images are given in Fig 6.2 of this report.

Rayleigh Scattering

The Rayleigh scattering system employed a frequency doubled Q-switched YAG laser operating at 532 nm (again the Spectra-Physics PIV 400, 350 mJ/p @ 532 nm). The Rayleigh optical system produced a sheet probe beam approximately 1 cm wide x 1 mm thick that was directed across the flow path just in front of the nozzle exit. The probe laser produced four laser pulses and the associated Rayleigh images were typically separated by 100 μ s. The timing of the laser pulses with respect to the injection of the e-beam was controlled by the data acquisition system described previously. Typical Rayleigh scattering images are shown in Fig 7.12 of this report while reduced Rayleigh data may be seen in Fig 7.9.

All data was corrected for beam intensity variations along the flow path as well as any background scattering. The data were normalized to the pixels at the edges of the camera field of view adjusted to be +/- 19 mm from the center of the nozzle. It was thus assumed that the air +/- 19 mm from the center of the nozzle was undisturbed air at atmospheric pressure. This assumption was justified in cases of unheated blowdowns, but probably not justified in those cases with e-beam heating. Hence the air density measured by Rayleigh scattering was in fairly good agreement with the predicted value shown in Table 7.1 for the unheated case but in poor agreement with predicted value shown in Table 7.2 for the SMP shot. Similar trends can be seen in Fig 7.9. Future experiments will need to have a more reliable calibration of the Rayleigh scattering system in order to extract quantitative information about the density during e-beam heating.

Nozzle Current-to-Ground

In order to measure the total current returned to ground through the nozzle, it was necessary to “float” electrically the entire nozzle / magnets assembly. This was accomplished by inserting a high-pressure dielectric union in the airline leading to the nozzle. During the early part of the experiment, however, the dielectric union malfunctioned and “shorted” the nozzle assembly making current-to-ground measurements impossible. After the union was repaired, however, the current to ground was measured during every blowdown with e-beam heating. The current was measured by monitoring the voltage across a 5.5 Ω resistor used to connect the nozzle to ground. Approximately seventy-five measurements of the nozzle current were accomplished during this work. The results of those measurements caused a change in the direction of the research during the closing weeks of the experimental campaign.

It was surprising to learn that the observed nozzle current bore almost no relationship to the internally measured HAWK e-beam current. Large fluctuations in the nozzle current were routinely observed (See Fig 6.1 of this report). When this observation was made, it became imperative to understand the cause of these fluctuations. The course of the 1 MW experiments was then changed and a campaign to understand the origin of the current fluctuations began.

Accelerator Exit Return Current

In an effort to understand the return path of the accelerator current, a thin copper disk (3 mm \times 50 mm diameter) with a central hole (10 mm) large enough to allow the passage of the e-beam was centered over the HAWK exit window. The current collected by this disk was then recorded during blowdowns with e-beam injection. The intent of this measurement was to ascertain whether any beam current could be detected as following a return path to the accelerator. No significant return current was measured with this device. An example of this is shown in Fig 7-A5 below.

X-Ray Luminosity

An experimental effort was undertaken to determine whether the observed nozzle current fluctuations were being caused by some kind of air-beam instability or whether they were due to an unsteady current output from HAWK. To that end, after several inconclusive experiments using the available diagnostics, a makeshift x-ray camera was employed to study the beam-induced x-ray luminosity at the output of the HAWK.

A fast photomultiplier was first “blanked off” with masking tape to ensure that it would respond only to x-rays. The modified photomultiplier was placed inside an improvised x-ray “camera” constructed from three-inch-thick lead bricks. The camera was “pointed” at the HAWK exit window and away from the nozzle exit. The resulting signal seen during an e-beam shot was thus due only to the interaction of the high-energy electrons with the ambient air immediately outside of the HAWK exit window. Hence, the measured x-ray luminosity was supposed to be due to the current exiting HAWK before it had an opportunity to interact with the high-pressure air from a blowdown.

Comparisons of the x-ray data against the nozzle current data support the view that fluctuations in the nozzle current were due to the unsteady nature of the beam current delivered from HAWK. An example of this is seen in Fig 7-A5. It thus seems that these fluctuations did not arise from some unforeseen air-beam instability but rather were caused by the vignetting of the e-beam with structures internal to HAWK. A more thorough discussion of this is given in Appendix A4.

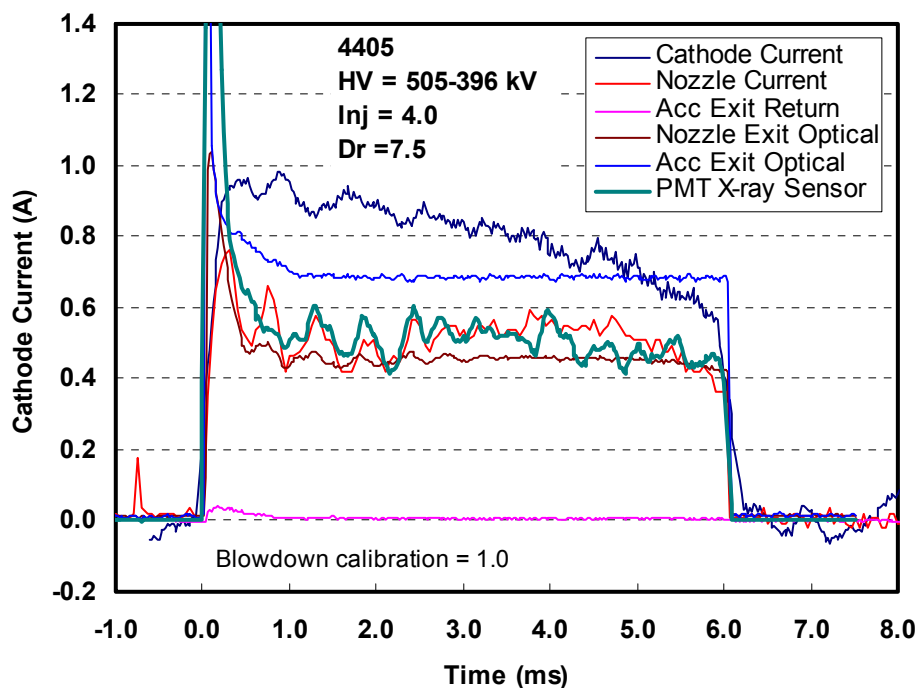


Figure 7-A5. In this figure are shown data taken during a 6 ms e-beam. The internal current as measured at the HAWK cathode appears to be fairly smooth while falling as a function of time. The nozzle current, however, is not only 40 to 50 percent smaller than the cathode current, but also fluctuates noticeably. The nozzle current fluctuations track fairly well with the fluctuations measured by the PMT x-ray sensor that was pointed at the HAWK output. This is interpreted to mean that the fluctuations seen on the nozzle current were introduced by HAWK and not by some beam-air instability. Also shown in the diagram are the e-beam visible luminosity signals taken at the HAWK output and the nozzle input. The lack of any discernible features in these signals demonstrates that x-ray luminosity is a better means of detecting current fluctuations. The current that returned from the nozzle area back to the HAWK exit is also shown and is clearly a small fraction of the total current.

NO Spectroscopy Measurements

Spectral UV-absorption measurements were performed to quantify line-of-sight NO concentrations just downstream of the nozzle exit plane. Xenon lamp radiation was passed three times through the flow field as illustrated in Fig. 8-A5 below and characterized spectrally using a grating spectrometer. The axial locations of the three passes were 0.5, 1.27, and 1.65 cm downstream of the nozzle exit plane. The beam diameter within the flow field was approximately 0.5 cm. During the experiments, the UV lamp was near the e-beam focusing magnets and had to be magnetically shielded with an improvised soft iron box. The magnetic field still interfered with the lamp discharge causing some loss of light to the detector during each shot. The spectrometer detector was set much farther from the magnets and partially shielded by a large laser power supply used for another diagnostic. There were no apparent affects to the detector

by the magnetic fields. Also, the detector was shielded from x-rays. X-ray events observed on ccd arrays during the 300 kW experiment were not observed on this detector during these tests.

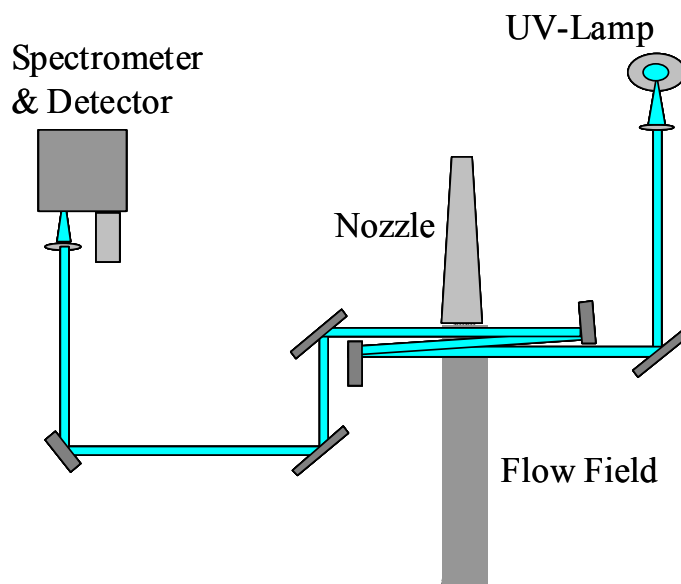


Figure 8-A5: The triple-pass optical configuration employed for the NO measurements.

The spectrometer was equipped with an intensified linear array detector and configured to measure from 210-250 nm with a 0.16 nm full-width-half-maximum spectral resolution. For this technique, absorption at the NO gamma (0,0) electro-vibrational band (226 nm) is used to quantify NO number density, given the flow-field static temperature and static pressure either deduced from other measurements or calculated using flow-field modeling codes.

Early NO-UV absorption measurements performed during e-beam injection exhibited radiation that interfered with the absorption measurement. Variations in facility operation conditions run-to-run prevented repeatable measurements with the lamp on and off that could have been used to correct for the interference radiation. To avoid interference from e-beam induced luminosity, it proved necessary to perform the NO-UV absorption measurements in the absence of the e-beam. In the experiment, measurements were typically taken during a 0.3 ms period beginning 0.1 ms after the e-beam was terminated. Because the transient time of the air from the throat to the nozzle exit was about 0.5 ms, the timing scheme employed would allow measurements to be taken on a column of air that had been heated in the nozzle by the e-beam just before it passed through the exit and into the spectrometer field of view. This assumed, of course, e-beam penetration to the nozzle throat. The timing of the NO measurements is illustrated in Figure 9-A5.

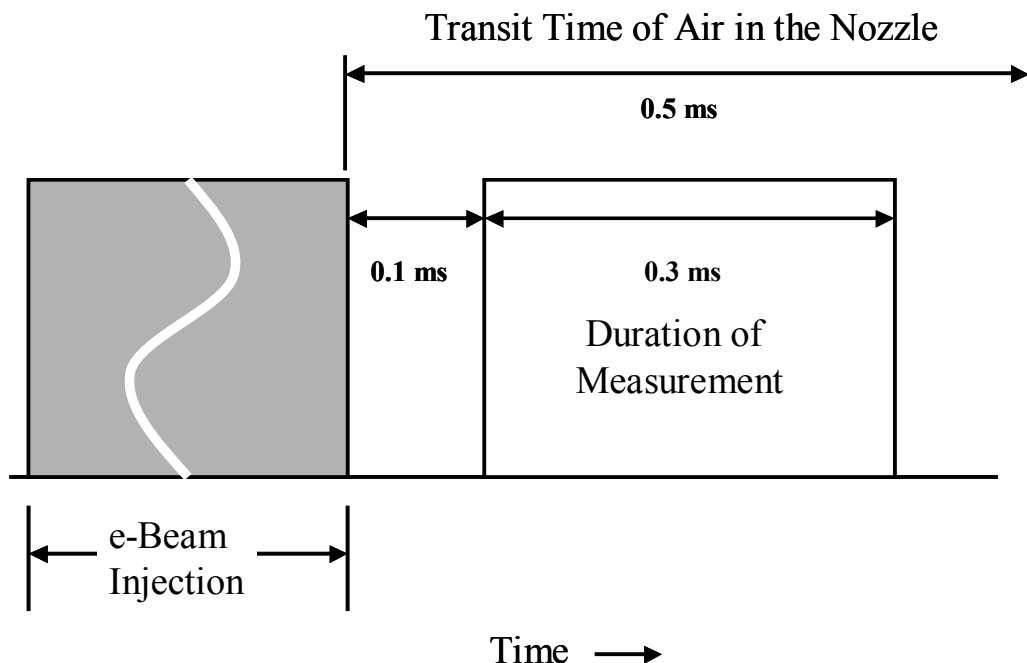


Figure 9-A5: The timing scheme employed for making NO measurements. The scheme allowed enough time (0.1 ms) for the X-rays and e-beam luminosity to subside after the termination of e-beam injection while still providing enough time (0.3 ms) to capture the NO created by the injection while it was escaping from the nozzle.

The initial power for each run of repeated conditions might be similar, but run-to-run variations in the temporal profile of the HAWK current and voltage often resulted in very different HAWK power outputs during the last 0.5 ms of each run. Since the NO-UV measurement was performed just after the e-beam was shutoff, this measurement was performed through gas heated by the last 0.5 ms of the e-beam.

One set of NO-UV absorption measurements were performed at lower HAWK power levels ranging from about 300 to 400 kW. No evidence of NO-UV absorption was observed during these experiments. Two factors could be contributing to no absorption. First, production of NO should be low at these conditions and could have been below detection limits. However, a primary factor was the shallow penetration depth of the e-beam at the lower power conditions coupled to the timing of the NO measurements described earlier. As stated earlier, e-beam heated air at the throat had a nozzle transient time of about 0.5 ms. But for the low power conditions, it was determined that due to shallow e-beam penetration the transient time of e-beam heated air was less than 0.2 ms after the e-beam was shut off. This being the case, the 0.3 ms NO absorption measurement was performed primarily through plenum air not heated by the e-beam. Therefore, the NO-UV measurements are not adequate for quantifying NO concentrations at the lower power conditions.

The second set of NO-UV absorption measurements were performed at higher HAWK power levels ranging from about 500 to 800 kW. NO gamma (0,0) band absorption was obvious as shown in the example spectrum in Fig. 10-A5 and the corresponding transmittance curve in

Fig. 7-14. The measured NO-UV transmittance ranged from 0.67 to 0.83 as shown in Table 1-A5 below. Other diagnostic measurements confirmed e-beam penetration to the nozzle throat area as desired.

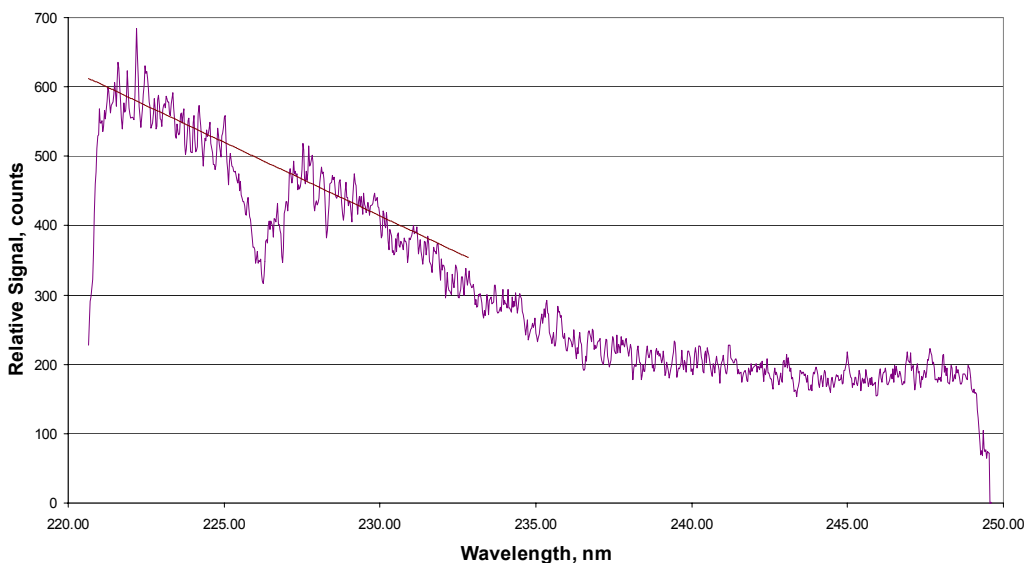


Figure 10-A5: A raw absorption spectrum taken during shot 728/4358. The NO absorption features can be clearly seen. The effective transmittance of this feature was calculated by compensating for the slope of the lamp emission spectrum approximated by the straight line. This shot received high-power e-beam injection for 1.2 ms, but the measurement was made during a 0.3 ms period beginning 0.1 ms after the e-beam was shutoff. The compensated transmittance is shown in Fig 7.14 of this report.

Table 1-A5: NO gamma (0,0) 2nd Bandhead Transmittance Values for High Power Run Conditions

Run #	Measured Transmittance	e-Beam Duration (sec)	Initial HAWK Voltage (kV)	Initial HAWK Current (Amps)
4353	0.81	0.5	564	1.5
4354	0.83	0.25	562	
4357	0.67	0.75	564	1.2
4358	0.70	1.2	561	1.53
4359	0.68	1.2	561	1.42
4360	0.73	2.0	561	1.20

Analysis of the NO-UV Absorption Measurements

The AEDC NO-UV line-by-line radiative transfer model was used to determine the number density of NO in the test medium from the measured transmission at the second bandhead of the NO-gamma (0,0) electro-vibrational band. The NO radiative transfer model is a line-by-line physics based model that spectrally calculates the absorption of each rotational transition including the effects of temperature and pressure line broadening. The NO model also simulates the spectrometer system instrument spectral response function and thus accounts for the measurement spectral resolution. The actual measured response for the instrument was used in the model since the “wings” varies greatly from a typical Gaussian shape. This model has been validated through extensive laboratory measurements at known NO concentration, pressure and temperature conditions.

The NO line-by-line radiative transfer modeling code requires an independent determination of radial and axial static temperature and static pressure profiles. Data from other diagnostic measurements were not adequate to provide the temperature and pressure profiles. Therefore, CFD flow-field models were required to calculate temperature and pressure. Time and resources prohibited extensive calculations for the proper flow-field conditions associated with the NO-UV measurements. However, the Princeton University CFD model was used to provide estimates of static pressure and static temperature at the nozzle exit ~ 0.25 ms after e-beam shut down using the simulated run (shot 699/4311) and the experimental pressure history for shot 728/4358. Princeton University estimates were $P_{\text{exit}} = 5.92 \pm 0.59$ atm and $T_{\text{exit}} = 1100 \pm 200$ K. Ideally, the radial profiles of static temperature and pressure for the three distinct axial locations of the 3-pass UV-beam would be used as inputs to the NO radiative transfer model used to deduce NO number density from the NO-UV measurement. But, other Princeton University calculations show very little fall-off of properties along the axis within the measurement volume. Thus, the flow-field in the region of the measurements was treated as a single homogeneous zone of constant temperature, pressure and NO number density.

Since the NO-UV measurement was implemented as a single (although multi-passed) line-of-sight measurement (no spatially resolved measurements), the NO density is assumed to be homogeneous in the analysis. The transmittance calculated using the NO radiative transfer modes is a function of the NO density-path length product. The path length of the UV lamp beam within the test medium (passed three times) was approximately 7.62 cm. The resulting NO concentration is an average NO density over the measurement volume. It should be noted that the e-beam was donut-shaped entering the nozzle and other diagnostic measurements indicate non-uniform total density (static pressure) and temperature profiles near the nozzle exit. This gives reason to believe that NO distributions are non-uniform as well.

The NO radiative transfer model was used to calculate a transmittance versus NO number density curve, Figure 12-A5, for the 7.62 cm path length, 1100 K static temperature, and 5.92 atm static pressure. The measured transmittance (0.70) for shot 728/4358 is labeled on the plot and corresponds to an NO number density of $3.70\text{E}+16 \text{ cm}^{-3}$. The error bar represents measurement uncertainty of ± 0.03 and corresponds to about $\pm 0.43\text{E}+16 \text{ cm}^{-3}$ ($\sim \pm 12\%$) uncertainty in NO number density.

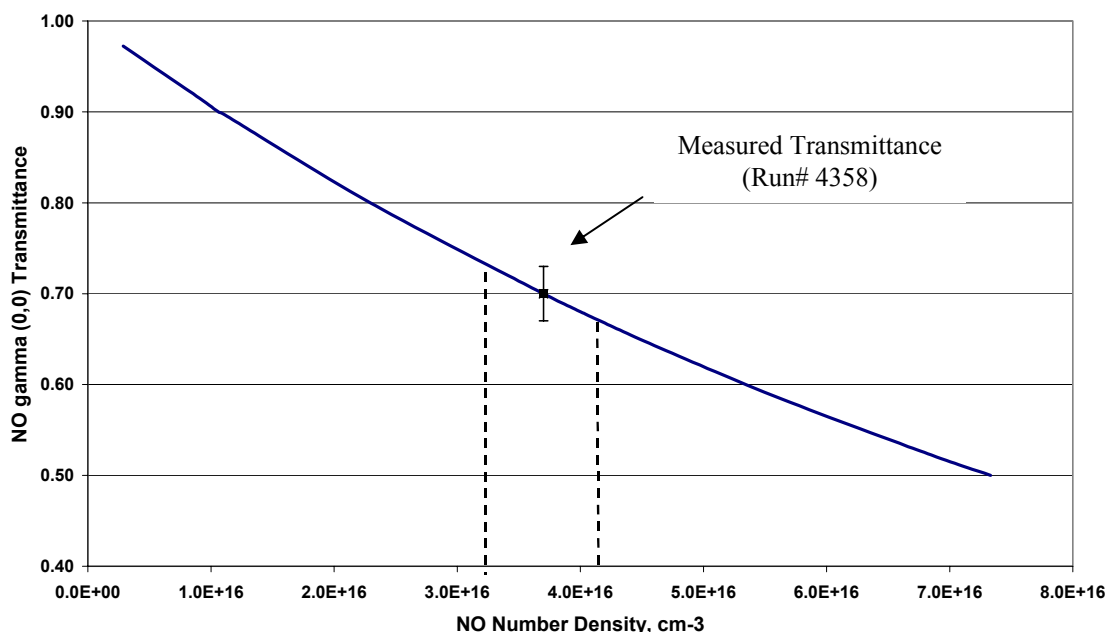


Figure 12-A5: Calculated Transmittance curve versus NO number density for a 5.92 atm static pressure, 1100 K static temperature, and 7.62 cm absorption path through a uniform homogeneous medium.

Calculations were performed to determine the sensitivity of NO number density to static temperature and static pressure. Static pressure affects the absorption line broadening. Calculations showed that pressure broadening had negligible effect on NO number density at these flow-field conditions for ± 10 percent changes in pressure. Static temperature affects both the absorption line broadening and the Boltzmann distribution among energy states. NO number density varied by less than 2 percent for ± 200 K changes in temperature. In both cases, much less than measurement uncertainty.

Accepting the spatial uniformity assumption of static temperature and pressure, the NO may have been preferentially generated in an annulus about the centerline. To illustrate the affect on the resulting NO density, assume the annulus is only 0.25 cm thick. The path length of the UV beam through the annulus for three passes would be only 1.50 cm (6×0.25 cm). Recall that the product of NO number density and path length is a constant in the radiative transfer model. Thus, the NO number density for the annulus region would be $1.88\text{E}+17 \text{ cm}^{-3}$ ($3.70\text{E}+16 \text{ cm}^{-3} \times 7.62 \text{ cm}/1.5 \text{ cm}$) or about 5 times greater for the annulus region. Notice that there are no experimental data to establish the spatial distribution. This discussion merely points out issues that should be considered in interpreting the NO number density presented here.

The NO-UV measurement gives the NO number density (for a fixed path length), not number fractional concentration of NO. To convert to concentration, the total number density is calculated using the ideal gas law and the estimated static temperature and pressure. The fraction of NO number density using the estimated 5.92 static pressure and 1100 K static temperature is 0.0010 ± 0.0003 . Treating the measurement volume as a homogeneous medium gives 0.1% NO.

APPENDIX A6: Time-Dependent Numerical Simulation

Time-Dependent Model Development

Because of some initial difficulties, the original CYLTRAN code was modified to allow for the handling of a larger number of electrons. The centerline power density (W/m^3) for the cases when power was deposited with 8,000, 16,000, 32,000, and 64,000 electrons were then compared against a 100,000-electron case. As expected, the increase in the number of electrons improved the statistics and the corresponding reduction in the percentage error for the power deposited per unit volume, as shown in Table 1-A6.

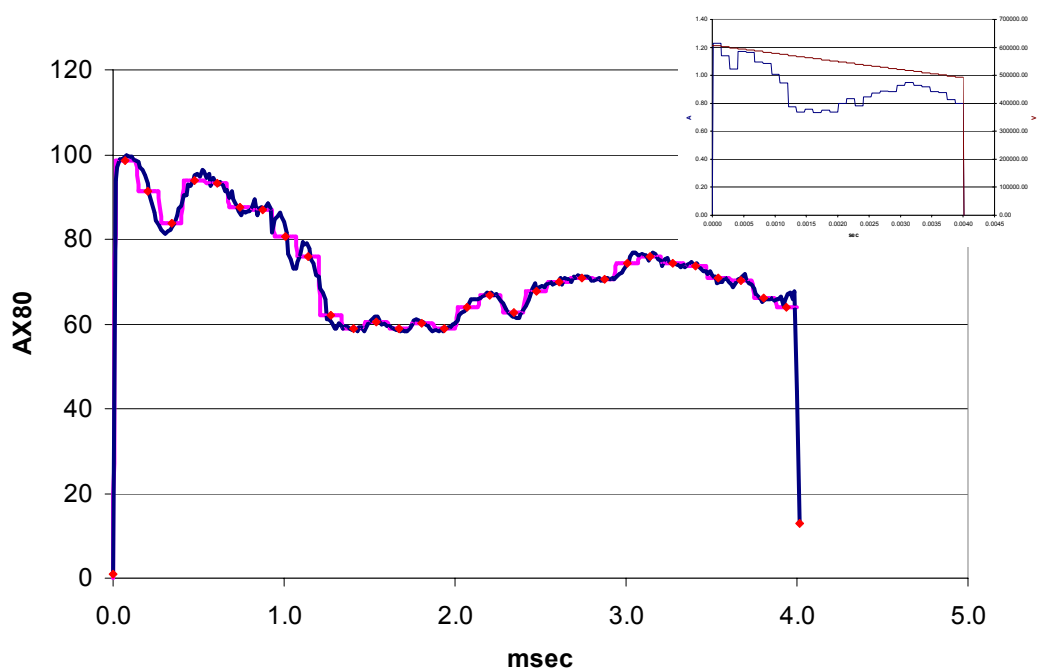
Table 1-A6: Error analysis using different number of electrons

# of Electrons	64,000	32,000	16,000	8,000
Mean % Error	3.997	4.554	6.270	7.482

Based on the above error analysis and the required code run time, the choice of 16,000 electrons was adopted for use in the time-dependent simulations. A further study of the effect of the heating error on the density profile compared with the 100,000-electron case showed that the mean error in the 8,000-electron case was 2 percent and in the 16,000-electron case was only 1 percent.

Current and Voltage Approximation

The time-dependent measurements of current and voltage were approximated by 30 step functions in which the current and the voltage were kept constant and equal to the local mean value over a time period of $\Delta t = 0.133$ ms, as shown in Fig 1-A6. The (ITS) code, for electron beam propagation, was called at the beginning of each step, with the local density given by the fluid mechanics code at the end of the last time step, to update the heating rate per unit volume for each cell for the next time step. With this heating rate the unsteady fluid mechanics code was next advanced with much smaller time steps ($\sim 2.5 \times 10^{-8}$ sec) to compute the unsteady flow physics for the next 0.133 ms when the heating was again updated. Thus it required approximately 200,000 iterations of the fluid mechanics code and 30 iterations of the CYLTRAN to calculate 5 ms of the flow. The calculations required approximately 25-30 hours on a 2.0 GHz Pentium IV processor. The procedure employed is outlined in Fig 2-A6.



maximum power ~ 750 kW

Figure 1-A6: The 30 step-function approximations to the variations in current. The approximated current and HAWK voltage are shown in the insert.

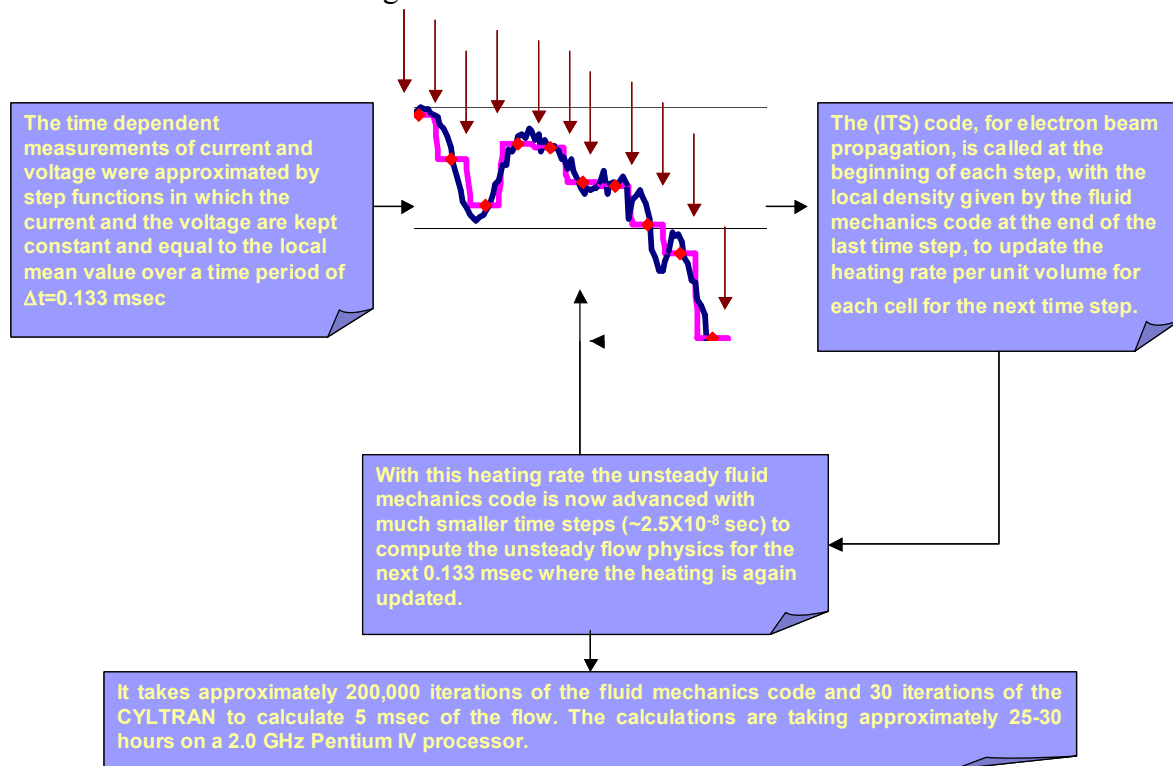


Figure 2-A6: An outline of the procedure employed in the calculations.

Results of Inviscid Modeling

Figures 7.6 and 7.10 of this report show the measured pressure at the five Optrand locations compared with the predicted pressure at these locations as a function of time. Figures 7.5 and 7.11 show the corresponding steady pressure distribution along the nozzle wall. Figure 5-A6 below shows the steady calculations for the Mach number distribution in the nozzle and in the downstream jet with and without the e-beam heating

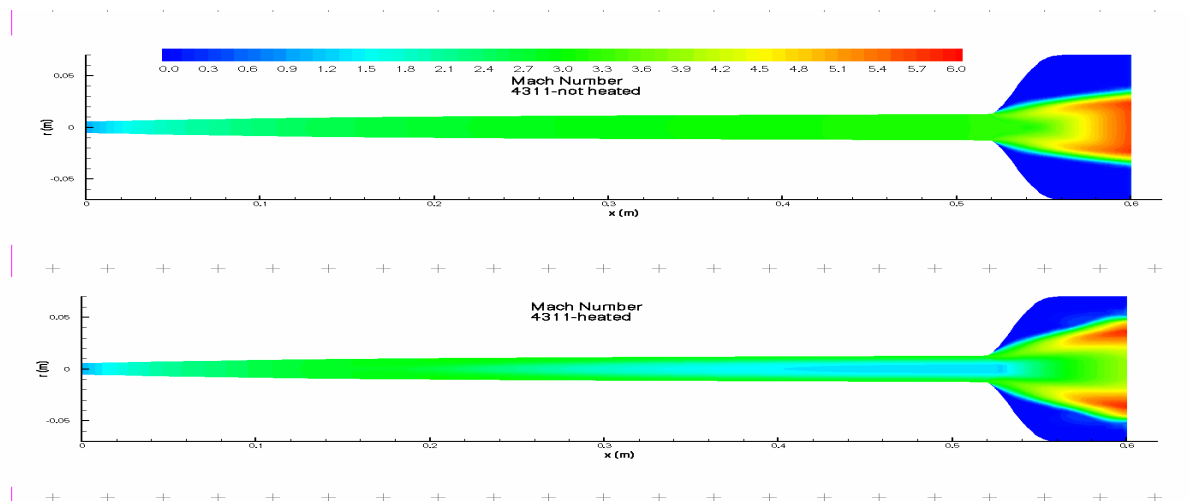


Figure 3-A6: Mach number distribution with and without heating.

e-beam Focusing

An effort was made to improve on the modeling results described above. In particular, to study the possible effect of aperture size on the predicted pressure time histories the cathode diameter was reduced to 90, 80 and 70 percent of its original size. This had the effect of increasing beam penetration. Figure 7.10 shows the predictions incorporating a 10-percent reduction in cathode diameter and the overall improvement in the comparison with the measurements.

Viscous Effects

In order to capture the effects of a turbulent boundary layer, a fully resolved viscous simulation is required. In order to carry out such a simulation, a very fine mesh near the wall is required so as to resolve the thin boundary layer; this is especially important at high Reynolds

numbers. To accomplish a steady-state viscous simulation, the required fine mesh would cause an increase of approximately a factor of three in the computational time. In the case of an unsteady viscous simulation, however, when an explicit time integration scheme is employed on such a fine mesh, the time step required for numerical stability becomes exceedingly small. Hence it is impractical, using the currently available hardware and codes, to perform unsteady viscous simulations.

In order to estimate the viscous effects on the pressure distribution, a viscous steady state simulation is performed for shot 699/4311. As shown in Fig. 1-A7, the viscous simulation gives lower pressure values compared with the Euler simulation. The maximum difference in values is approximately 8 percent for the heated case and 4 percent for the unheated case, at the nozzle exit

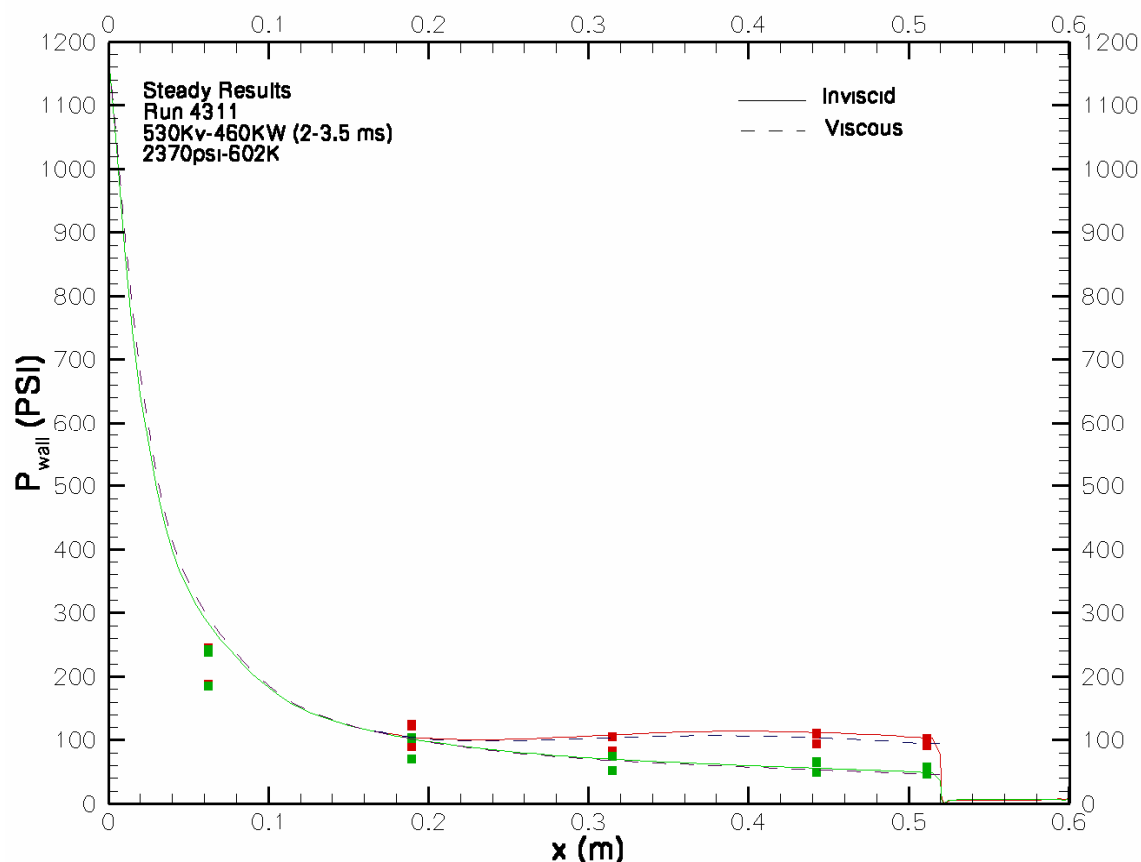


Figure 4-A6: comparison of the inviscid to the viscous calculations.